THESIS FOR THE DEGREE OF DOCTOR OF PHILOSOPHY

Comparison of incineration and pyrolysis of NMC-lithium-ion batteries – determination of the effects on the chemical composition, and potential formation of hazardous by-products.

GABRIELE LOMBARDO

Department of Chemistry and Chemical Engineering
CHALMERS UNIVERSITY OF TECHNOLOGY
Gothenburg, Sweden 2020

Comparison of incineration and pyrolysis of NMC-lithium-ion batteries – determination of the effects on the chemical composition, and potential formation of hazardous by-products.
GABRIELE LOMBARDO
ISBN: 978-91-7905-400-7

Doktorsavhandlingar vid Chalmers tekniska högskola
Ny Serie Nr. 4867
ISSN 0346-718X

Chalmers University of Technology
Nuclear Chemistry/Industrial Materials Recycling
Department of Chemistry and Chemical Engineering
Kemivägen 4
SE - 412 96 Göteborg
Sweden

Phone: +46 (0)31 772 2856 (work)
Cell: +46 (0)70 248 62 89
E-Mail: gablom@chalmers.se

Cover:
Apparatus used for incineration, dynamic pyrolysis and vacuum pyrolysis of lithium-ion battery anodes, cathodes, and separators.

Printed by:
Chalmers Reproservice
Göteborg, Sweden 2020.

Comparison of incineration and pyrolysis of NMC-lithium-ion batteries – determination of the effects on the chemical composition, and potential formation of hazardous by-products.

GABRIELE LOMBARDO
Department of Chemistry and Chemical Engineering
Chalmers University of Technology

Abstract

Several industrial lithium battery recycling processes use thermal pre-treatment in an oxidative or inert atmosphere, or in a vacuum, to separate the battery components and remove organic material. However, a comparison of these pre-treatments on the microstructure and composition of waste material and production scrap LiBs has not been explored as well as there is a scarcity of information about the character of by-products generated during the processing.

In this work the effects of incineration and dynamic pyrolysis on the composition of spent Li-ion batteries (LiBs) and the effects of incineration, dynamic pyrolysis, and pyrolysis under vacuum on the composition of production scrap Li-ion batteries (LiBs) were investigated. LiBs with cathode active material based on $Li(Ni_xMn_yCo_z)O_j$, i.e. NMC-LiBs, were treated from 15 to 180 minutes at a temperature between 400-700°C. During the pyrolysis, reactions with C and CO(g) led to a reduction of metal oxides, with Co, CoO, Ni, NiO, Mn, Mn_3O_4, Li_2O, and Li_2CO_3 as the main products. During the incineration, the organic material was removed more efficiently than in pyrolysis and the lithium metal oxides were subjected to both carbothermic reduction and oxidation. During pyrolysis at 700°C for 180 minutes, the carbon content decreased to 15w%, in comparison to the initial 41w%. The incineration performed under the same conditions resulted in almost complete removal of the graphite and organic species, ~0.6w%. Gas and organic oil by-products from the decomposition of the organic components were characterized. The presence of HF was detected and fluorine was identified also in the oil by-products. The decomposition of the binder facilitated the separation by mechanical treatment of the active material from the current collector. The best method to recover cathode material was shown to be incineration at a temperature range between 550˚ and 650˚ C for at least 90 minutes, followed by ball milling. The recovered fraction of active material was >95%. The formation of HF in the case of high temperature accident involving NMC-LiB was also determined. Four commercial refrigeration liquids containing halogens were investigated. The presence of these refrigeration liquids leads to an increase of the quantity of HF released during a simulated fire.

Keywords: Lithium-ion batteries; recycling; carbothermal; incineration; vacuum; pyrolysis.

LIST OF PUBLICATIONS

Thisthesis is based on the work contained in the following publications, referred to by Roman numerals in the text:

I. Lombardo, G.; Ebin, B.; St. J. Foreman, M. R.; Steenari, B.-M.; Petranikova, M. Chemical Transformations in Li-Ion Battery Electrode Materials by Carbothermic Reduction. *ACS Sustain. Chem. Eng.* **2019**, *7* (16), 1366813679. https://doi.org/10.1021/acssuschemeng.8b06540.

Contribution: *Main author, all experimental work, all data acquisition and interpretation.*

II. Lombardo, G.; Ebin, B.; Mark, M. R.; Steenari, B. M.; Petranikova, M. Incineration of EV Lithium-Ion Batteries as a Pretreatment for Recycling – Determination of the Potential Formation of Hazardous by-Products and Effects on Metal Compounds. *J. Hazard. Mater.* **2020**, *393* (November 2019), 122372. https://doi.org/10.1016/j.jhazmat.2020.122372.

Contribution: *Main author, all experimental work, all data acquisition and interpretation.*

III. Lombardo, G.; Ebin, B.; Steenari, B. M.; Alemrajabi, M.; Karlsson, I.; Petranikova, M. Comparison of the effects of incineration, vacuum pyrolysis and dynamic pyrolysis on the composition of NMC-lithium battery cathode-material production scraps and separation of the current collector. *Resources, Conservation & Recycling.* **2020**, *164* (January 2021), 105142. https://doi.org/10.1016/j.resconrec.2020.105142.

Contribution: *Main author, all experimental work, all data acquisition and interpretation.*

IV. Lombardo, G.; Ebin, B.; Foreman, R. StJ. M.; Yeung, L.W.Y.; Steenari, BM.; Petranikova, M. Formation of HF in the case of the high-temperature accident of the NMC-LiB using the cooling system based on the refrigeration liquids (RL) containing halogens – Manuscript.

Other publications that were not included in this thesis

Vieceli, N.; Lombardo, G.; Burçak, E; Petranikova, M. Recovery of metals from lithium-ion batteries by thermal pretreatment and organic acid leaching. Santiago, Chile; Hydroprocess 2020 Conference; **2020** October 26 – 30.

Contents

ABBREVIATIONS AND DEFINITIONS

The following abbreviations and definitions are used throughout this thesis:

°C	Degrees Celsius
>	More than
<	Less than
w %	Percentage weight total
ΔG^0_f	Standard Gibbs free energy of formation
ΔH^0_f	Standard Enthalpy of formation
ΔS^0_f	Standard Entropy of formation
EV	Electric vehicle
FTIR	Fourier Transform Infrared Spectroscopy
g	gram(s)
µg	microgram(s)
GC-MS	Gas Chromatography coupled with Mass Spectrometry
IC	Ion Chromatography
ICP-OES	Inductively Coupled Plasma-Optical Emission Spectroscopy
LiB	Lithium-ion battery(s)
M	Molar concentration (mol/L)
min	minute(s)
mL	millilitre(s)
PP	Polypropylene
PVDF	Polyvinylidene fluoride
RL	refrigeration liquid
SEI	Solid electrolyte interphase
SEM	Scanning Electron Microscopy
TCD	Thermal conductivity detector
XRD	X-Ray Diffraction

1. Introduction

Since the 1990s, Li-ion batteries (LiBs) have been widely used as the power source for portable electronic devices. This is because they can provide high energy and power per unit of battery weight, long storage life, low self-discharge, and a wide range of application temperatures [1,2,3]. The use of LIBs in portable electronic devices has doubled from 2014 to 2019 [4,5].
Due to its performance, the LiB is also widely used in the car industry for fully electric and hybrid engines[6,7]. Since LiBs have become a promising option for the reduction of CO_2 emissions, government and societal awareness of climate change are supporting the growth of the electrical vehicle (EV) industry[8,9].

The forecast indicates that there is a good chance that the global number of electric vehicles will be 50 million by 2025 and 140 million in 2030 [10,11]. This will lead to the increasing use of LiBs and, thus, of the raw materials necessary for their production [12,13].
Many of these raw materials are concentrated in the two electrodes that compose the LiB cells: an anode (negative pole), generally composed of a copper layer covered by graphite, and a cathode (positive pole), generally composed of an Al layer coated with an active material [14]. The performance of the battery cell is influenced by the chemistry of the cathode active material and the most used type in the automotive field is the NMC-LiB, i.e. a battery in which the cathode active material has the general composition $Li(Ni_xMn_yCo_z)O_j$.

Due to the forecast increasing demand for LiBs raw materials, the critical reserves of Co, and the instability in supply and price of Li, it is important to develop efficient and cost-effective recycling methods for LiB materials[16]. Furthermore, the lifetime of the LiBs used in EVs is around 10 years [20–22]. This means that the quick growth in EVs demand will soon cause an accumulation of the spent LiBs [18–20]. A system for collecting spent LiBs and effective processes for recycling the used materials in them is needed to ensure the raw material supply for the production of new LiBs [16,21].

The recycling processes used at present are mostly focused on the recovery of the metallic Al and Cu parts that compose the battery current collectors [22,23], and Co, Ni, Mn, and Li, from the cathode active material [14,24,25,26].

The industrial recycling processes generally use hydrometallurgical methods, pyrometallurgical methods, or a combination of both [21, 27–29,30].

In the pyrometallurgical processes, spent batteries often do not require discharging or mechanical pre-treatment, since smelting furnaces are designed for large volumes of raw materials [2,31–33]. Furthermore, no separation step is required if several types of batteries are processed, such as LiBs and Nickel–metal hydride batteries [34,35]. An alloy based on Ni, Co, Fe, and Cu is formed. Using the hydrometallurgical method, Ni, Co, and Cu are separated and recovered effectively from that alloy [51,58]. However, Mn, Li, and Al are lost in slag [32,38]. In some existing pyrometallurgical industrial processes (Nickelhütte–Germany [59], Sony/Sumitomo-Japan [39,40], Umicore-Belgium [41–44]) the organic components of the batteries are burnt off.

A major disadvantage of the pyrometallurgy method is the energy demand, as well as the necessity to treat the off-gases and loss of valuable components, such as graphite [45]. Despite the large demand for Li, Li recovery is generally not taken into consideration [46].

In comparison to the pyrometallurgy method, the hydrometallurgical method has many advantages, such as lower energy consumption, less hazardous gas emissions, higher total amount of material recovered, and the ability to recycle Li, Mn, and Al [47–50,51]. The recovery of metals from the black mass is carried out through leaching, solvent extraction, precipitation, and/or ion exchange methods [18,35,37,52,53]. In many cases a reducing agent is added to further increase the leaching efficiency. For example, hydrogen peroxide is added to reduce Co, Ni, and Mn compounds to species and increase the leachability of these metals [54]. Na_2SO_3, $NaHSO_3$, $(NH4)_2SO_3$ are also used as reductants in the leaching process [55,56]. In some existing industrial processes, such as the one used by Retriev Technologies-USA, Li is recovered by precipitation, for example as Li_2CO_3 or Li_3PO_4 [57,58]. The disadvantage is that the hydrometallurgical method is more complex than the pyrometallurgical one because it needs a series of additional pre-treatments. Indeed, a thermal pre-treatment (Accurec and Redux in Germany) or mechanical pre-treatment (Akkuser-Finland) is needed to separate the cathode's active material from the aluminum foil [59] and to remove the components that might inhibit or complicate leaching and solvent extraction (Recupyl-France) [2,17,20,65,82–84,87]. The thermal pre-treatment can be performed in three alternative ways: incineration, pyrolysis under inert gas, or vacuum pyrolysis. This is used as an effective tool for battery discharging, and electrolyte decomposition. Furthermore, the organic binder decomposes, allowing the separation of the active material from the current collector by mechanical treatment. In this way, Cu and Al layers can be recovered before the hydrometallurgical treatment [27,61]. Thermal treatments can also

trigger the carbothermic reduction reaction of the carbon present in the battery with the active material [5,46,113]. The metal ions in the active material are reduced to lower oxidation and/or more soluble states. In this way, the addition of a reducing agent during the leaching can be avoided [64].

Although pyrolysis and incineration as thermal pretreatment is already applied in the industrial recycling of LiBs, there is a lack of knowledge about the effects of the thermal treatment on the microstructure and composition of the battery material. Furthermore, most of the research is focused on $LiCoO_2$ as the active material, while the current trends are toward NMC and materials with higher Ni content. Moreover, only a limited number of studies have focused on thermal treatment of the other types of active materials, such as $LiNiO_2$ or $LiMn_2O_4$. There is also a marginal generation of by-products formed during the treatment. A thorough investigation of the formation of gas and organic residue is necessary, especially for industrial scale processes, as these substances can be toxic and can reduce the efficiency of the process and/or be corrosive, damaging the equipment used. One example is the harmful or corrosive gas containing HF that can be generated by the evaporation or decomposition of the electrolyte and binder during the thermal pretreatment. It is not known if the fluoride is completely removed from the battery cells in the form of gaseous HF or if it forms other compounds in liquid or solid by-products.

This work aimed to study and compare the effects of incineration with a constant flow of air, dynamic pyrolysis with a constant flow of inert gas, and pyrolysis under vacuum, as thermal pre-treatments, on the composition of the battery cell materials, as a function of treatment time and temperature.

Emphasis was placed on the characterization of the solid, gas, and liquid by-products generated during these treatments.

The formation of hydrofluoric acid in the case of high temperature accident involving LiBs using the cooling system based on the refrigeration liquids containing halogens was also studied. Such data are very limited in the literature, but they can contribute to a more sustainable design of the future batteries and knowledge about the risks associated with accidents with LiB thermal runaway.

2. Background and Theory

2.1 Li-ion battery components and composition

In the LiB, the charging and discharging events are determined by the movement of the Li cations from the cathode to the anode and vice versa. During charging, the Li ions move from the cathode material through the electrolyte to the separator and then again through the electrolyte to the anode. This event creates a flow of current up the negative current collector and to the positive current collector. During the charging/discharging cycles, Li ions have to intercalate and de-intercalate reversibly in the framework of the active material without introducing any significant structural changes [65–67].

A Li-ion battery (LiB) consists of a number of principal components, which are listed in Table 1. However, the composition varies according to the brand and application of the battery.

Table 1: Composition and function of the main LiB components

Component	Composition	Function
The negative electrode (anode)	Cu foil coated with graphite [60,68]	The anode receives lithium ions from the cathode during charging and emits lithium ions during discharging. Graphite is the most commonly used anode material in commercial LIBs due to its stable thermal and mechanical structure, electrical conductivity, non-toxicity, abundance [60,68] Li interacts weakly with graphite, so graphite can be used to intercalate and store Li, preventing formation of Li dendrites that could short circuit the electrodes and cause thermal instability [69].
The positive electrode (cathode)	Al foil covered with an electrochemically active material. In the automotive field, the active material is generally a Li-transition-metal-oxide ($LiMO_2$), where the metal M can be Co, Ni, Mn, Al, or one of their combinations. One of the most commercialized cathode materials has the general composition $Li(Ni_xMn_yCo_z)O_j$ [25,26]. Another common active material is $LiCoO_2$.	The cathode is commonly a lithium metal oxide material, which emits lithium ions to the anode during charging and receives lithium ions during discharging. The main benefit of NMC LiBs is their higher energy density compared with other chemistries [70].
Polymeric binder	Generally, it is in polyvinylidene fluoride (PVDF) [71].	The polymeric binder improves the adhesion between the Al foil and the active material [72].
Separator	Polypropylene (PP) [73].	The separator is permeable to Li cations but at the same time prevents contact between the electrodes and, thus, the internal short circuit and cell failure [74].
Electrolyte	Solvent: alkyl carbonates (ethylene carbonate, dimethyl, diethyl, and ethyl methyl carbonate) Salt: $LiPF_6$[1,75] or $LiClO_4$[76]	The electrolyte allows the movement of the Li cations between cathode and anode and facilitates the formation of the solid electrolyte interphase (SEI) layer, due to the decomposition of the electrolyte.
Thermal management system	A dielectric fluid in which the battery is immersed [77,78].	The thermal management system is necessary to maintain the proper temperature range [79,80].
Cover/shell	Steel or aluminium	All the other components are inserted into a container that can be a metal can, a plastic enclosure, or a metal foil-type pouch. The electrolyte liquid is injected, and the entire assembly is hermetically sealed [81].

Significant quantities of heat are created inside LiB cells during the charge and discharge cycles. This heat is generated by exothermic chemical reactions [82]. The performance, life, and safety of LiBs are very sensitive to temperature [83]. In the case of abuse of LIBs, such as overcharging or high temperature operation, exothermic reactions can be triggered. The heat released by these reactions causes a rise in the reaction rate, which can possibly result in an explosion. Such kinds of uncontrollable exothermic reactions are called thermal runaway. The thermal runaway starts with the decomposition of the SEI and involves the reaction of cathode, anode, and electrolyte. The exothermal reactions propagate to adjacent cells and set fire to the surrounding combustible materials. To avoid this, the LiBs are provided with a thermal management system that is required to maintain the proper temperature range [77,78]. Generally, LiBs are cooled with forced ambient or cooled air that is directed to flow across the surface of the battery cell. One alternative is the direct immersion cooling systems that use single-phase dielectric liquids. The battery cells are fully immersed in the dielectric fluid that is typically circulated with a pump to ensure a constant flow to make continuous contact with all the battery modules [79,80].

2.2 Thermodynamics of reactions involved in LiB cathode material high temperature treatment methods

2.2.1 Carbothermic reduction

Both incineration and pyrolysis have been described as valid methods to facilitate the recovery of Co, Mn, Ni, and Li triggering carbothermal reduction. Indeed, an improvement in the Co and Li recovery rate was achieved for $LiCoO_2$ cathode material subjected to incineration at 700°C, due to $LiCoO_2$ carbothermic reduction and carbon removal [45,84,85,86]. However, how the composition of active material changed during the thermal treatment has not been published.
Similarly, during pyrolysis at 650°C, NMC cathode material was reduced into Ni, Co, and MnO using lignite as a reducing agent[87, 88, 89]. This determined an increase in the leaching efficiency and the recovery of Ni, Co, and Mn. Instead of employing an external reductant agent, the use of the carbon already present in the cathode and anode materials as a reductant agent has not been explored.
The carbothermic reduction aims to reduce the metal oxides to metals in elemental form [90] and

produce also CO(g) and CO_2(g) [91] as by-products. The thermodynamic of these reactions can be predicted using the Ellingham diagram, Figure 1.

The Ellingham diagram is a plot of Gibbs free energy versus temperature, in which the reactions of formation of oxides are approximated to straight lines following equation (1) over the temperature ranges in which no phase transformations occur.

$$\Delta G^0_f = \Delta H^0_f - T\Delta S^0_f \quad (1)$$

in which ΔG^0_f is the change in the Gibbs free energy of formation, ΔH^0_f is the enthalpy of formation, T is the temperature, and ΔS^0_f is the entropy variation. So, ΔS is the slope and ΔH is the y-intercept of the straight lines in the diagram.

The carbothermic reduction can be described by the following reactions:

$$3MO(s) + 2C(s) \rightarrow 3M(s) + CO(g) + CO_2(g) \quad (2)$$
$$MO(s) + CO(g) \rightarrow M(s) + CO_2(g) \quad (3)$$

in which MO is a generic metal oxide. Reaction (2) is accompanied by a large increase in entropy because two solids (MO and C) are converted into one new solid (M) and two gas products (CO and CO_2). The reduction of metal oxides with C, which occurs when Gibbs free energy ΔG for the reduction reaction is negative, therefore becomes progressively more feasible at higher temperatures [92].

In contrast, in reaction (3), CO is a gaseous intermediate that is one of the products of the oxidation of C, as shown in reactions (4), (5), and (6).

$$C(s) + O_2(g) \rightarrow CO_2(g) \quad (4)$$
$$2C(s) + O_2(g) \rightarrow 2CO(g) \quad (5)$$
$$2CO(g) + O_2(g) \rightarrow 2CO_2(g) \quad (6)$$

CO_2 is the thermodynamically most favored product at temperatures below 700°C, as observed in the Ellingham diagram.

The position of the line of each element in the Ellingham diagram shows the stability of the oxide as a function of temperature. Lines closer to the top of the diagram describe the behavior of oxides that are unstable and easily reduced. In the lower part of the diagram, the metals become progressively more reactive and their oxides become harder to reduce. A set of considerations can be described:

- Li is extremely reactive, so the probability to find it in the elemental form will be very low. Li will keep its oxidation state +1 forming its most stable oxide, Li_2O.
- The Al of the cathode sheet forms another extremely stable oxide, Al_2O_3 (melting point 2072°C).
- Another element that could keep an oxidation state higher than 0 is the Mn, whereas Co, Ni, and Cu are significantly more easily reduced.

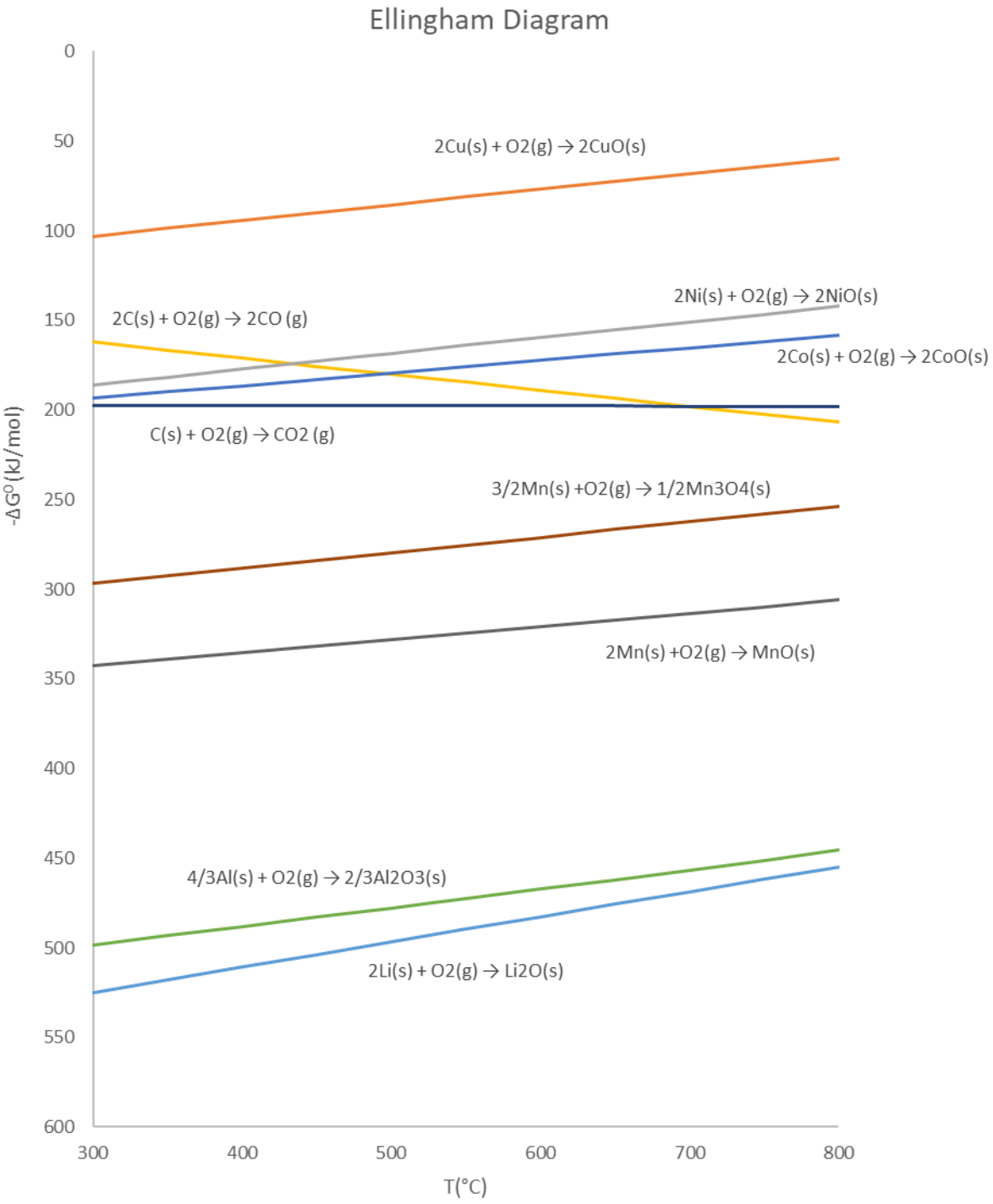

Figure 1: Ellingham diagram showing the standard Gibbs energies of formation of selected oxides as a function of temperature. All the reactions are normalized to consume one mole of O_2. The software HSC Chemistry 9, developed by Outotec, was used to build this diagram.

During the thermal treatment, it is expected that the lithium-metal-oxide compounds are subjected to a carbothermic reduction, triggered by the carbon present in the samples. Therefore the software HSC Chemistry 9, developed by Outotec, was used to carry out thermodynamic calculations to propose a hypothesis about which reaction mechanisms are involved during the thermal treatment. The oxides ($LiCoO_2$, $LiMn_2O_4$, and $LiNiO_2$) were considered individually and their possible interactions with O_2, C, and CO were studied. All the reactions described below are shown in Figures 2 and 3.

Incineration

$LiCoO_2$

At temperatures higher than 300˚C, C and CO can reduce this metal oxide. C and CO reduce some of the Co(III) present in the $LiCoO_2$ to Co(II) in the formation of $Co(II)(III)_3O_4$, in the presence of O_2, as described in reaction (7). Li_2CO_3 and CO_2 are the other products of these reactions. The $Co(II)(III)_3O_4$ is further reduced to Co(II)O and Co(0), according to the reactions (8) and (9). The trends for the ΔG^0 dependence on T for these reactions are shown in Figure 2. Li tends to maintain its oxidation state and form stable Li_2O. The possible reaction between CO_2 and Li_2O gives Li_2CO_3 as product, as described by equation (10).

$LiMn_2O_4$

Thermodynamic data regarding $LiMn_2O_4$ was not available in the HSC 9 database. Therefore, a separate database was created using the entropy and heat capacity data published by Knyazev [24] and enthalpy data published by Lai [93]. These extensions of the database permitted the extrapolation of ΔG^0 up to 126.85 °C. Above that temperature, the curve that describes the trend of ΔG^0 was approximated using the same software.

During the thermal treatment, the thermodynamic promotes the $Mn^{(+3)(+4)}$ reduction to $Mn(II)(III)_3O_4$ and Mn(II)O and decomposition to $Mn(IV)O_2$, as shown in reaction (11). It can be expected that $Mn(II)(III)_3O_4$ and $Mn(IV)O_2$ will react with C, CO, and O_2 forming Mn(II)O as described in reactions (12) and (13). These results are shown graphically in Figure 2.

$LiNiO_2$

There was insufficient data in the HSC Chemistry database available for $LiNiO_2$. Its behavior was therefore modeled as being similar to that of $LiCoO_2$ and was estimated using HSC Chemistry software.

The reaction of $LiNiO_2$ with C and CO in the presence of O_2 can give Ni(II) O and Li_2CO_3 as the main products, according to reaction (14). Ni(II)O can be further reduced by C and CO into Ni(0), as described by reaction (15). These results are shown graphically in Figure 2.

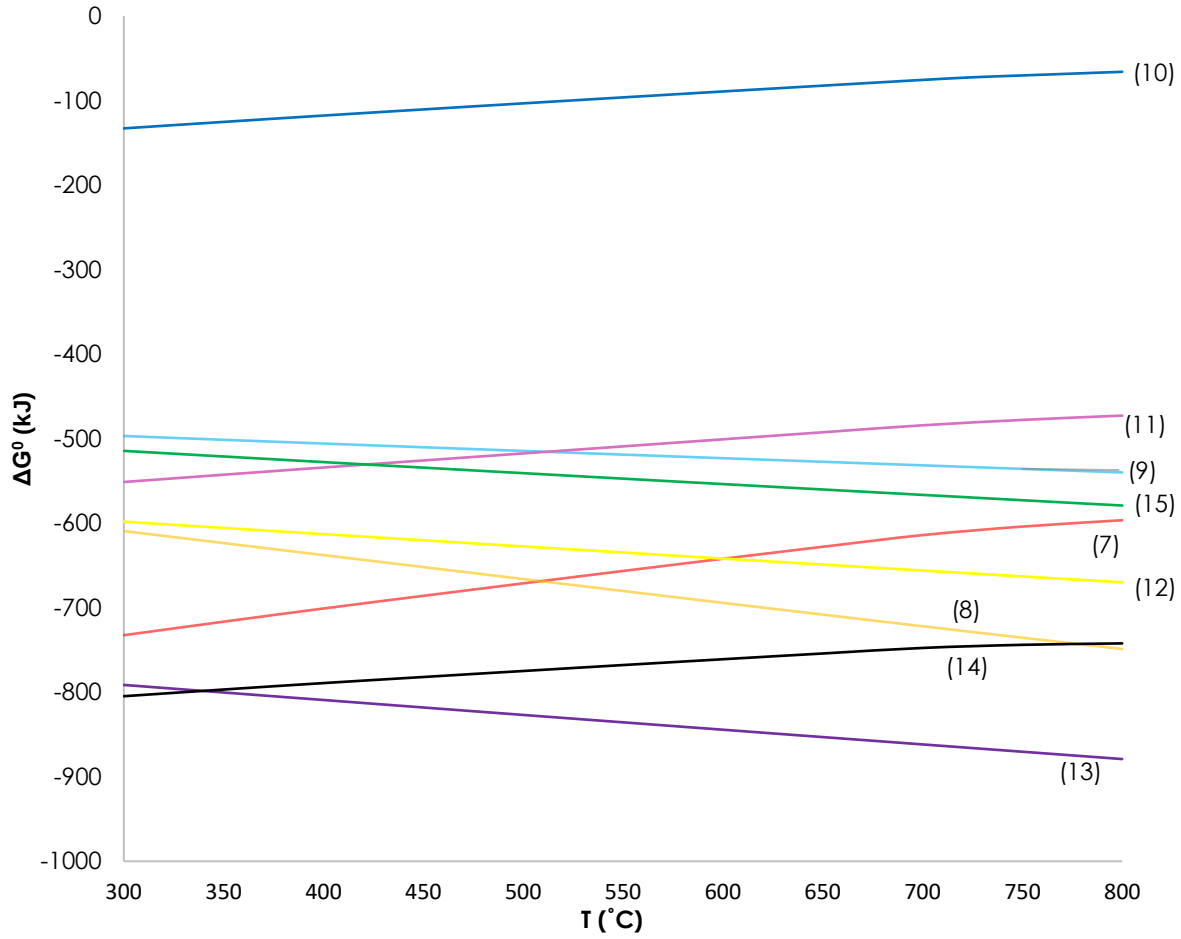

(7) 2LiCoO2(s) + 2/5C(s) + CO(g) + 2/5O2(g) → 2/5Co(s) + 2/5Co3O4(s) + 2/5CoO(s) + Li2CO3(s) + 2/5CO2(g)

(8) 4/5Co3O4 (s) + 2C (s) + CO(g) + O2(g) → 12/5Co (s) + 3CO2(g)

(9) 12/5CoO(s)+ 19/10C(s) + CO(g) + 23/20O2(g) → 19/10Co(s)+ 29/10CO2(g)

(10) Li2O(s) + CO2(g) → Li2CO3(s)

(11) 27/10LiMn2O4(s) + 13/10C(s) + CO(g) + O2(g) → MnO(s) + Mn3O4(s) + 13/10MnO2(s) + 13/10Li2CO3(s) + CO2(g)

(12) 2Mn3O4(s) + 7/4C(s) + CO(g) + 5/4O2(g) → 6MnO(s) + 11/4CO2(g)

(13) 12/5MnO2(s) + 19/10C(s) + CO(g) + 23/20O2(g) → 12/5MnO(s) + 29/10CO2(g)

(14) 4LiNiO2(s) + 2C(s) + CO(g) + O2(g) → Ni(s) + 3NiO(s) + 2Li2CO3(s) + CO2(g)

(15) 12/5NiO(s) + 19/10C(s) + CO(g) + 23/20O2(g) → 12/5Ni(s) + 29/10CO2(g)

Figure 2: Plots of ΔG^0 (kJ) vs T (°C) for the reduction of $LiMO_x$ with C or CO during incineration at different temperatures.

Pyrolysis

$LiCoO_2$

Co(III) is reduced to $Co(II)(III)_3O_4$ and Co(II)O by means of reactions (15) and (16). CO is a product of the reaction between the metal oxide and C. It can be expected that $Co(II)(III)_3O_4$ and Co(II)O will react with C and CO to form Co(0) as described in reactions (17) and (18). Li(I) can be present in the form of $Li(I)_2O$ and react with CO_2, forming $Li(I)_2CO_3$. The plot in Figure 3 shows how ΔG^0 varies with temperature for these reactions. Figure 4 shows the variation in the equilibrium amount versus temperature for each species involved in the carbothermic reaction of $LiCoO_2$ with C, resulting in Co, Li_2CO_3, and gases (CO and CO_2) as products. Above 600˚C, C forms both CO and CO_2. The amount of CO increases with increasing temperature. At 700˚C, the quantity of C reacting with oxygen to form CO and CO_2 is significantly higher than at lower temperatures.

$LiMn_2O_4$

The reactions of $LiMn_2O_4$ with C or CO give Mn_3O_4, and Li_2CO_3 as products, as described by reactions (19) and (20).

Mn with oxidation states III and IV in $LiMn_2O_4$ is reduced to Mn with oxidation states II and III in Mn_3O_4 and II in MnO. Another possible product is $Mn(IV)O_2$. The thermodynamic plots of ΔG^0 versus T for these reactions are shown in Figure 3. $Mn(II)(III)_3O_4$ and $Mn(IV)O_2$ can be further reduced by C to give Mn(II)O, as described by reactions (21), (22), and (23).

Instead, Mn(II)O can act as a reducing agent in the carbothermic reaction of $LiMn_2O_4$, as shown in (25) and (26), (Figure 3). The thermodynamic calculations show that the reaction (26) of $LiMn_2O_4$ with CO, in the presence of Mn(II)O, has a lower ΔG^0 over the entire temperature range compared to without Mn(II)O, as described by reaction (20).

This means that Mn(II)O can be involved in the reduction of the Mn(III)(IV), but C and CO would be the main reductant agents.

$LiNiO_2$

The carbothermic reduction of Ni(III) can give Ni(0) and Ni(II)O as the main products, as described by reactions (27) and (28). The Ni(II)O can in turn be reduced by C and CO into Ni(0) with the associated formation of CO_2, as described by reaction (29). The corresponding plot of ΔG^0 as a function of T is shown in Figure 3.

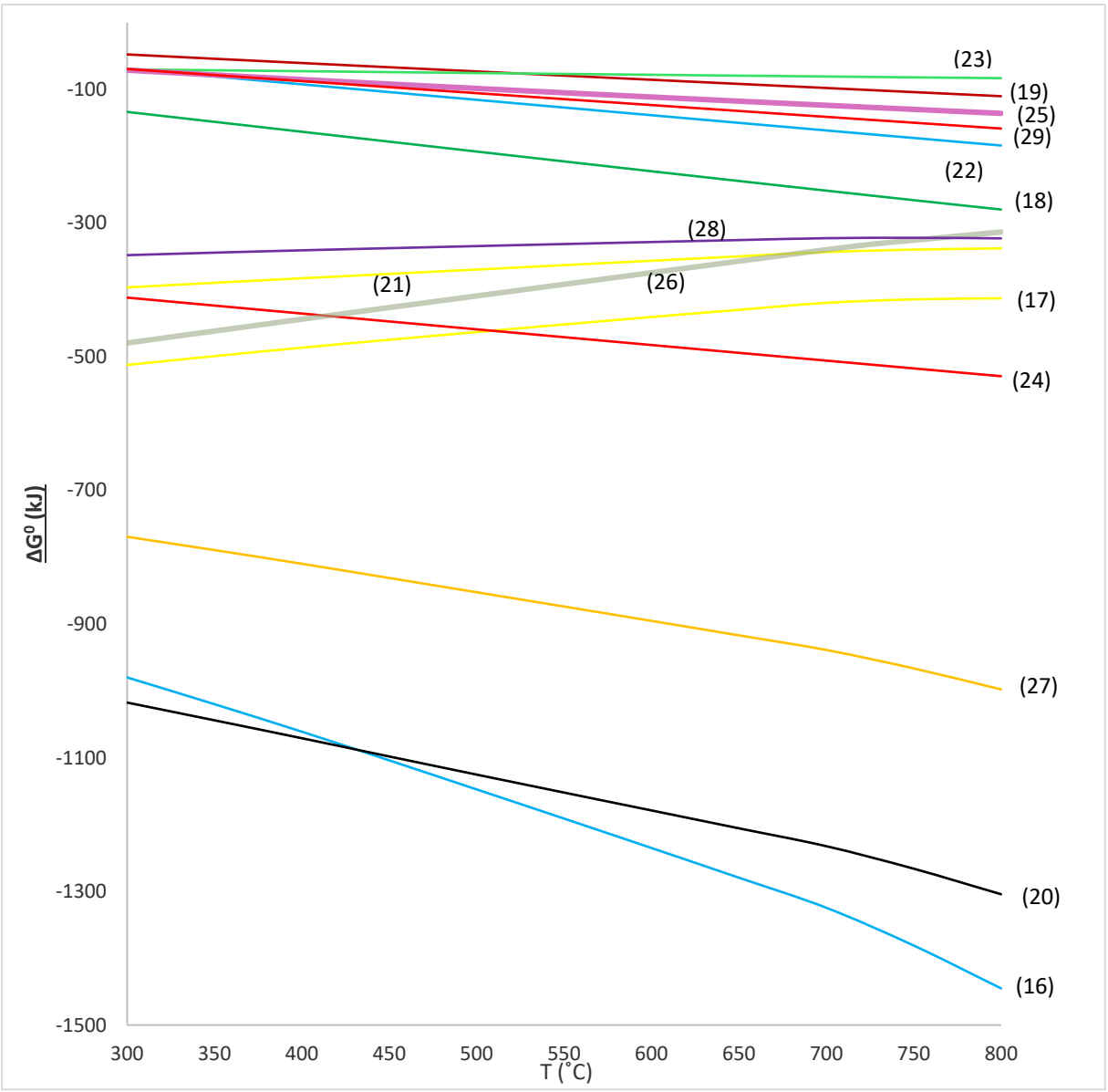

(16) 16LiCoO2(s) + 10C(s) → 12Co(s) + Co3O4(s) + CoO(s) + 8Li2CO3(s) + CO(g) + CO2(g)

(17) 2LiCoO2(s) + 3/10C(s) + CO(g) → 9/10Co(s) + 3/10Co3O4(s) + 3/10CoO(s) + Li2CO3 (s)+ 3/10CO2(g)

(18) 9/10Co3O4(s) + 34/25C(s) + CO(g) → 14/5Co(s) + 12/5CO2(g)

(19) 3CoO(s) + C(s) + CO(g) → 3Co(s) + 2CO2(g)

(20) 10LiMn2O4(s) + 7C(s) → 16MnO(s) + Mn3O4(s) + MnO2(s) + 5Li2CO3(s) + CO(g) + CO2(g)

(21) 2LiMn2O4(s) + 1/2C(s) + CO(g) → 2MnO(s) + 1/2Mn3O4(s) + 1/2MnO2(s) + Li2CO3(s) + 1/2CO2(g)

(22) 2Mn3O4(s) + C(s) → 6MnO(s) + CO2(g)

(23) Mn3O4(s) + CO(g) → 3MnO(s) + CO2(g)

(24) 3MnO2(s) + C(s) + CO(g) → 3MnO(s) + 2CO2(g)

(25) 2.8LiMn2O4(s) + MnO(s) + C(s) → 1.4Li2O(s) + 2.2Mn3O4(s) + CO2(g)

(26) 4LiMn2O4(s) + MnO(s) + 3CO(g) → 2Li2CO3(s) + 3Mn3O4(s) + CO2(g)

(27) 8LiNiO2(s) + 6C(s) → 7Ni(s) + NiO(s) + 4Li2CO3 (s) + CO2(g) + CO(g)

(28) 2LiNiO2(s) + 2/3C(s) + CO(g) → 4/3Ni(s) + 2/3NiO(s) + Li2CO3(s) + 2/3CO2(g)

(29) 3NiO(s) + C(s) + CO(g) → 3Ni(s) + 2CO2(g)

Figure 3: Plots of ΔG^0 (kJ) vs T (°C) for the reduction of $LiMO_x$ with C or CO during pyrolysis at different temperatures.

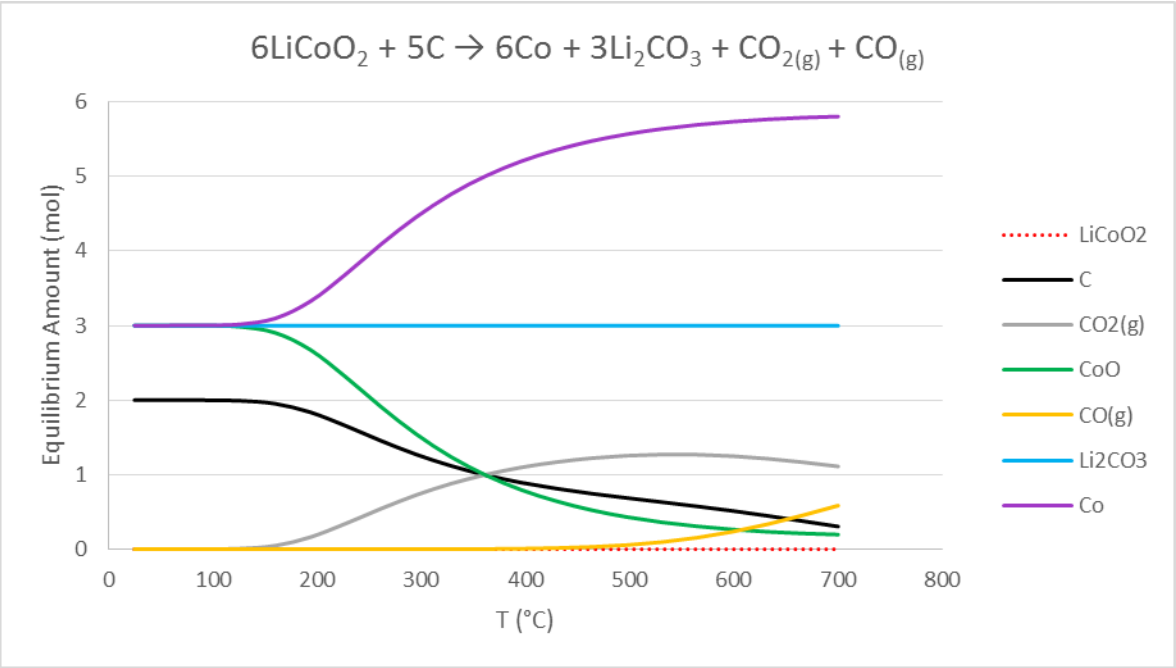

Figure 4: The variation of the equilibrium amount vs temperature for each species involved in the carbothermic reaction of $LiCoO_2$ with C, giving Co, Li_2CO_3, and gases (CO and CO_2) as products.

2.2.2 Decomposition of organic components and electrolyte during thermal treatment

Incineration has been shown to be highly efficient for the removal of the organic components, such as polypropylene separator, PVDF binder, and electrolyte, which facilitates the leaching process [84,85,86]. These components decompose releasing mainly CO_2(g), CO(g), and H_2O(g).

In contrast, the amount of CO and CO_2 produced per time unit during pyrolysis is lower than the amount of these gases produced by incineration, so it is generally considered a greener process. However, the decomposition mechanism of the battery organic components is more complex and can cause the formation of substances that are potentially corrosive and toxic. Pyrolyzing the polypropylene separator, the main products, in decreasing yields, are 2,4-dimethyl-l-heptene (boiling point 136°C)[94], 2-pentene (boiling point 38°C)[95], and the monomer propylene (boiling point -47°C)[96], all considered dangerous to health.

The pyrolysis or incineration of the PVDF binder and electrolyte generates considerable amounts of toxic gases, such as HF and fluorinated compounds. In the literature, quantitative measurements of HF in the gas emitted from Li-ion batteries are described only in the case of failure of the battery cells[97,98] and aging[99,100]. Thus, a qualitative and quantitative study to examine by-products generated through the thermal pretreatment of a recycling processes has not been carried out. Additionally, it is not known if the fluoride is completely removed from

the battery cells in the form of gaseous HF or if it forms other compounds in gas, liquid, or solid by-products.

PVDF is a crystalline polymer of quite high thermal stability and its thermal decomposition is heavily influenced by the presence of O_2[101]. Indeed, it has been observed through thermogravimetric analysis that the degradation of PVDF begins at around 320°C in O_2 and 450°C in N_2 [102]. It has been concluded that O_2 reduces the activation energy of the thermal degradation. This involves the release of gas containing HF(g) and the monomer vinylidene fluoride (VDF) (boiling point -85°C)[103] (g). In the case of pyrolysis, a small quantity of the dimer of VDF(g) and bigger aliphatic and cyclic molecules remain in the liquid fraction[104]. The major pyrolysis products are HF, VDF, 1,3,5-trifluorobenzene (1,3,5-TFB) (boiling point 76°C)[105], 1,2,4-trifluorobenzene (1,2,4-TFB) (boiling point 88°C)[106], and 1,4-difluorobenzene (DFB) (boiling point 88.5°C)[107,108]. The thermal treatment of fluorobenzene could also produce fluoro-dioxines[109], such as 2,3,7,8-TFDD[110], which are known for their serious environmental problems and significant negative effects on human health due to their toxicity[111].

$LiPF_6$ thermally decomposes into gaseous PF_5(g) and LiF(s) at around 200°C, when heated in a dry and inert environment. In the presence of electrolyte solvents, such as ethylene carbonate, dimethyl, diethyl, and ethyl methyl carbonate, the decomposing temperature of $LiPF_6$ can fall to as low as 85°C[112,113]

$$LiPF_6(\text{org. solution}) \rightarrow LiF(s) + PF_5(g) \quad (30)$$

In contact with moisture/water PF_5 reacts to form POF_3.

$$PF_5(g) + H_2O(g) \rightarrow POF_3\,(g) + 2HF(g) \quad (31)$$

POF_3 is a reactive intermediate that will react with other organic materials, or with water, generating HF [98].
PF5 also react with HF to form HPF6:

$$PF_5\,(g) + HF\,(g) \rightarrow HPF_6\,(g) \quad (32)$$

HPF_6 can further react with water to yield HF and form H_3PO_4 as a final product:

$$HPF_6(g) + 4H_2O(g) \rightleftharpoons H_3PO_4(g) + 6HF(g) \quad (33)$$

3. Materials and methods

3.1 Materials and thermal treatment

3.1.1 Spent NMC-LiBs cells (Papers I and II)

Figure 5: Untreated sample

A total of 6 spent NMC-LiBs cells, already discharged by the VOLVO CAR CORPORATION, were dismantled by removal of the plastic cover for the pyrolysis and incineration experiments. A manually crushed mixture of anodes and cathodes with separator was used. The electrodes were collected and representative samples of 0.5g were obtained by pressing using a puncher with a circular diameter of 2 mm, through an equal number of cathodes and anodes(Figure 5). These samples were subjected to incineration and dynamic pyrolysis at different temperatures (400ºC, 500ºC, 600ºC, and 700ºC) for different time periods (15, 30, 60, 90, and 180 minutes). Standard samples, consisting of a mixture of graphite and one of the pure metal oxides present in the black mass ($LiCoO_2$, $LiMn_2O_4$, and $LiNiO_2$), were subjected to the same thermal treatment. These standards were analyzed and compared to the NMC-LiB samples and the results from thermodynamic considerations in order to identify the mechanism of decomposition for each metal oxide.

3.1.2 Scrap NMC-LiBs cell cathodes (Paper III)

The starting material was composed of a LiB ribbon-shaped cathode consisting of an Al layer, 19.4 cm wide and 300 cm long (Figure 6). This was a scrap of a LiB cathode production chain. To prepare each sample, an area of 100 cm^2 covered by the active material was cut from the layer, weighed, and divided into pieces of approximately 5 cm^2. Samples of weight 1.95 ±0.3 g were prepared. These samples were subjected to incineration, dynamic pyrolysis, and pyrolysis under vacuum at different temperatures (450ºC, 550ºC, and 650ºC) for different time periods (30, 60, 90, and 150 minutes).

Figure 6: Cathode scrap material.

The choice of the treatment temperature for all the experiments was the result of a compromise: at a lower temperature, the efficiency of the PVDF removal, and thus the purity of the treated black mass, should be lower than it would be when treated at a higher temperature. On the other hand, higher temperatures can cause the Al to melt (melting point 660.3 °C), which in the liquid state could coat the samples and inhibit removal of the PVDF and the contact between the battery and the reducing atmosphere in the furnace. It was decided to perform the treatment at 700˚C to determine if there were any effects due to Al melting at this temperature. Experiments were carried out in triplicate.

3.1.3 Refrigeration liquids (Paper IV)

Tests were carried out to define how much HF could be generated in a fire caused by a car accident in a case when refrigeration liquid is used. LiB cells Samsung INR21700-50E with a weight of 69 g were cut in half to obtain representative samples with a weight of ~34.5 g. Each sample was partially immersed in 5 ml of refrigeration liquid (RL) to simulate a real ratio. Four commercial refrigeration liquids were tested. To determine how much HF can be generated by a refrigeration liquid in a high temperature event, thermal treatment at 700 ºC was performed, since 700 ºC is the average surface temperature of the battery cells during thermal runaway[98]. The aim was to trigger the decomposition of the organic material and refrigeration liquid.

3.1.4 Equipment for the thermal treatment

The thermal treatment was performed in a tubular furnace (Nabertherm GmbH Universal Tube Furnace RT 50-250/11). Each sample was placed in an alumina sample holder and inserted into a high-purity 65 cm alumina tube (Al_2O_3, 99.7%, Degussit AL23, Aliaxis). Custom-made stainless steel connectors were added to both ends of the tube. When the furnaced reached the

selected temperature, the alumina tube was then inserted in the tubular furnace. A constant flow of approximately 340 ml/min of 99.9% pure nitrogen (for the dynamic pyrolysis) or air (for the incineration) was pumped through the tube, with a flowmeter used to regulate the gas flow at the system inlet. For the vacuum pyrolysis, the samples were inserted into the part of the alumina tube located outside the furnace, as shown in Figure 7a. Using a thermocouple it could be measured that the samples in this part of the tube were subjected to a temperature no higher than 80ºC. A constant flow of N_2 was then injected in the furnace to remove the oxygen before the vacuum was formed. When the furnace was up to temperature, a vacuum of -0.75 bar was applied to the system with a Millipore vacuum pump. Then, each end of the alumina tube was closed with a valve, to keep the pressure in the tube constant. The vacuum pump was then turned off. The part of the alumina tube in which the samples were placed was moved into the furnace. The pressure inside the system was measured with a manometer (Figure 7b).

The exhaust gas was bubbled through three plastic cylinders filled with 150 ml of MilliQ water (ultrapure water with a resistivity of 18.2 MΩ.cm (at 25°C) and a TOC value below 5 ppb). The MilliQ water was then collected and analyzed. The MilliQ water from the gas-washing bottle directly connected with the alumina tube is referred to as B1. Consequently, the MilliQ water from the other gas-washing bottles is referred to as B2 and B3, respectively.

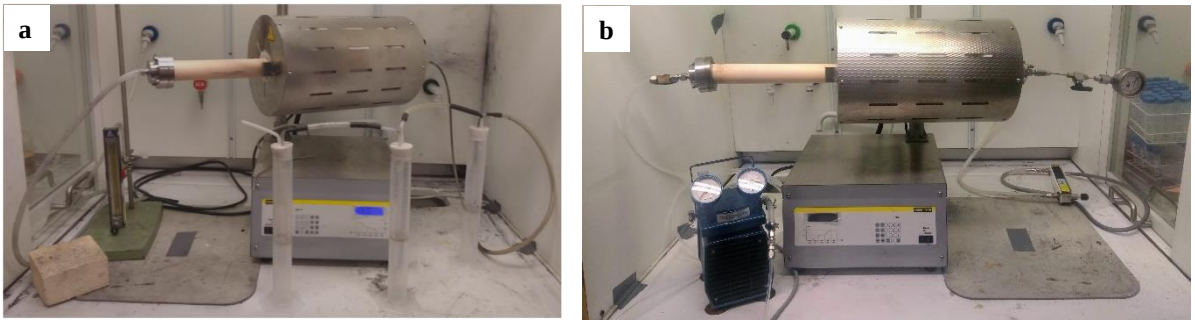

Figure 7: Apparatus used for a) incineration/ dynamic pyrolysis and b) vacuum pyrolysis

3.2 Determination of metal concentrations in solid samples by ICP analysis

The dissolution of the electrode materials was carried out using aqua regia (Merck Millipore Nitric acid 65% w/w - EMD Millipore Hydrochloric acid 37% w/w) at approximately 80ºC using magnetic stirring. The solutions obtained were filtered. The undissolved fractions were washed, dried, and weighed, and analyzed with X-ray diffraction (XRD). The liquid fraction was diluted 100 and 1000 times using 0.5M HNO_3, and an iCAP™ 6000 Series ICP-OES was

used to determine the metal concentrations in the solutions. To analyze the concentration of the metals in the organic by-products obtained through the thermal treatment, the organic by-products were dissolved in a solution 3:1 volume ratio concentrated sulfuric acid (H_2SO_4) (Merck Millipore 98.0% w/w)- hydrogen peroxide (H_2O_2) (Merck Millipore 30 % w/w in H_2O) and analyzed by ICP-OES. This acid mixture is a strong oxidizing agent and is thus highly efficient for wet combustion (removing most organic components). It will also hydroxylate most surfaces (add -OH groups), rendering them highly hydrophilic. Experiments were carried out in triplicate.

3.3 X-Ray powder diffraction qualitative analysis of crystalline compounds - XRD

The XRD analyses were carried out using a Siemens D5000 X-ray diffractometer, using an accelerator voltage of 40 kV and a current of 40 mA. The X-ray wavelength used corresponds to the characteristic Cu K-radiation, and a 2Θ range from 10° to 80° was included in the scans. Furthermore, sample rotation was applied with a rotation speed of 15 rpm. The obtained diffraction data was evaluated using EVA software by Bruker (USA) and the JCPDS database [114].

3.4 Fourier Transform Infrared Spectroscopy analysis of the gas produced during the thermal treatment - FTIR

The instrument used was a Perkin Elmer Spectrum Two FT-IR Spectrometer - Standard Detector, equipped with a $LiTaO_3$ detector, which has a range between 15700 – 370 cm-1. The sample holder was a cell equipped with gas-tight taps, the ends of which were closed with flat-glass KBr walls, transparent to IR. Since the gas density is low, the optical path was long, about 10 cm.

3.5 Analysis of carbon content in samples before and after thermal treatment in an oxidative atmosphere

A LECO CS744 instrument was used for the determination of the total carbon content in the samples before and after the thermal treatment. This instrument was equipped with a wide-range IR detector and an induction High-Frequency furnace in which an integrated oxygen lance floods the crucible holding the sample with high-purity oxygen to promote complete

combustion of the carbon present in the sample. To facilitate ignition, 0.1 g of each sample was mixed with 2 g of a tungsten/tin blend accelerator. Experiments were carried out in triplicate.

3.6 Ion chromatography

The MilliQ water used to wash the gas exiting from the furnace was analyzed using a Dionex DX100 Ion chromatograph to measure the concentration of fluorine. The column used was a Dionex IonPacTM AS4A-SC RFICTM 4x250 mm Analytical. The eluent was a solution of 1.7 mM $NaHCO_3$ and 1.8 mM Na_2CO_3. The pH of the washing water was also measured. The pH meter was calibrated to an accuracy of ±0,02 pH units at 25°C (Radiometer Analytical SAS) using three buffer solutions at pH 1, 4, and 7. Experiments were carried out in triplicate.

The concentration of F in the refrigeration liquids was determined by dissolving these liquids in an organic solvent (e.g., methyl tert butyl ether) and then diluting the samples using methanol. The samples were analyzed at Örebro University by professor Leo Yeung using combustion ion chromatography at 1050°C. The solvent used for dilution was also analyzed and a very low detectable level of F was found (16 ng F/mL). It was not possible to analyze the fluorine concentrations using classical ion chromatography since the refrigeration liquids are organic compounds. During the combustion ion chromatographic analysis, the organic F was converted into inorganic fluoride to be able to analyze it through a chromatographic column. Experiments were carried out in triplicate.

3.7 Scanning Electron Microscope (SEM)

The morphology of the samples was investigated using a FEI Quanta 200 environmental SEM equipped with an Oxford Inca energy dispersive X-ray detector (EDX). Imaging was done with an accelerating voltage at 20 kV.

3.8 Ball milling for the mechanical removal of black mass from the aluminum layer

A Fritsch Planetary Mill Pulverisette 7 was used. The machine consists of a rotation plate with two symmetrical holders. Each holder hosts a sample holder that contains quartz balls with a diameter of 1cm. After the thermal treatment, the cathode was milled in the ball mill for 15 mins at 1000 rpm. The same treatment was applied to untreated samples, to compare the efficiency of the black mass removal and the contribution of the thermal treatment. The samples, the internal surface of the sample holders, and the quartz balls were washed with

MilliQ water to recover all the cathode material detached from the Al foil. The removed cathode active material was then left in the air to dry and weighed. Experiments were carried out in triplicate.

3.9 Gas Chromatography coupled with Mass Spectrometry (GC-MS)

A Hewlett Packard HP 5890 Series II Gas Chromatograph and a Hewlett Packard HP 5972 Mass Spectrometer were used to analyze the composition of the oil by-product formed by the decomposition of the organic components of the LiBs. The GC was equipped with an Agilent Technologies column 112-5512, 15 m length, 0.25 mm inner diameter, 0.25 µm film thickness. The samples were diluted in Acetone 99.5 w% (Sigma-Aldrich) and 5µL were injected into the system The column had a temperature of 220ºC.

3.10 Analysis of the oil by-products

The oil by-products consisted of a less polar fraction, soluble in petroleum ether (Fraction 1), and a fraction with higher polarity (Fraction 2), soluble in acetone. To collect Fraction 1, petroleum ether was added to a part of the oil to dissolve the less polar fraction. This solution was then filtered to remove possible particles and the undissolved part. Filtration was done by leaving the solution to gravity-filter through a glass Pasteur pipette with an inner lining of cotton with an effective mesh size of approximately 10 µm as a filtering material. To collect Fraction 2 a similar procedure was used, treating a part of the oil with acetone and then filtering the acetone phase (Figure 8).

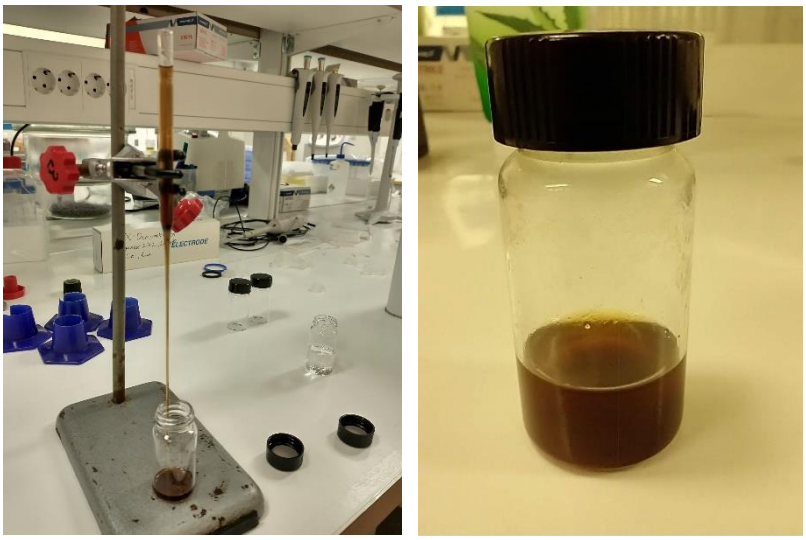

Figure 8: Organic by-products gravity-filtered through a glass Pasteur pipette with an inner lining of cotton as a filtering material.

3.11 C, H, and F analysis carried out by MedAc laboratories (UK)

The oil by-product and the MilliQ water used to wash the gas exiting from the furnace were sent to MEDAC laboratories (UK) for elemental microanalysis. C and H analysis was carried out by combustion analysis. The sample was completely and instantaneous oxidized by combustion, which converts all organic and inorganic substances into combustion products. The resulting combustion gases passed through a reduction furnace and were swept into the chromatographic column by the He carrier gas. Here they were separated and eluted as carbon dioxide and water and detected by a thermal conductivity detector (TCD), which gives an output signal proportional to the concentration of the individual components of the mixture. The instrument was calibrated with the analysis of known standard compounds. The F was analyzed by means of combustion, followed by titration or ion chromatography.

4. Results and discussion

4.1 Characterization of the battery material

A total of 6 cells were dismantled by removing the plastic cover. The cathodes and anodes were separated from the separators manually and the black mass was scraped from the anode copper foils and cathode aluminum foils. Each component was weighed. The average weight of each cell was 553.1±0.2 g, including an external plastic cover of 23.0 g. Internally, each battery cell consisted of 19 anodes interleaved with 18 cathodes. The weight of the black mass recovered from the cathode aluminum layers was 218.2±0.8 g and represented the main component of each cell, followed by graphite (115.9±0.3 g), the copper foils (57.0±0.1 g), aluminum foils (36.0±0.1 g), and separators (42.2±0.5 g). A summary of this data can be seen in Figures 9 and 10. The percentage of electrolytes in Fig 10 is a calculated value.

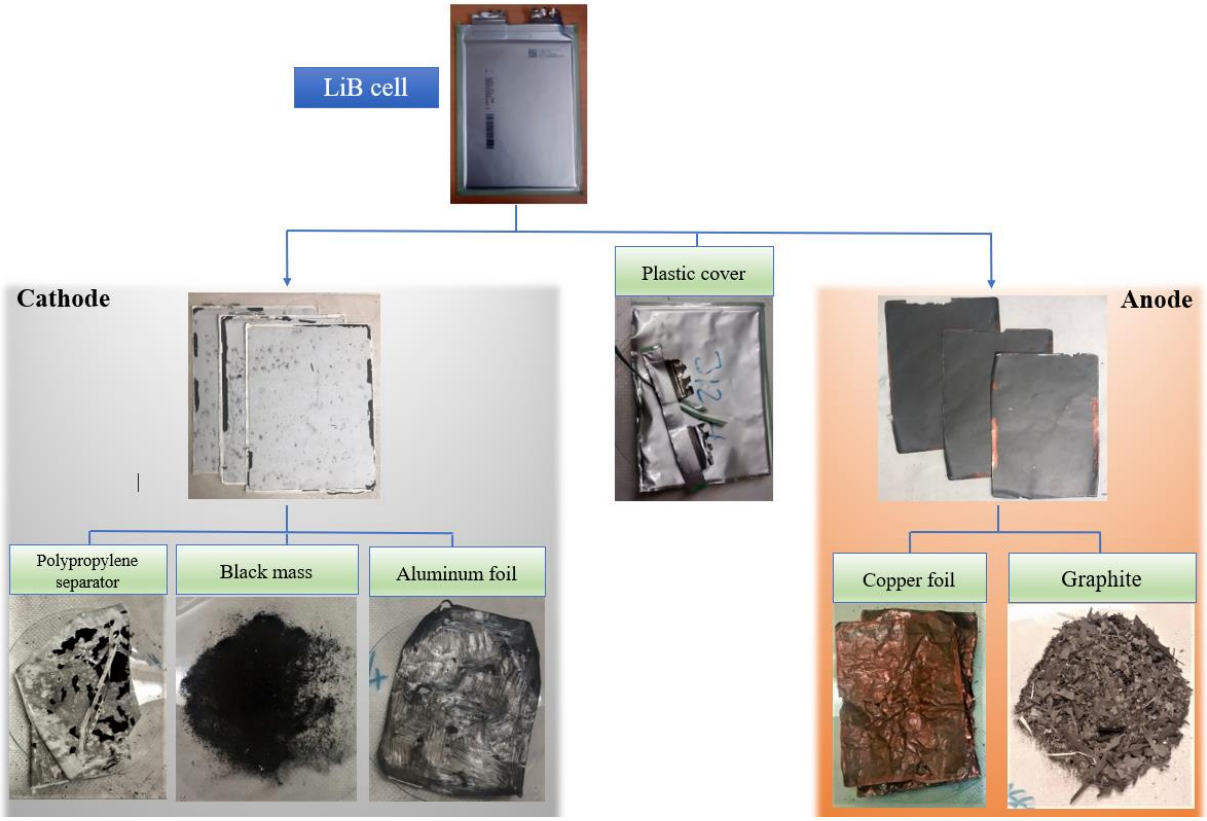

Figure 9: Components of the LiB cell.

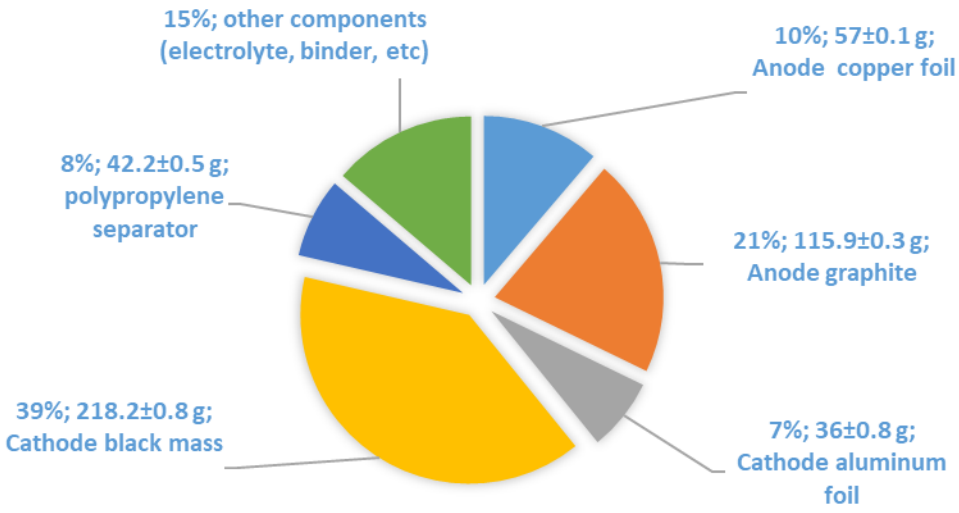

Figure 10: Mass balance of used material.

To investigate the composition and microstructure of the batteries, samples consisting of a mixture of both cathodes and anodes were prepared. Through the ICP-OES analysis, the weight % of the metals in a battery cell was calculated (Table 2). The calculated limits of detection (LODs) for the analyzed elements are also shown.

Table 2: The weight percentage of some elements in the battery cell. (the Metal composition of the battery cell).

Element	Mn	Ni	Co	Cu	Li	Al	P
w%	11.0±0.7	5.6±0.3	5.5±0.3	12.3±0.8	2.4±0.2	6.8±0.5	0.3±0.1
LODs	0.1	0.2	0.2	0.1	0.2	0.1	0.1

By analyzing the cathode and anode separately, it was observed, as expected, that the composition of the two types of electrodes was considerably different (Table 3): Cu was only detected in the anode; Al, Co, Mn, and Ni in the cathode, whereas Li was present in both electrodes.

Table 3: Metal composition of the electrode material [w%].

Element	Mn	Ni	Co	Cu	Li	Al
Anode	nd	nd	nd	27.2±0.8	0.1±0.2	nd
Cathode	19.0±0.7	9.0±0.3	9.1±0.3	nd	3.7±0.2	10.3±1.2

nd = not detected

The identification of crystalline compounds performed by XRD of these samples identified the presence of Cu and Al, both in elemental form and oxide form, as shown in Figure 11. The most intense peak at 27˚ is generated by the graphitic carbon.

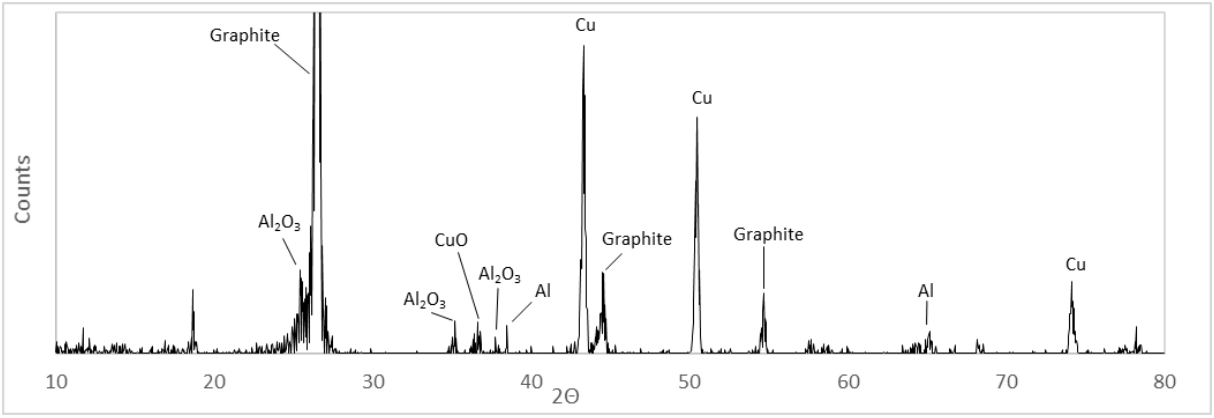

Figure 11: The XRD diffractogram of mixed electrode materials (anode and cathode).

The complexity, and in some cases similarity, of the X-ray diffraction spectra for transition metal oxides makes it difficult to identify the specific Co, Ni, and Mn oxides present. Therefore, further XRD analysis was performed only on the active cathode material, which was mechanically separated from the aluminum layer. The result is shown in Figure 12. It was possible to identify the presence of $LiMn_2O_4$, $LiNiO_2$, and $LiCoO_2$. The peak at 18.7˚ is common for all three metal oxides, therefore, its absence in the spectra of the treated samples could be considered as evidence of the almost complete decomposition of the lithium metal oxides.

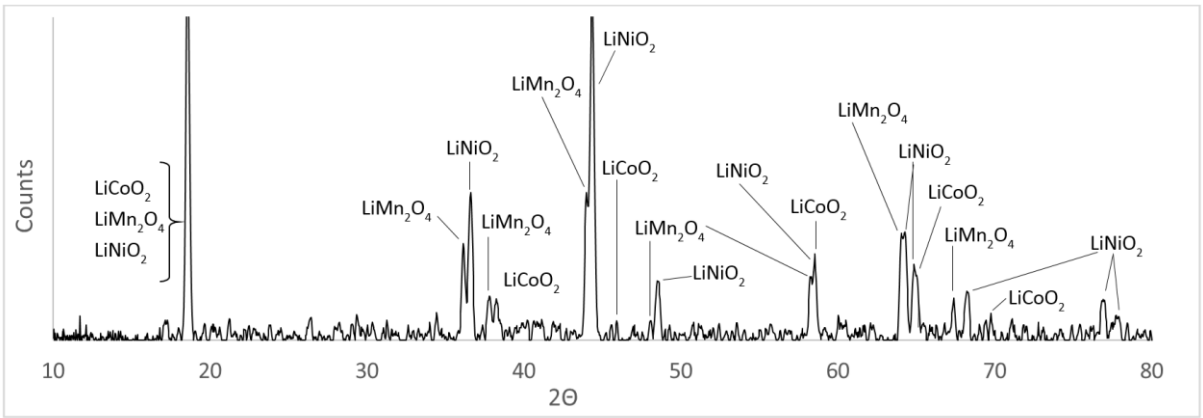

Figure 12: The XRD diffractogram of cathode material.

The XRD diffractogram of the solid fractions remaining after the attempted total dissolution of the samples shows a hump at low angles. This is due to the amorphous nature of the polymers, i.e. the separator material and binder, in PP and PVDF. Diffractions originating from Al_2O_3 were also detected. The undissolved fraction obtained from the negative electrodes was essentially graphite.

4.2 Pyrolysis

4.2.1 Spent NMC-LiBs cells (Paper I)

Change in sample weight during dynamic pyrolysis

By measuring the weight of the samples before and after the dynamic pyrolysis, a general loss of mass was detected, which increased with the rise in temperature and the duration of the dynamic pyrolysis (see Figure 13). After treatment at 700ºC for 90 minutes, a loss of ~22 w% was measured, doubling the weight loss obtained at 400 ºC for 90 minutes. Increasing the temperature from 500 to 600ºC did not have a notable effect on the sample weight. Furthermore, the treatment time heavily influenced the change in the weight of the samples (Δw%), especially at high temperatures. All samples lost a significant part of their weight in the first 15 minutes of the treatment. The reason is the evaporation of the organic solvents present in the battery, which happens at a temperature higher than 150ºC. The effect determined by the variation of the treatment time is more evident at 700ºC than at a lower temperature. Indeed Δw% passed from ~9% at 15 minutes to ~22% after 180 minutes. Furthermore, Δw% reached a maximum after 90 minutes, followed by a plateau.

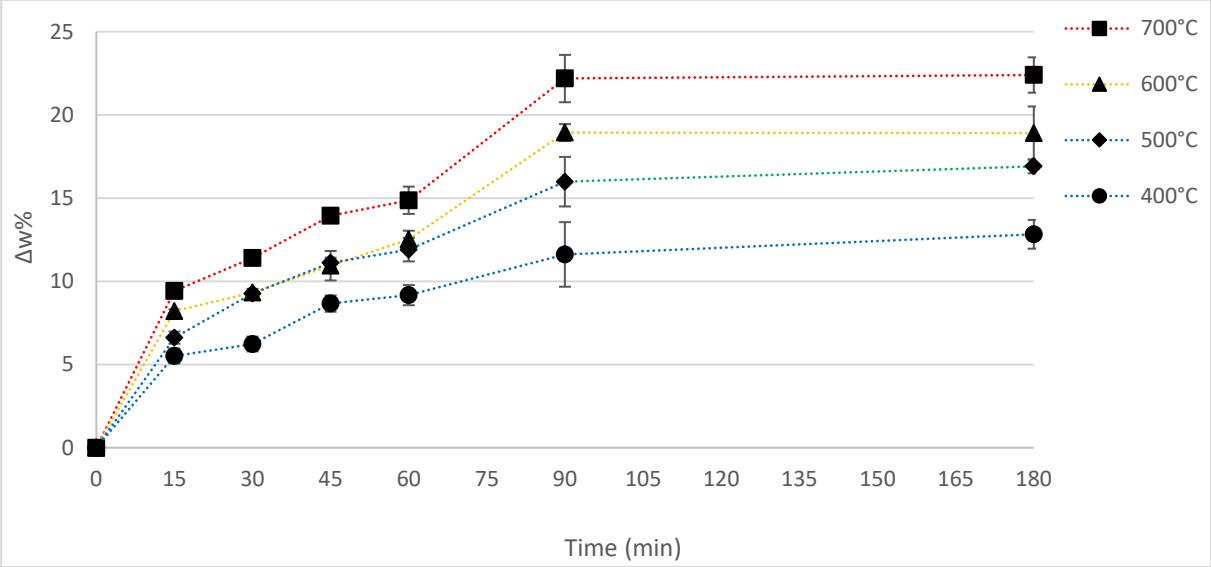

Figure 13: Weight loss in dynamic pyrolysis at different temperatures and times. The (0;0) point corresponds to the untreated material. The lines are only provided to guide the eye.

To confirm the hypothesis that the Δw% was mainly caused by the decomposition of the organic components and oxidation of the graphite, the residual carbon contents in the samples were measured. The percentage weight of carbon decreases with the rise in time and temperature of

treatment (Table 4). The concentration of carbon in the samples pyrolyzed at 700°C for 180 minutes is the lowest (15 w%) from an initial 41% in the untreated battery.

Table 4: Change of the carbon content in the sample in the dependence on the time and temperature of dynamic pyrolysis.

T (°C)	Time (min)	Carbon content (w%)
Untreated	0	40.8±2.8
400	30	35.5± 2.4
	60	32.8±2.0
	90	21.2±1.6
	180	19.0±0.9
500	30	32.0±2.5
	60	31.7±2.5
	90	23.3±1.2
	180	20.1±1.0
600	30	31.4±1.7
	60	29.4±2.5
	90	21.1±1.6
	180	15.2±1.3
700	30	27.2±2.5
	60	25.2±0.6
	90	16.0±1.6
	180	15.0±1.1

Changing in metal concentration during dynamic pyrolysis

The rise in the metal concentrations during heat treatment is almost proportional to the decrease in the weight of the sample.

The data in Table 5 and Figure 13 show that the weight of the samples treated at 500˚C and 600˚C does not differ significantly. The reason is that there are no significant differences between the decomposition reactions that occur at these temperatures. The decomposition of most of the organic materials occurs before 500°C, such as the decomposition of the PVDF. This was confirmed by Kulia and coworkers who carried out a thermogravimetric study of PVDF under a nitrogen atmosphere and observed that PVDF exhibited a single degradation at 450°C, with a material loss of more than 80% of its weight before 500°C was reached [115].

At temperatures between 600 and 700°C, the oxidation of the C in CO and CO_2 leads to additional weight loss. The amount of CO increases with increasing temperature. At 700˚C, the

quantity of C reacting with oxygen to form CO and CO_2 is significantly higher than at lower temperatures (as shown in Figure 25). Furthermore, the constant flow of nitrogen removes CO and CO_2 from the system, thus the reaction equilibrium is not reached (see Figure 4).

Table 5: The w% of major elements in the untreated and dynamic pyrolyzed samples. The w% of the elements in the treated samples are calculated based on the weight of the samples after dynamic pyrolysis.

		w%						
T (°C)	**Time (min)**	Mn	Ni	Co	Cu	Li	Al	P
Untreated	0	11.0±0.7	5.6±0.3	5.5±0.3	12.3±0.8	2.4±0.2	6.8±0.5	0.3±0.1
400	30	11.4±0.3	6.0±0.3	5.7±0.3	12.9±0.1	2.6±0.3	7.1±0.3	0.3±0.1
	60	11.6±0.2	6.2±0.3	5.8±0.1	13.1±0.2	2.6±0.1	7.3±0.1	0.3±0.3
	90	11.8±0.2	6.3±0.3	5.9±0.3	13.4±0.3	2.7±0.3	7.4±0.3	0.3±0.2
	180	12.5±0.2	6.5±0.2	6.3±0.1	13.8±0.3	2.9±0.2	7.4±0.2	0.3±0.2
500	30	11.7±0.3	5.9±0.3	5.7±0.3	13.0±0.3	2.8±0.2	6.0±0.3	0.3±0.1
	60	12.8±0.5	6.1±0.3	6.3±0.3	13.4±0.2	2.8±0.3	7.1±0.2	0.3±0.1
	90	13.2±0.3	6.7±0.3	6.6±0.3	15.3±0.1	3.1±0.3	7.5±0.3	0.3±0.2
	180	13.7±0.3	6.6±0.4	6.5±0.3	15.3±0.1	3.1±0.2	7.7±0.1	0.3±0.2
600	30	11.7±0.2	6.2±0.3	5.7±0.3	12.5±0.1	2.7±0.2	7.4±0.3	0.3±0.1
	60	12.6±0.1	6.3±0.1	6.1±0.1	13.6±0.2	2.4±0.3	7.3±0.3	0.4±0.1
	90	13.2±0.3	6.7±0.3	6.6±0.3	14.4±0.3	3.1±0.3	9.9±0.3	0.4±0.1
	180	14.4±0.3	7.4±0.3	7.0±0.3	15.0±0.0	3.6±0.3	10.5±0.3	0.4±0.1
700	30	12.0±0.1	6.5±0.1	5.9±0.1	13.6±0.3	2.9±0.1	8.2±0.1	0.4±0.1
	60	12.2±0.1	7.0±0.3	6.2±0.3	14.3±0.1	3.0±0.3	10.1±0.1	0.4±0.2
	90	14.2±0.3	7.1±0.2	6.7±0.3	15.1±0.3	3.0±0.3	10.3±0.2	0.4±0.1
	180	14.2±0.3	7.5±0.2	7.1±0.3	15.3±0.3	3.6±0.3	10.7±0.2	0.4±0.1

Change in the phase composition during dynamic pyrolysis

The carbothermic reduction of the oxides modified the microstructural composition of the samples composed of a mix of both cathode and anode material. In Figure 14, the XRD spectrum of the untreated battery is compared with the spectra for the samples treated by dynamic pyrolysis for 90 minutes.

Making quantitative assumptions based on these spectra is incorrect, but it is evident that an increase in the treatment temperature leads to a decrease in the intensity of the peaks at 26.5°, 43.3 °, and 54.9°, which are the diffraction peaks from the graphitic carbon.

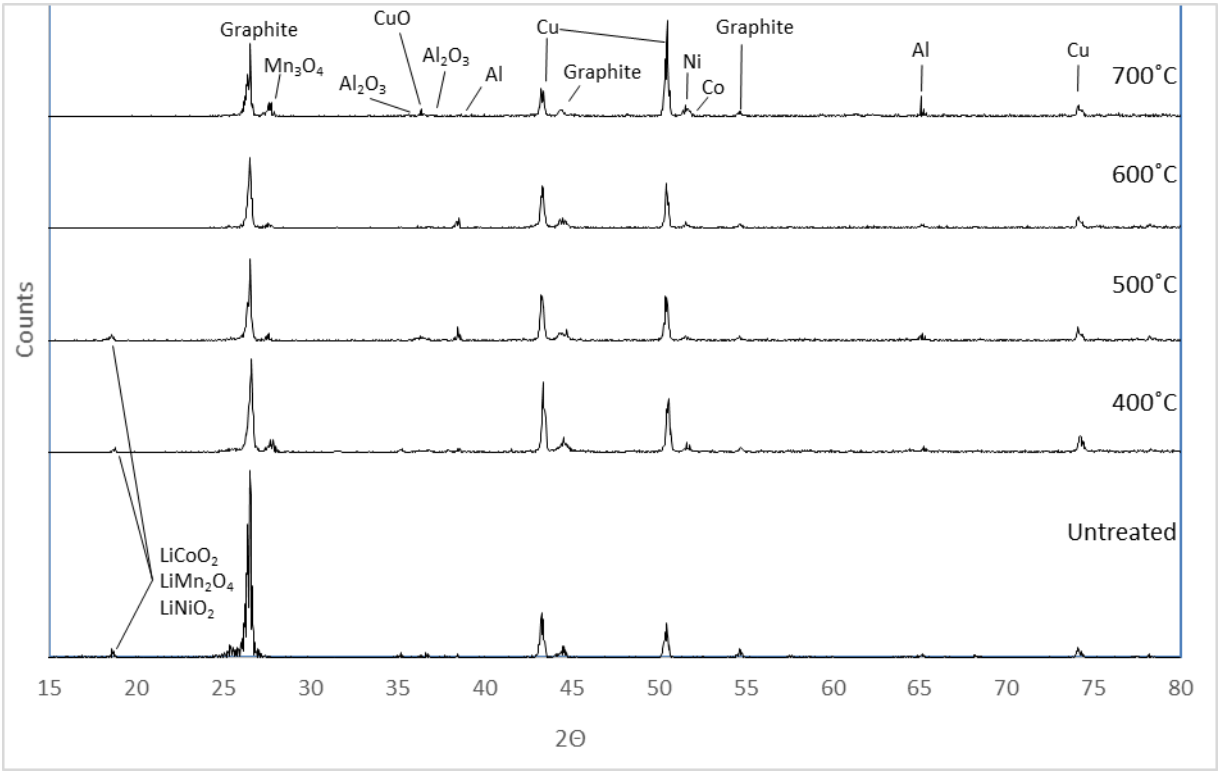

Figure 14: Comparison between the XRD spectra of an untreated sample and the spectra of samples pyrolyzed for 1.5 h at 400°C, 500°C, 600°C, and 700°C.

The diffraction peak at 18.7˚, which is common for all three lithium-metal oxides, is present in the diffractogram for the sample treated at a temperature lower than 500°C, but it was not detected for samples treated at higher temperatures. Comparing the spectra of samples exposed to dynamic pyrolysis at 700°C for different times (Figure 15), the peak at 18.7˚ disappears only after 90 minutes. So, the treatments at 600°C and 700°C for 90 minutes seem to be enough to obtain the almost complete carbothermic reduction of the active material. The signals of the carbothermic products, such as metals in elemental form Ni, Cu, and Co, were identified in the peaks at 50.5° and 74°.

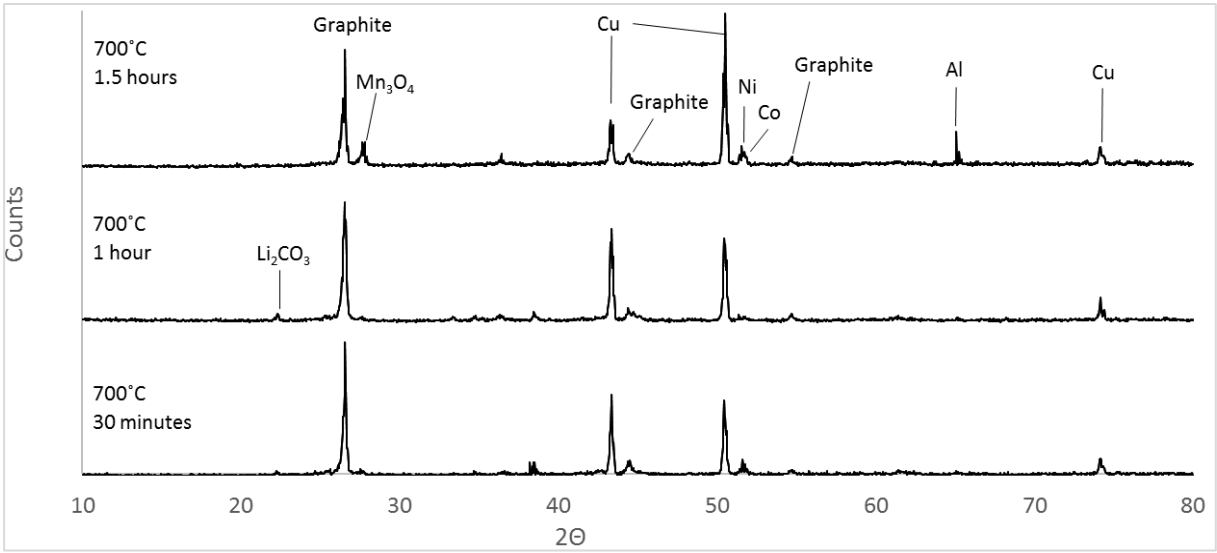

Figure 15: Comparison between XRD spectra of pyrolyzed samples at 700°C for 30 minutes, 60 minutes, and 90 minutes.

The metal species have diffraction peaks at similar 2Θ angles, and this limits the data resolution. To obtain a better identification of the compounds, XRD spectra of standard samples, i.e. pure metal oxides, mixed with graphite and treated by pyrolysis at 700°C, were collected (Figure 16).

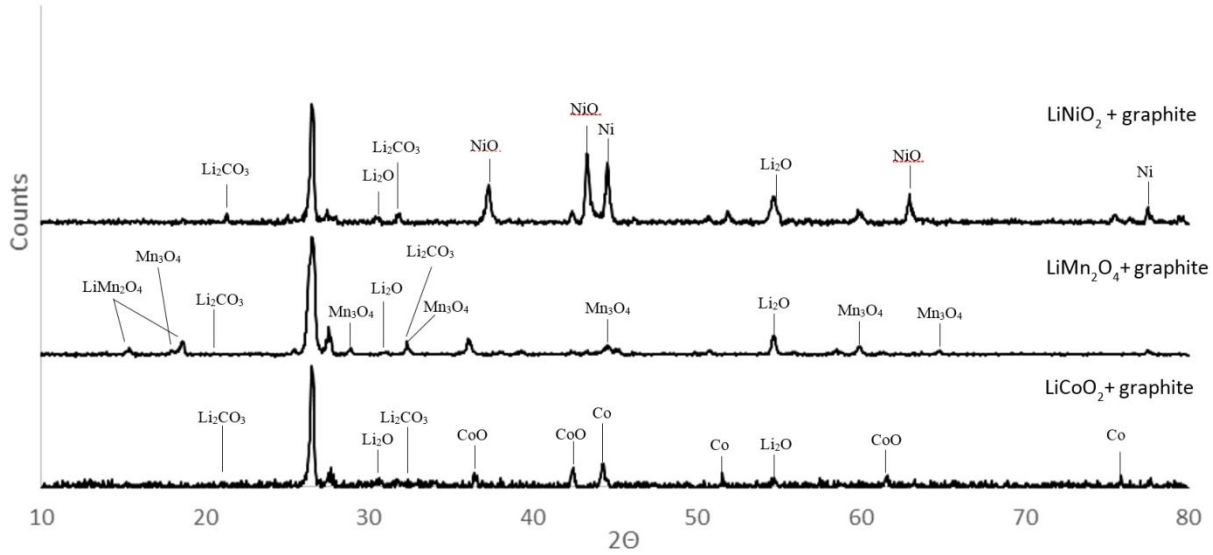

Figure 16: Comparison of XRD spectra for standard samples, consisting of a mixture of graphite and one of the oxides ($LiCoO_2$, $LiMn_2O_4$, and $LiNiO_2$.) pyrolyzed for 1.5 h at 700°C.

The XRD results confirmed the proposed hypothesis presented in this work through thermodynamic calculation (see Figure 3) about the reaction mechanisms involved during the thermal treatment.

The XRD spectrum of the mixture of $LiCoO_2$, pyrolyzed with excess graphite at 700°C for 90 minutes indicates the presence of Li_2CO_3, CoO, and Co. This data confirms that reactions (16), (17), and (18) correctly describe the carbon induced reduction.

$$16LiCoO_2(s) + 10C(s) \rightarrow 12Co(s) + Co_3O_4(s) + CoO(s) + 8Li_2CO_3(s) + CO(g) + CO_2(g) \quad (16)$$

$$2LiCoO_2(s) + 3/10C(s) + CO(g) \rightarrow 9/10Co(s) + 3/10Co_3O_4(s) + 3/10CoO(s) + Li_2CO_3\,(s) + 3/10CO_2(g) \quad (17)$$

$$9/10Co_3O_4(s) + 34/25C(s) + CO(g) \rightarrow 14/5Co(s) + 12/5CO_2(g) \quad (18)$$

The presence of CoO was not expected, as even if the reduction of CoO to metal Co by C and CO, described by reaction (19), is permitted thermodynamically, there was no complete decomposition of CoO. The reason might be the kinetics of this decomposition reaction and/or that the gas flow transporting CO and CO_2 out of the system is limiting the contact between the gas and the solid.

$$3CoO(s) + C(s) + CO(g) \rightarrow 3Co(s) + 2CO_2(g) \quad (19)$$

Li_2O, Li_2CO_3, and Mn_3O_4 are the products of the reaction between graphite with $LiMn_2O_4$, as shown in reaction (30). No reduction to form MnO or MnO_2, as described in the thermodynamic considerations by the reactions (20), and (21), could be observed.

$$6LiMn_2O_4(s) + 4C(s) + CO(g) + O_2(g) \rightarrow 4Mn_3O_4(s) + 3Li_2CO_3(s) + CO_2(g) \quad (30)$$

$$10LiMn_2O_4(s) + 7C(s) \rightarrow 16MnO(s) + Mn_3O_4(s) + MnO_2(s) + 5Li_2CO_3(s) + CO(g) + CO_2(g) \quad (20)$$

$$2LiMn_2O_4(s) + 1/2C(s) + CO(g) \rightarrow 2MnO(s) + 1/2Mn_3O_4(s) + 1/2MnO_2(s) + Li_2CO_3(s) + 1/2CO_2(g) \quad (21)$$

The XRD spectra of $LiNiO_2$ confirms the reduction to NiO and Ni, as described by (27), (28), and (29). The time and temperature of treatment did allow the complete decomposition of NiO into Ni and the reaction between the total amounts of Li_2O with CO_2.

$$8LiNiO_2(s) + 6C(s) \rightarrow 7Ni(s) + NiO(s) + 4Li_2CO_3(s) + CO_2(g) + CO(g) \quad (27)$$

$$2LiNiO_2(s) + 2/3C(s) + CO(g) \rightarrow 4/3Ni(s) + 2/3NiO(s) + Li_2CO_3(s) + 2/3CO_2(g) \quad (28)$$

$$3NiO(s) + C(s) + CO(g) \rightarrow 3Ni(s) + 2CO_2(g) \quad (29)$$

4.2.2 Scrap NMC-LiBs cell cathodes (Paper III)

Change in the phase composition during dynamic and under vacuum pyrolysis

All the detected peaks in the XRD spectrum of the untreated cathode active material (Figure 40) are due to the presence of the $Li(Ni_xMn_yCo_z)O_2$.

In the spectra of the cathode active materials subjected to vacuum pyrolysis at 450°C and 550°C, significant differences were not observed when compared with the spectra of untreated material. This indicates that such a thermal treatment does not change the elemental composition of the active material or the crystalline compounds present in it (Figure 17a). Only after vacuum pyrolysis carried out at 650°C for 90 minutes, it was possible to detect the signals of Li_2CO_3, Mn_3O_4, Co_3O_4, and NiO (Figure 17b).

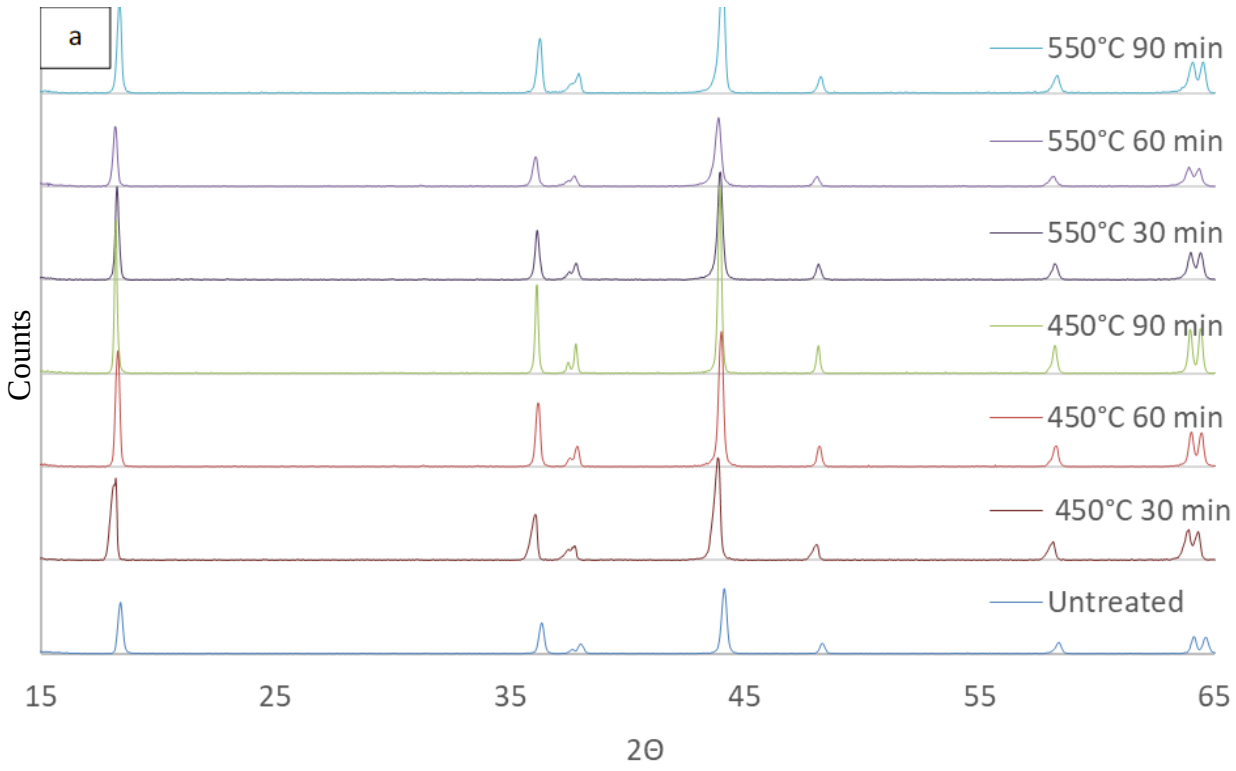

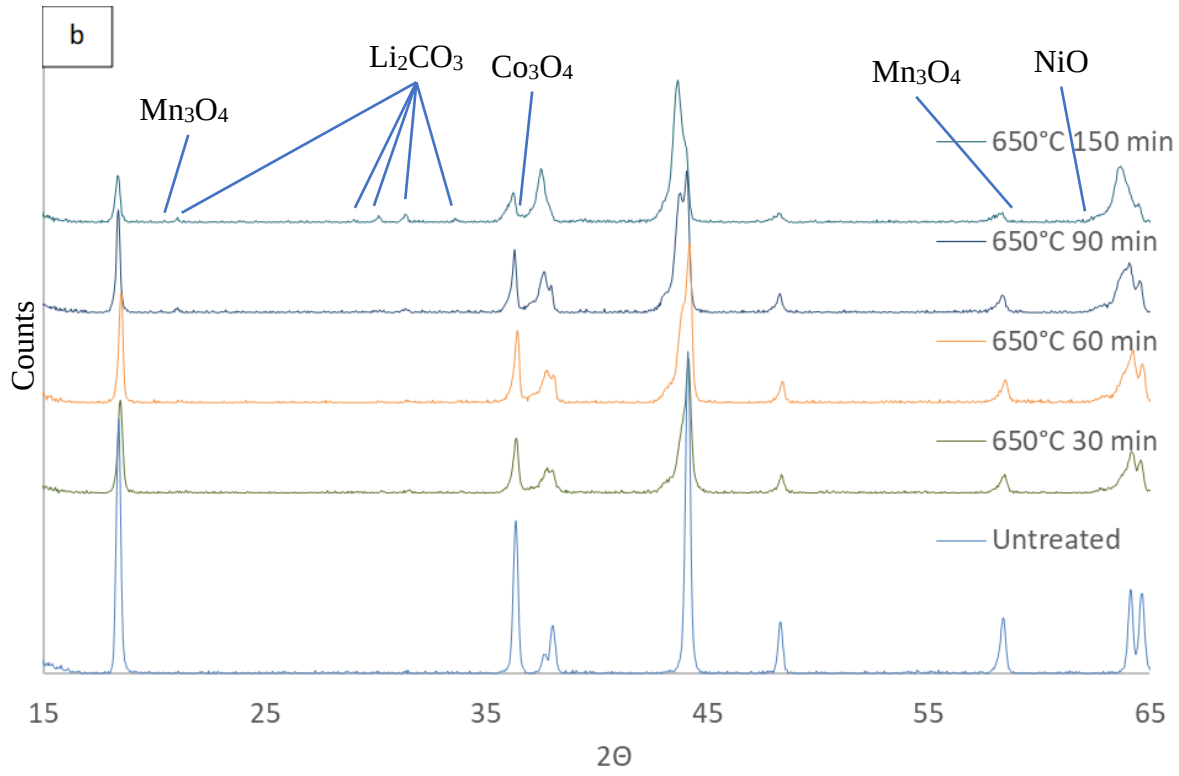

Figure 17a, b: Comparison between the XRD spectra of an untreated sample and the spectra of samples thermally treated under vacuum conditions for 30, 60, 90, or 150 minutes at 450°C, 550°C, or 650°C.

The same carbothermic reduction products were observed at as low a temperature as 450°C in the samples pyrolyzed under inert gas, Figure 18. It may be concluded that the constant flow of nitrogen in the system during pyrolysis promotes the carbothermic reaction, bringing the CO_2 that was produced during the reduction out of the system.

The peaks at 18° and 44° are typical of the $Li(Ni_xMn_yCo_z)O_2$ compounds. Their presence in the spectra even after 150 minutes of treatment at all temperatures indicates that the conditions of treatment are not severe enough or the quantity of carbon was not high enough to give a complete reduction of the metal oxides. Indeed, Li et al. [64] have proved that by carrying out pyrolysis at higher temperature, 1000°C for 30 min, and adding graphite to obtain a molar ratio $LiCoO_2$/ graphite of at least 4/3, it is possible to push the reduction of $LiCoO_2$ to form metallic Co and Li_2CO_3. Also, Xiao et al. [116], performing vacuum pyrolysis on NMC-LiB, observed that it is possible to reduce $LiCoO_2$ and $LiMn_2O_4$ to metallic Co and MnO by performing a thermal treatment at a temperature slightly higher, 700°C, and adding the graphite removed from the LiB anodes.

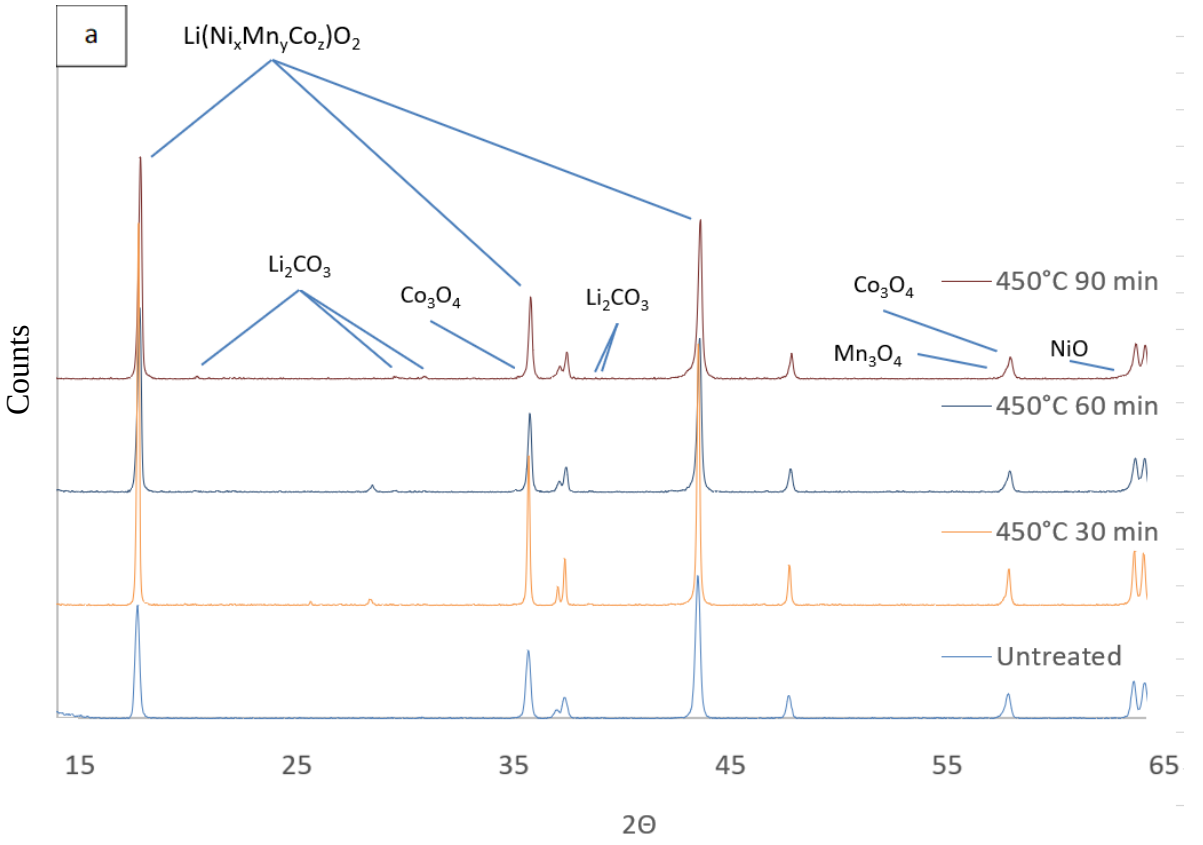
a
Li(NixMnyCoz)O2
Li2CO3
Co3O4
Li2CO3
Co3O4
Mn3O4
NiO
450°C 90 min
450°C 60 min
450°C 30 min
Untreated
Counts
15
25
35
45
55
65
2Θ

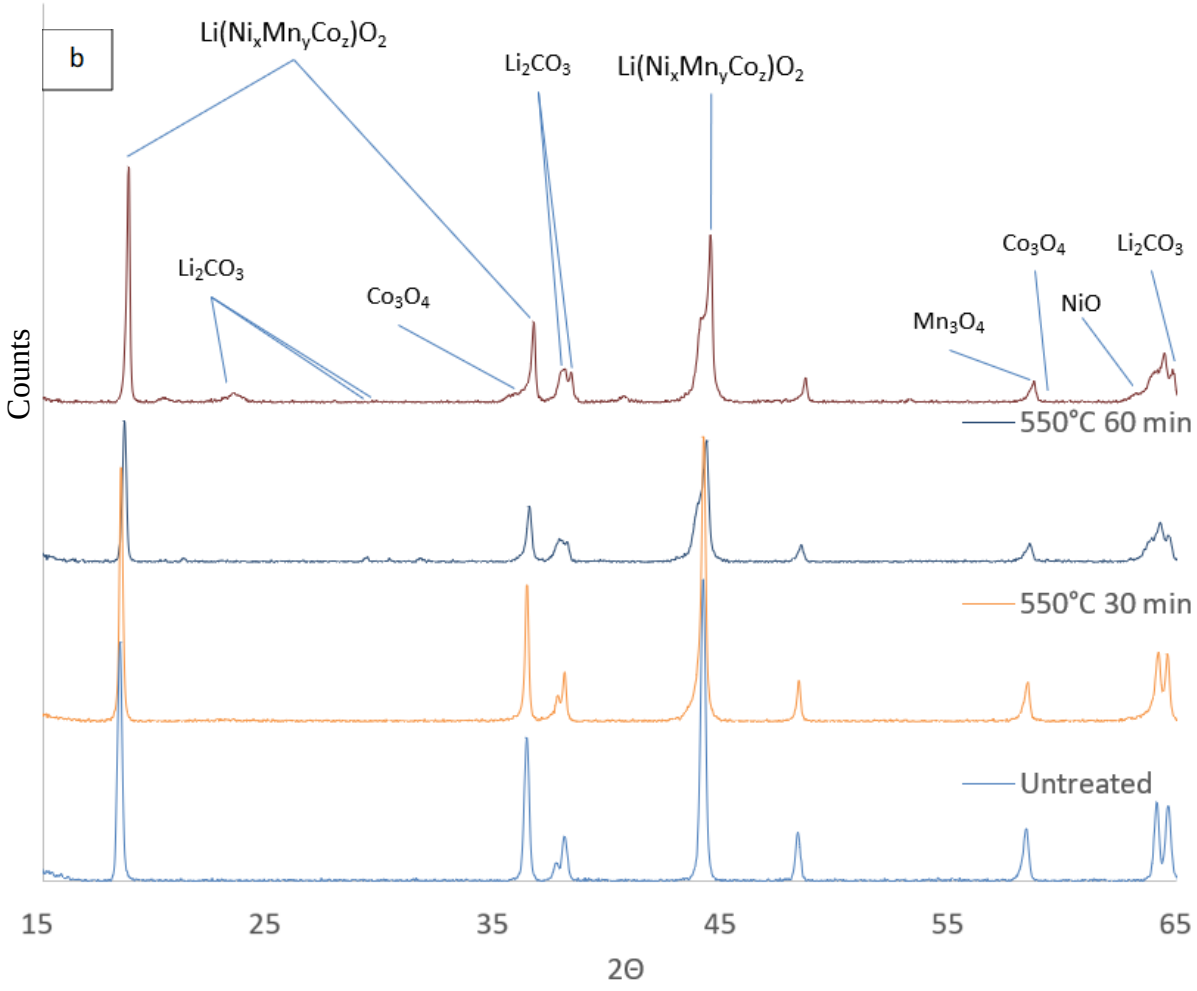
b
Li(NixMnyCoz)O2
Li2CO3
Li(NixMnyCoz)O2
Li2CO3
Co3O4
Co3O4
Li2CO3
Mn3O4
NiO
550°C 60 min
550°C 30 min
Untreated
Counts
15
25
35
45
55
65
2Θ

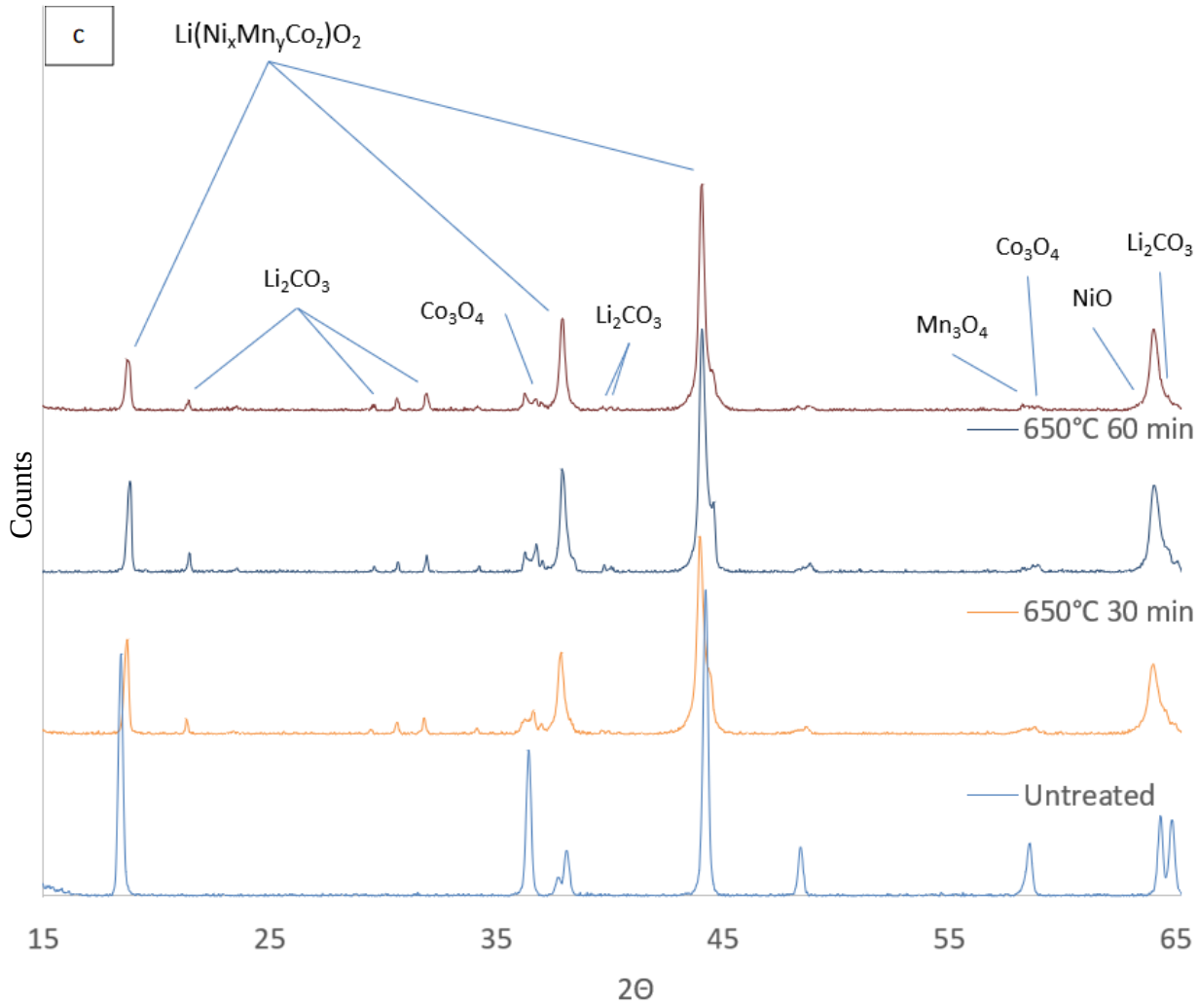

Figure 18a, b,c: Comparison between the XRD spectra of an untreated sample and the spectra of samples pyrolyzed for 30, 60, or 90 minutes at 450°C, 550°C, or 650°C.

Effects of dynamic pyrolysis and pyrolysis under vacuum on the morphology and particle size of active cathode material.

The study of the effects of the thermal treatment on the morphology and particle size of cathode active material separated from the current collector is important for the subsequent leaching and/or possible regeneration for lithium-ion batteries. The untreated samples (Figure 19a) appear to be composed of particles of an irregular shape with a dimension <2µm. They are grouped in disorganized clusters and organized globular particles. The morphology of the dynamic pyrolyzed samples looks to be only slightly affected by the treatment. Indeed, it is composed of smaller globular particles (Figure 19b). In contrast, the vacuum pyrolysis causes a significant decrease in the number of globular particles and the samples look to be composed

of only irregular-shaped particles without any kind of grouping scheme and with smaller size when comparing with the other samples (Figure 19c).

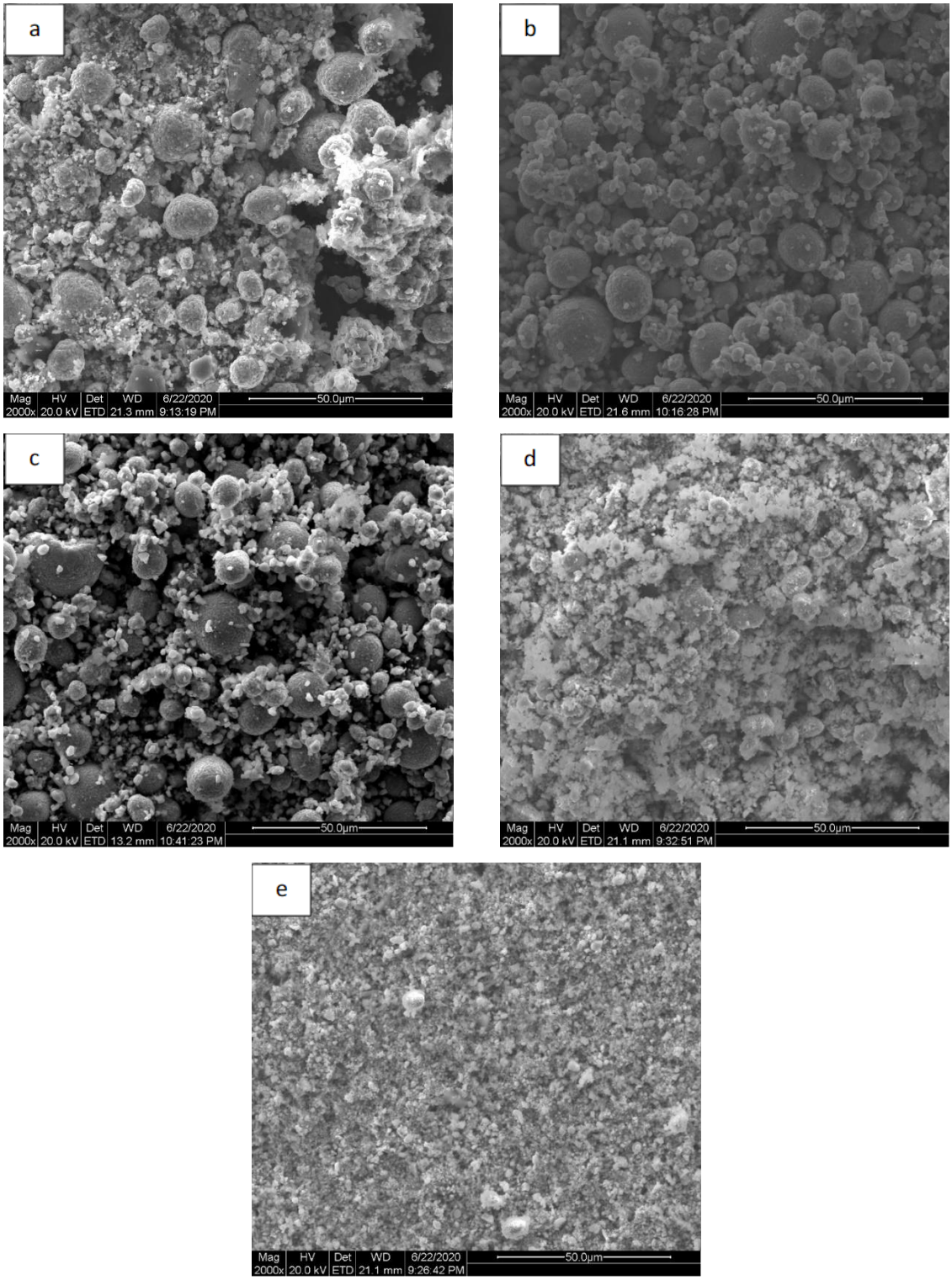

Figure 19: SEM images of cathode active material separated from a)untreated sample, b) sample pyrolyzed under inert gas at 550ºC for 30 min, c) sample pyrolyzed under inert gas at 550ºC for 90 min, d) sample pyrolyzed under vacuum at 550ºC for 30 min, f) sample pyrolyzed under vacuum at 550ºC for 90 min.

The increasing time of treatment does not have evident effects on the morphology except for the samples subjected to vacuum pyrolysis, for which the dimension of the irregular-shaped particles is reduced.

Mechanical separation of black mass from the Al layer without and after dynamic, as well as after vacuum pyrolysis

The thermal treatments induced the decomposition of the PVDF and this made it easier to remove the cathode material from the metal foils.

The efficiency of active material removal from the Al foils through a mechanical treatment performed in a ball mill was studied. Only 15.8 w% of the cathode material could be separated from samples that had not been thermally treated. The results further showed that higher temperature and longer duration times used in the thermal treatment increased the separation efficiency in the milling. (Figure 20).

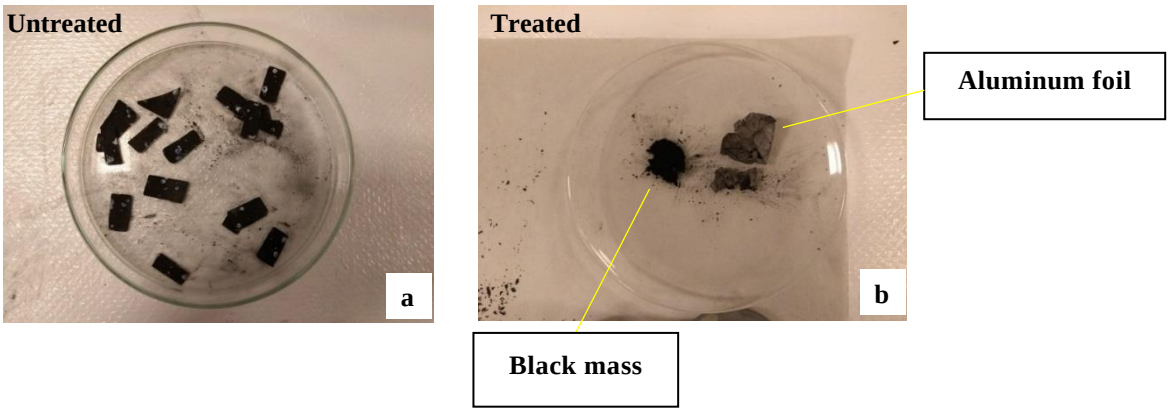

Figure 20: (a) Untreated samples subjected to mechanical treatment, (b) thermally treated samples subsequently subjected to mechanical treatment.

The milling after the pyrolysis showed a complete separation only when a period of 150 minutes of heat treatment had been applied. After thermal treatment under inert gas, the quantity of active material removed increased from ~56 w%, after 30 minutes of treatment at 450˚C, to its maximum at ~98 w% at 550˚C for 90 minutes (Figure 21a). Instead, after vacuum pyrolysis, the active material removed by milling increased from ~47 w% after 30 minutes of treatment at 450˚C to 98 w% at 650˚C after 90 minutes of treatment (Figure 21b).

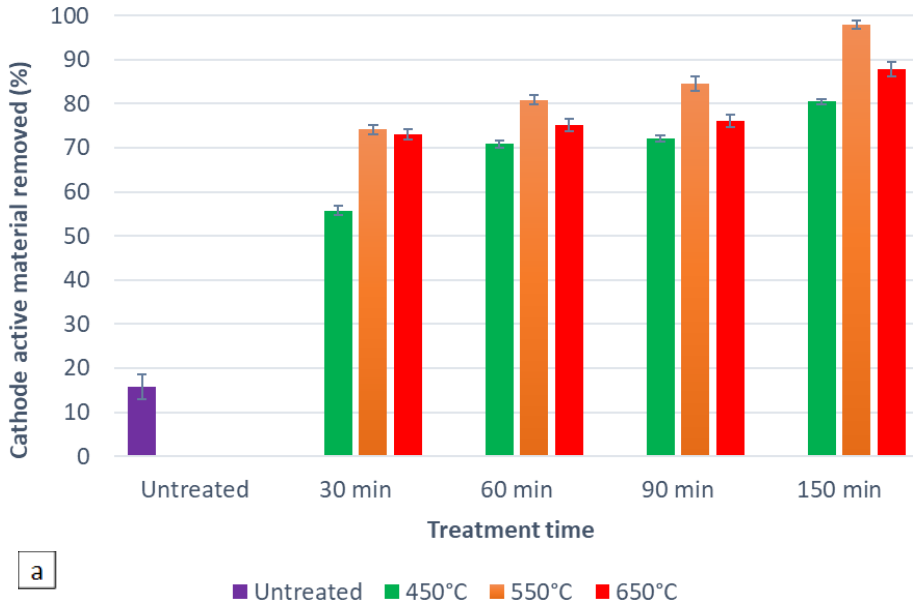

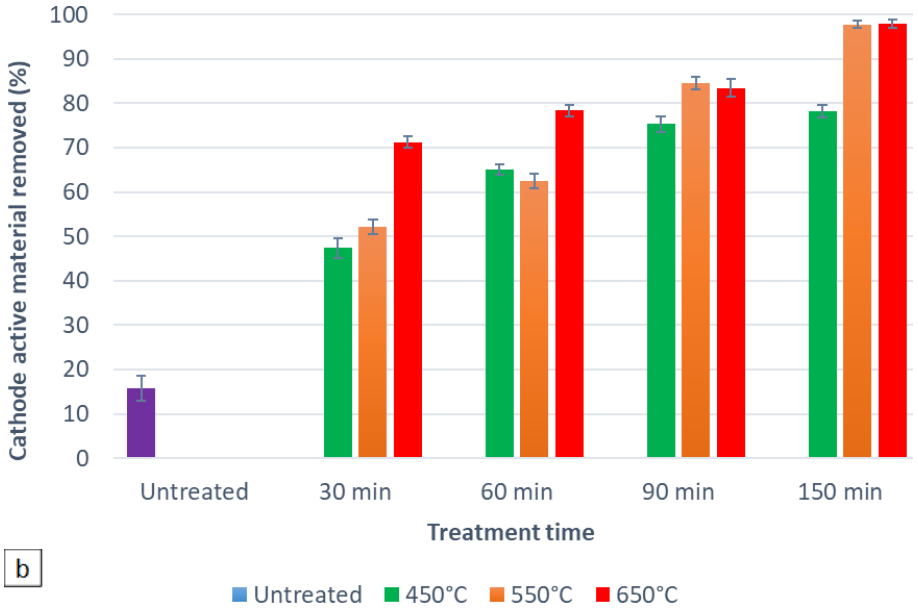

Figure 21: Comparisons between cathode active material recovered after 15 minutes of milling from the untreated samples with the quantity recovered from samples a) pyrolyzed under inert gas and b) subjected to vacuum pyrolysis.

The quantity of active material removed through milling was significantly higher for the samples treated for 90 minutes at 550˚C than for those treated at 650˚C after dynamic pyrolysis. The main reason for this is the partial melting of the Al foil (melting point 660.3°C). At 650˚C, Al melt covered the cathode material and inhibited PVDF removal.

The quantity of materials removed through milling after dynamic pyrolysis reached over 80 w% after treatment at 550°C for 60 minutes. By contrast, to reach the same value of material

removed by vacuum pyrolysis, it is necessary to treat the samples at a temperature above 550°C for at least 90 minutes, so the rate of removal is lower in that experiment setting. This is due to the presence of the N_2 flow, which constantly carried the PVDF decomposition products away from the furnace, thus promoting its decomposition.

The formation of a layer of Al_2O_3 on the surface of the Al foil during the thermal treatment leads to an increased brittleness of the Al foil. It could also lead to increased contamination of the removed cathode active material by aluminum powder. The Al content in the cathode active material recovered after milling (Table 6) decreased with the time and temperature of treatment. Indeed, the highest concentration of Al was detected in the cathode active material recovered from the untreated samples after milling, 5.15 w%. This trend is probably caused by the strong cohesion between the active material and the Al foil due to the presence of the PVDF. In the untreated samples, the adhesion is so strong that Al powder remains attached to the separated active material. The increase of temperature and time of treatment determines the decomposition of the PVDF and the reduction of the adhesion.

Table 6: Aluminium content in the cathode active material recovered after milling (w%).

		Al content after milling (w%)			
		30 minutes	60 minutes	90 minutes	150 minutes
Dynamic pyrolysis	450°C	4.1±0.1	3.8±0.1	3.1±0.2	2.1±0.2
	550°C	3.5±0.2	1.7±0.1	1.4±0.2	1.1±0.1
	650°C	2.6±0.2	1.4±0.1	1.3±0.2	1.0±0.1
Vacuum pyrolysis	450°C	0.8±0.1	0.8±0.1	0.7±0.1	0.6±0.1
	550°C	0.6±0.1	0.6±0.1	0.3±0.1	0.3±0.1
	650°C	0.4±0.1	0.34±0.1	0.2±0.1	0.2±0.1
Untreated		5.2±0.2			

To summarize, pyrolysis of a mix of NMC-LiB cathodes and anodes was shown to effectively trigger the carbothermic reduction of the lithium-metal-oxides. Co, Mn, and Ni oxides were reduced to a lower oxidation state and/or more soluble forms. The graphite already coated on the surface of the anode metal layers was more than enough to complete the reduction. The addition of an extra reducing agent was not necessary. The remaining part of graphite, which was not involved in the carbothermic reduction, can be recovered after leaching as a solid residue.

Furthermore, decomposition of the PVDF binder was achieved, making the separation of the active material from the metal foils more feasible.

4.3 Incineration

4.3.1 Spent NMC-LiBs cells (Paper II)

Change in sample weight during incineration

The Δw% is more consistent during incineration than during pyrolysis, with a significant weight loss in the first 15 minutes of treatment (Figure 22).

At 400ºC and 500ºC, the weight loss during 30 and 90 minutes of incineration increased almost proportionally with the treatment time. In contrast, the weight of the sample did not change at 700ºC after 90 minutes of treatment (Δw% ~35%). This is due to the almost complete removal of the C content during the first 90 minutes. Indeed, after 180 minutes, at 700 ºC the weight loss slightly increased to ~37% and the samples treated at both 600 ºC and 500 ºC reached the same value.

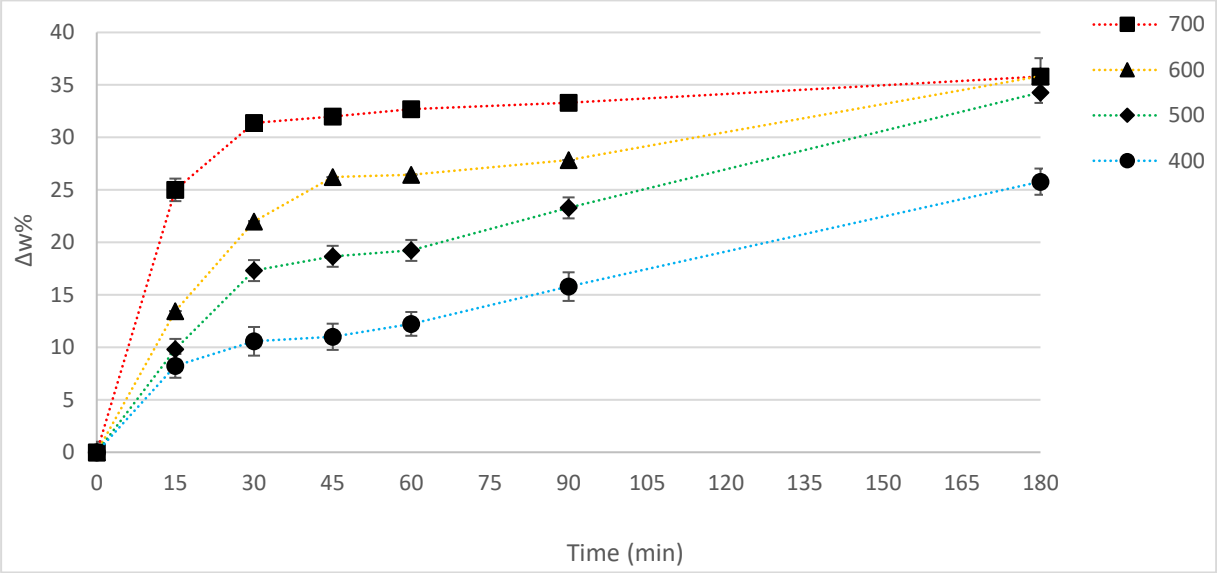

Figure 22: Weight loss in incineration at different temperatures and times. The (0;0) point corresponds to the untreated material. The lines are only provided to guide the eye.

The carbon content in the remaining material after incineration at 700°C for 90 or 180 minutes (Table 7) is less than 1%, from an initial 41% in the untreated battery.

Table 7: Change of the carbon content in the sample depending on the time and temperature of incineration.

T (°C)	Time (min)	Carbon content (w%)
Untreated	**0**	40.8±2.8
400	30	29.6±1.4
	60	25.0±1.5
	90	19.1±2.3
	180	15.3±1.3
500	30	24.0±2.2
	60	21.5±1.2
	90	15.7±1.2
	180	11.7±0.2
600	30	16.0±1.3
	60	11.9±1.0
	90	5.5±1.0
	180	0.8±0.2
700	30	5.3±0.9
	60	2.2±0.2
	90	0.6±0.2
	180	0.6±0.1

Change of metal concentrations in cathode materials during incineration

The increase of the temperature and time of treatment promotes the oxidation of the carbon content and results in a rise in the concentrations of the metals in the samples (Table 8). Comparing the untreated sample with the sample treated at 700°C for 180 minutes, the data show that the concentration of each metal increased by about ~40%, almost proportional to the decrease in the weight of the sample (Figure 22).

Table 8: The w% of major elements in the untreated and incinerated samples.

		w%						
T (°C)	**Time (min)**	Mn	Ni	Co	Cu	Li	Al	P
Untreated	0	11.0±0.7	5.6±0.3	5.5±0.3	12.3±0.8	2.4±0.2	6.8±0.5	0.3±0.1
400	30	12.2±0.1	6.2±0.1	6.1±0.1	14.2±0.1	2.6±0.1	7.0±0.1	0.3±0.1
	60	12.8±0.2	6.3±0.2	6.5±0.1	15.4±0.1	2.6±0.1	7.9±0.2	0.3±0.1
	90	13.2±0.2	6.5±0.2	6.4±0.2	15.6±0.5	2.7±0.1	7.7±0.4	0.3±0.1
	180	14.3±0.3	7.2±0.2	7.1±0.3	15.9±0.3	3.6±0.3	10.7±0.2	0.4±0.1
500	30	12.9±0.2	6.8±0.1	6.2±0.4	15.6±0.3	2.7±0.1	7.9±0.3	0.3±0.1
	60	13.1±0.2	6.9±0.2	6.6±0.3	15.9±0.4	3.4±0.1	8.1±0.5	0.4±0.1
	90	14.3±0.2	6.9±0.1	6.8±0.1	16.9±0.3	3.6±0.1	8.7±0.2	0.4±0.1
	180	15.5±0.2	7.6±0.0	7.7±0.0	17.3±0.1	3.8±0.1	9.4±0.3	0.4±0.1
600	30	13.4±0.2	6.8±0.2	6.3±0.1	15.3±0.5	2.6±0.1	7.4±0.1	0.4±0.1
	60	13.8±0.3	7.6±0.1	6.6±0.5	16.6±0.3	2.8±0.1	8.0±0.4	0.4±0.1
	90	14.2±0.3	7.5±0.2	7.3±0.1	16.9±0.1	3.8±0.1	8.8±0.1	0.4±0.1
	180	15.5±0.2	7.6±0.0	7.7±0.0	17.3±0.1	3.8±0.1	9.4±0.3	0.4±0.1
700	30	13.9±0.2	6.9±0.1	6.8±0.1	16.3±0.2	2.9±0.1	8.7±0.3	0.4±0.1
	60	14.2±0.3	7.4±0.1	7.3±0.3	16.5±0.1	2.9±0.1	9.7±0.5	0.4±0.1
	90	15.0±0.4	7.7±0.1	7.6±0.1	17.0±0.5	3.2±0.1	9.8±0.3	0.4±0.1
	180	15.5±0.4	7.9±0.0	7.8±0.0	17.3±0.3	3.4±0.1	9.8±0.1	0.4±0.1

Change in the composition of the crystalline compounds of the cathode material during incineration

The intensity of the peaks at 26.5°, 43.3°, and 54.9° in the XRD spectra in Figure 23, which come from the graphitic carbon, clearly decreases with the rise in the treatment temperature. These peaks almost disappear after 90 minutes of treatment at 700°C. Under these conditions, the graphite and organic substances are likely totally consumed with the formation of volatile species.

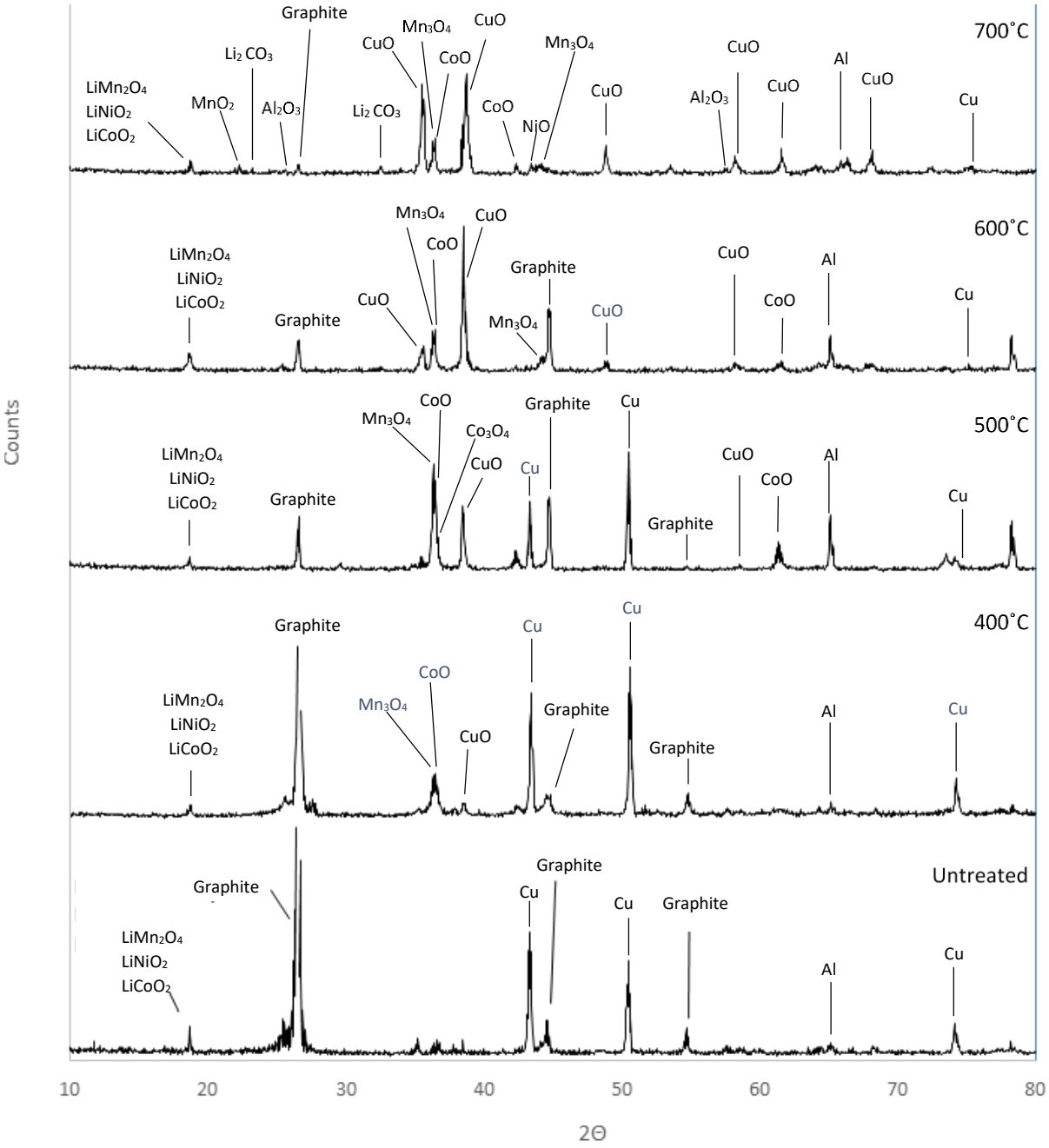

Figure 23: Comparison between the XRD spectrum of an untreated sample and the XRD spectra of the samples incinerated for 1.5 h at 400°C, 500°C, 600°C, and 700°C.

The airflow causes oxidation of the Cu foil. The two strong peaks at 2Θ 35.5 and 38.7 degrees correspond to the most prominent diffraction peaks for CuO:

$$2Cu(s) + O_2(g) \rightarrow 2CuO(s) \quad (31)$$

The signal at 2Θ=18˚ is common for all three lithium-metal oxides and was observed for samples treated at all temperatures. This indicates that it was not possible to obtain the complete reduction of these species. The reason is the kinetics for the oxidation of carbon compared to the kinetics of the carbothermic reduction. The presence and abundance of O_2 give rapid incineration of the C, limiting its reaction with the metal oxides. However, some products of the carbothermic reduction were detected: CoO, MnO_2, Mn_3O_4, and NiO. To perform a better identification of the signals, the XRD spectra of standard samples were collected for reference compounds (Figure 24).

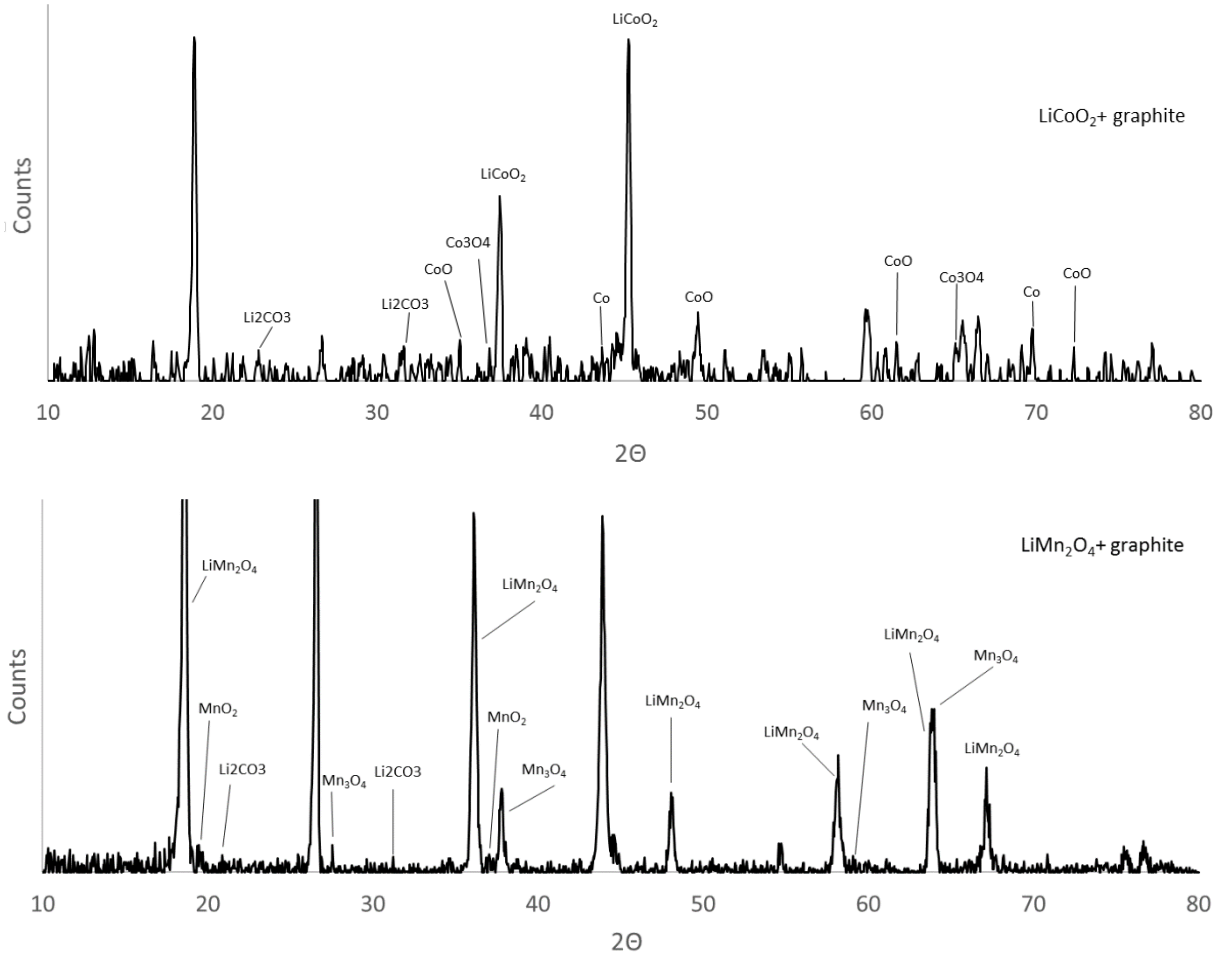

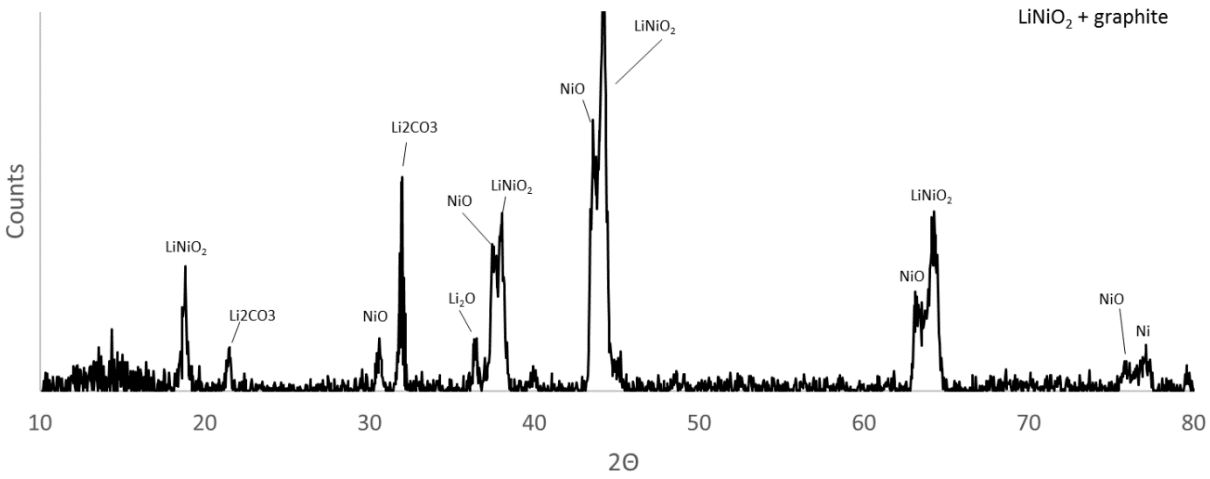

Figure 24: Comparison of the XRD diffractograms for standard samples, composed of a mixture of graphite and one of the oxides (LiCoO2 (a), LiMn2O4 (b), and LiNiO2 (c) Incinerated at 700°C for 1.5 h.

Incineration of $LiCoO_2$ into Li_2O, Li_2CO_3, CoO, Co_3O_4, and Co by graphite was expected from the thermodynamic considerations shown in reactions (7) and (8) (Figure 2). The presence of CoO and Co_3O_4 can be due to slow kinetics of their reduction reactions or can be due to oxidation of part of the Co formed by reaction with O_2. The higher concentration of O_2 compared to the concentration of CO promotes the oxidation reactions.

$$2LiCoO_2(s) + 2/5C(s) + CO(g) + 2/5O_2(g) \rightarrow 2/5Co(s) + 2/5Co_3O_4(s) + 2/5CoO(s) + Li_2CO_3(s) + 2/5CO_2(g) \quad (7)$$

$$4/5Co_3O_4(s) + 2C(s) + CO(g) + O_2(g) \rightarrow 12/5Co(s) + 3CO_2(g) \quad (8)$$

$LiMn_2O_4$ decomposed to MnO_2 and Mn_3O_4, reaction (32). No reduction to form MnO, as described in the thermodynamic considerations shown in reactions (11), (12), and (13), could be observed.

$$2\,LiMn_2O_4(s) + C(s) + CO(g) + O_2(g) \rightarrow Mn_3O_4(s) + MnO_2(s) + Li_2CO_3(s) + CO_2(g) \quad (32)$$

$$27/10LiMn_2O_4(s) + 13/10C(s) + CO(g) + O_2(g) \rightarrow MnO(s) + Mn_3O_4(s) + 13/10MnO_2(s) + 13/10Li_2CO_3(s) + CO_2(g) \quad (11)$$

$$2Mn_3O_4(s) + 7/4C(s) + CO(g) + 5/4O_2(g) \rightarrow 6MnO(s) + 11/4CO_2(g) \quad (12)$$

$$12/5MnO_2(s) + 19/10C(s) + CO(g) + 23/20O_2(g) \rightarrow 12/5MnO(s) + 29/10CO_2(g) \quad (13)$$

The X-ray diffractogram of the $LiNiO_2$ in Figure 24 shows that the reaction with C and O_2 gives Li_2O, Li_2CO_3, NiO, and Ni as its products, as shown in reactions (14) and (15) (Figure 2). Similar to the results obtained with the Co-containing compounds, the presence of NiO may be due to the oxidation of part of the Ni formed.

$$4LiNiO_2(s) + 2C(s) + CO(g) + O_2(g) \rightarrow Ni(s) + 3NiO(s) + 2Li_2CO_3(s) + CO_2(g) \quad (14)$$

$$12/5NiO(s) + 19/10C(s) + CO(g) + 23/20O_2(g) \rightarrow 12/5Ni(s) + 29/10CO_2(g) \quad (15)$$

4.3.2 Scrap NMC-LiBs cell cathodes (Paper III)

All the detected peaks in the XRD spectrum of the untreated cathode active material (Figure 25) are due to the presence of the $Li(Ni_xMn_yCo_z)O_2$. It is not possible to observe any significant difference when comparing this with the spectra of incinerated cathode active material. This indicates that thermal treatment does not change the composition or microstructure of the active material under incineration conditions. The O_2 reacts with the entire quantity of C in the samples, as described in reactions (2), (3), and (4), with CO and CO_2 as products carried out of the system by the constant airflow.

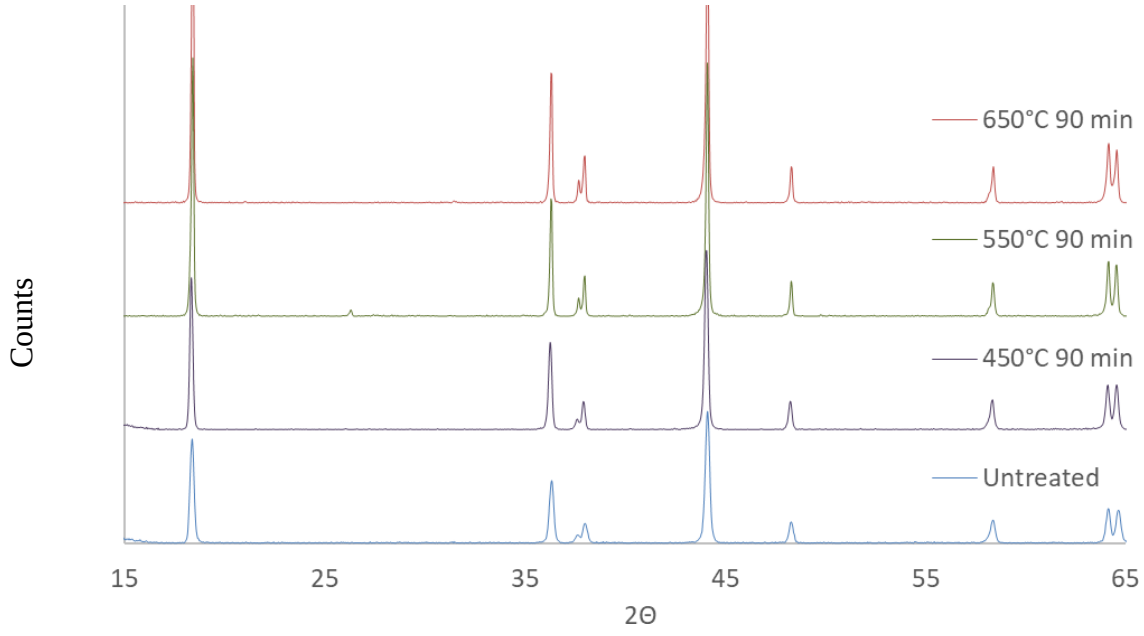

Figure 25: Comparison between the XRD spectra of an untreated sample and the spectra of samples incinerated for 90 minutes at 450°C, 550°C, and 650°C.

Effects on the morphology and particle size of active cathode material

Both the untreated samples and the samples subjected to incineration appear to be composed of particles of an irregular shape with dimension <2µm. They are grouped in disorganized clusters or as organized globular particles. This indicates that the morphology has not been affected by the incineration (Figure 26).

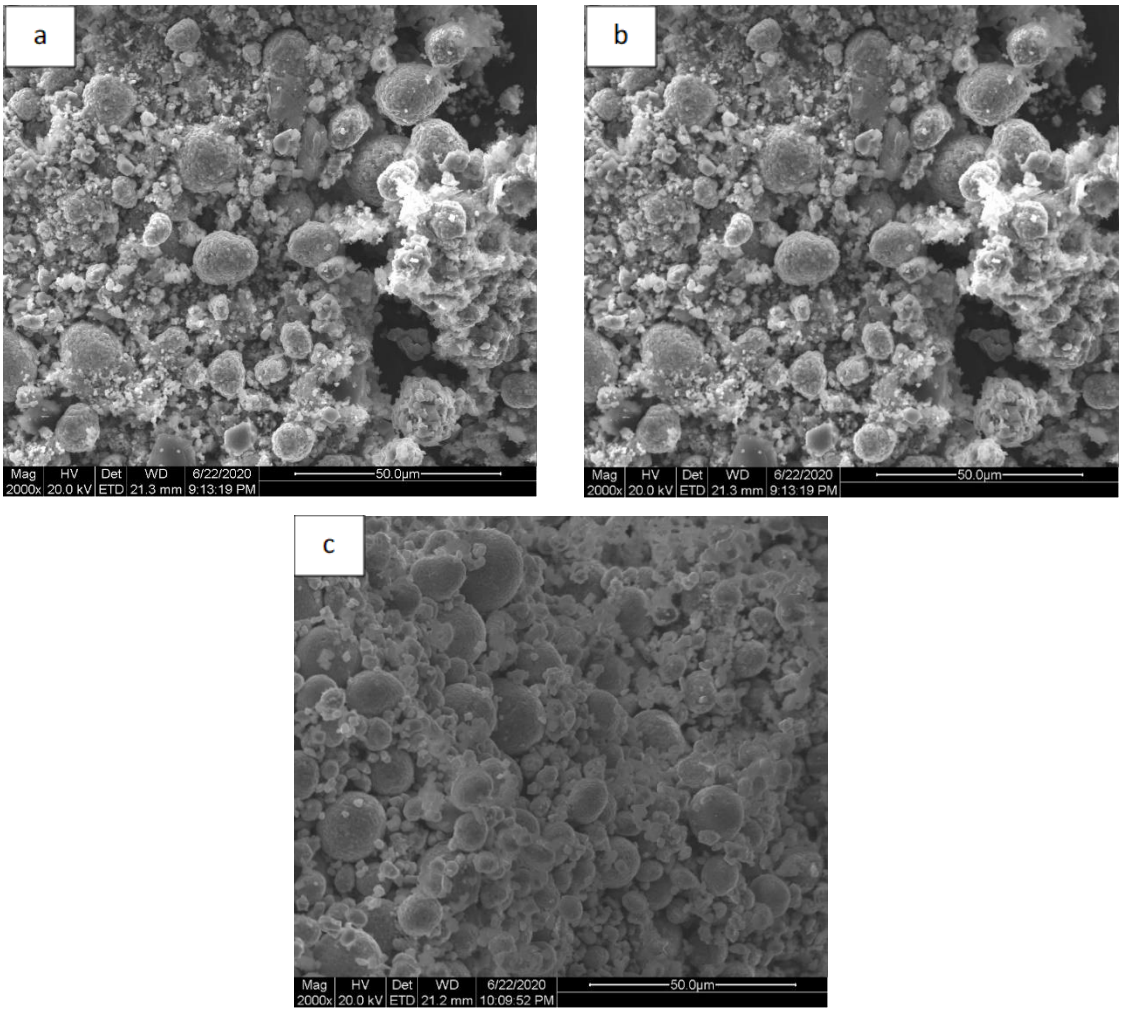

Figure 26: SEM images of cathode active material separated from a)untreated sample, b) sample incinerated at 550C for 30 min, c)sample incinerated at 550C for 90 min.

Mechanical separation of black mass from the Al layer without thermal treatment and after incineration

Increasing the time and temperature of thermal treatment positively affected the quantity of active material removed from the Al layer by ball milling. The plot in Figure 27 shows that

after 90 minutes at 550˚C an almost complete separation of active material is possible, with 98.6% of material removed; seven times higher than the quantity obtained from the untreated material.

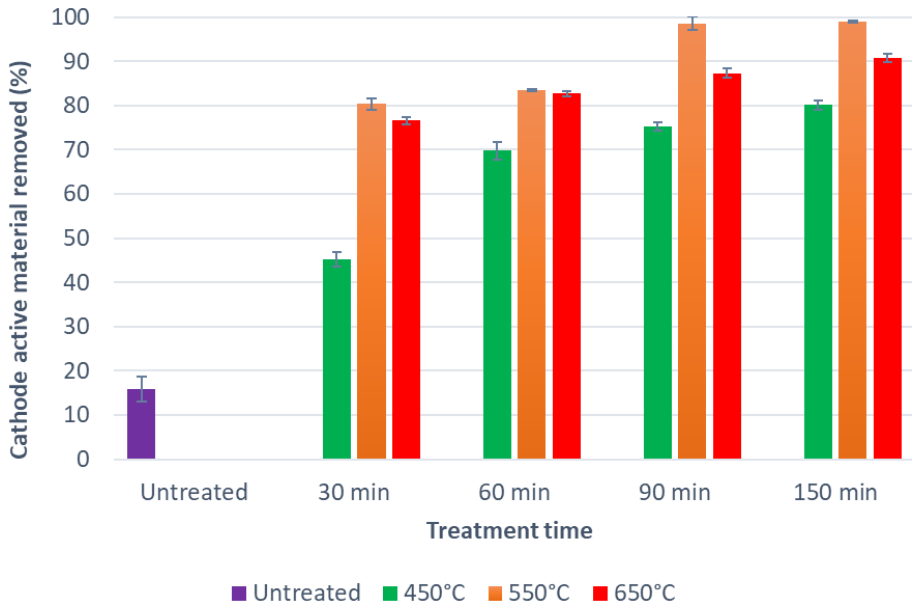

Figure 27: Comparison between cathode active material recovered after 15 minutes of milling from the untreated samples and the quantity recovered from incinerated samples.

As already described for the pyrolysis, during incineration the partial melting of the Al foil at 650 ˚C also inhibited PVDF removal, making the quantity of active material removed through milling higher for the samples treated for 90 minutes at 550˚C than for those treated at 650˚C.

During incineration, a layer of A_2O_3 on the surface of the Al foil is formed. The data presented in Table 9 show that the content of Al in the cathode active material recovered during milling increased with the time and temperature of heat treatment for the incinerated samples, reaching 4.62 w% after incineration at 650°C for 150 minutes. However, a higher concentration of Al was detected in the untreated removed cathode material, 5.15 w%.

Table 9: Al content in the cathode active material recovered after milling (w%).

		Al content after milling (w%)			
		30 minutes	60 minutes	90 minutes	150 minutes
Incineration	450°C	0.5±0.1	0.6±0.1	1.0±0.1	1.3±0.1
	550°C	0.9±0.1	2.0±0.2	3.0±0.1	3.1±0.2
	650°C	1.2±0.1	2.3±0.2	3.4±0.2	4.6±0.1
Untreated		5.2±0.2			

Incineration has allowed an almost complete decomposition of the graphite and organic species. Efficient separation of the active material and the Al foil was achieved over shorter times and at lower temperatures, so a more efficient decomposition of the PVDF than during pyrolysis was possible.

The concentration of C in the waste was enough to trigger a carbothermic reduction of the cathode active material. The O_2 in the gas flow causes oxidation of the Cu and Al foils, with the formation of CuO and Al_2O_3. The oxidation of the Al metal foils may introduce the need for extra steps in the hydrometallurgical recovery of valuable elements following the thermal treatment described in this work. On the other hand, the oxidation of Cu can increase its leachability, thus making it easier to recover in hydrometallurgical processes.

4.4 Analysis of by-products

4.4.1 FTIR analysis of the gas produced during the thermal treatment (Paper II)

The FTIR spectra of the gases produced during pyrolysis and incineration show the same peaks (Figure 28). The peaks for CO_2 at 2400 cm^{-1} and between 3750 and 3600 cm^{-1} as well as the double peaks of CO around 2125 cm^{-1} are intense. This shows that the atmosphere in the system was rich in CO and CO_2. This is caused by the carbothermic reaction of carbon from the organic components and graphite with residual oxygen, as well as oxygen from the metal oxides during pyrolysis. During incineration, there is also a contribution of O_2 present in the airflow. Comparing the two spectra in Figures 28a and 28b, the quantity of CO_2 detected during combustion is higher than that obtained during pyrolysis. The symmetric peaks at 1400-1800 and 3550 -3900 cm^{-1} are typical when H_2O is present as water vapor in the system. The spectra of gas samples collected during incineration at 700°C at different times after the start of treatment, Figure 28c, show that the quantity of CO_2 in the off-gas decreases during the treatment.

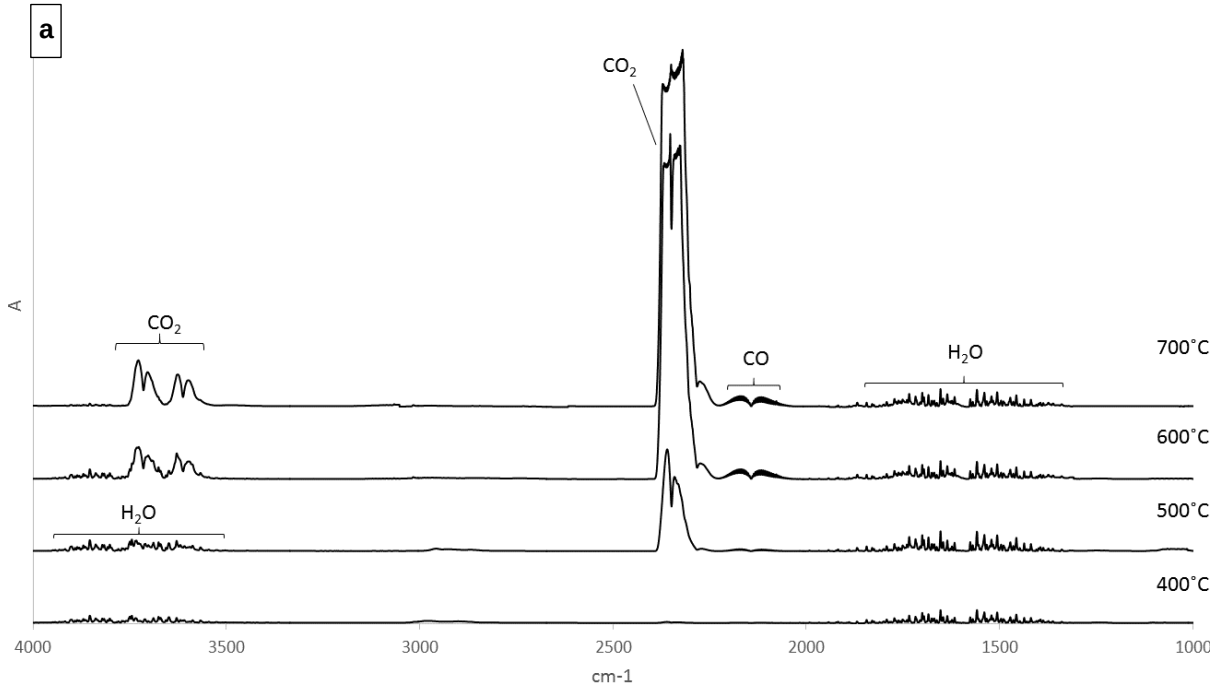

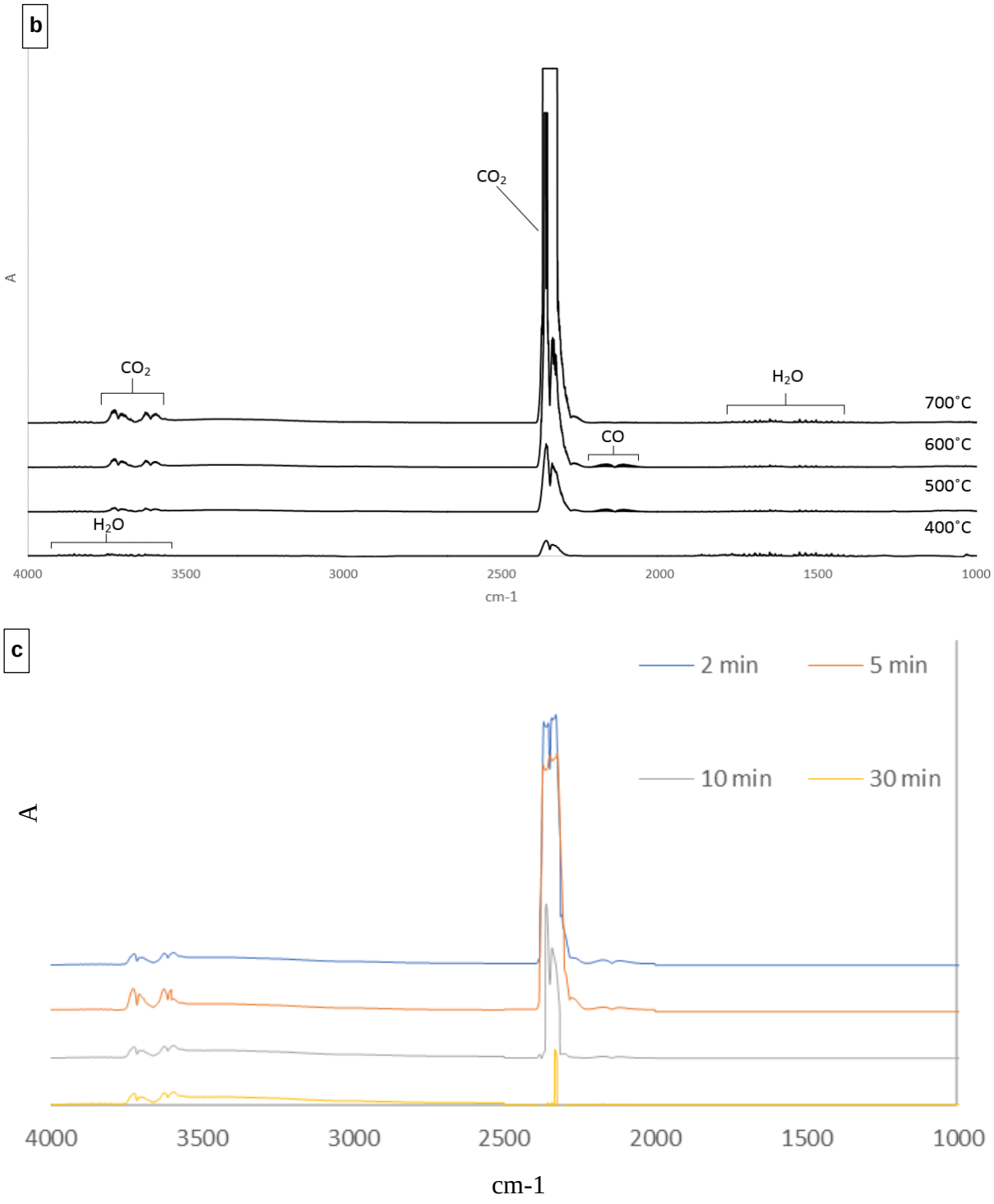

Figure 28: Comparison of absorbance spectra for samples treated for 5 minutes at 400˚, 500˚, 600˚, and 700°C. (a) for pyrolysis; (b) for incineration. (c)spectra of gas samples collected during incineration at 700°C at different times after the start of treatment.

The high temperature promotes the degradation of the PVDF, which typically occurs through a mechanism of dehydrofluorination [117].

It was expected that the presence of HF would be detected in the gas phase in the FTIR spectra. However, the signal for H_2O at high frequency probably obscures the signal for this acid. Evidence for the degradation of the binder was obtained by analyzing the gas washing water to detect the presence of fluoride ions. The analysis did not show any significant difference in the amount of gaseous fluorides created when samples were treated at different times and temperatures. After thermal treatment of the samples (0.5g), the average concentration of fluoride in the absorption solutions was 0.23±0.01 mM, and the average pH value of these solutions was 3.1± 0.3 for pyrolysis, and 0.27±0.02 mM and 2.9± 0.3 for incineration. Neither the Ion Chromatography nor FTIR performed on the absorption liquid showed any presence of volatile phosphates, which could be expected due to the decomposition of the electrolyte.

4.4.2 The organic by-product of the thermal treatment

The high temperature led to the decomposition of the organic substances present in the samples. The decomposition products were brought into the final part of the alumina tube by the constant gas flow. This part of the tube was located outside the oven and therefore was colder. In this section of the tube, the organic substances condensed, covering the internal part of the tube (see Figure 29). The condensates were collected by firstly washing the tube with acetone, followed by water and then ether.

Figure 29: The internal section of the quartz tube covered with the organic by-product.

The result is a brown-yellow tar with a density similar to oil. This oil is a mixture of many decomposition products, therefore, the identification of the exact composition was complex.
It was observed that this oil consisted of a less polar fraction (Fraction 1), and a more polar fraction (Fraction 2).

Incineration

When incinerating all anodes and cathodes contained in a single LiB cell at 650°C for 180 minutes, 2±0.15 g of oil was collected, which equates to ~0.3% of the weight of the battery. From this initial quantity it was possible to obtain ~0.8g of Fraction 1 (corresponding to ~0.1 w% of the battery) and ~1.2g of Fraction 2 (corresponding to ~0.2 w% of the battery).

A sample from each of the two collected fractions was sent to the MedAc LTD laboratory (UK) for the determination of the contents of C, H, P, and F (Table 10).

Table 10: Elemental analysis of carbon, hydrogen, phosphor, and fluorine in the oil collected after incineration at 650°C for 180 minutes, performed by MedAc LTD.

	Element (w%)			
	C	H	F	P
Fraction 1 (non-polar)	85.2±0.2	14.0±0.2	0.9±0.1	0.02±0.01
Fraction 2 (polar)	45.2±0.2	5.6±0.1	35.0±0.3	0.33±0.01

Fraction 1 is almost totally composed of C and H; dividing the percentage of C and H for their respective atomic mass, the ratio of carbon and hydrogen is 1 to 2. It can therefore be assumed that the hydrocarbons in Fraction 1 most probably consist of molecules containing chains of -CH_2- produced by the decomposition of the polypropylene separator. In Fraction 2 the amount of fluorine instead represents one-third of the total (35.0 w%). This indicates that the most polar fraction was largely composed of the decomposition products of the PVDF. Fluorine was therefore not totally removed from the system as hydrofluoric acid by the flow of gas but instead partially remained in this organic by-product. A small quantity of P, produced from the decomposition of the electrolyte, was identified in both fractions.

Based on the acquired data, it is possible to estimate the amount of F in the gas product and the residual amount of F in the oil product.

Considering that F represents 35.0 ±0.3 w% of Fraction 2 (1.2g), then 0.4g of this fraction is composed of F. This quantity of F remains in the oil by-product produced by the incineration of an entire LiB cell.

From the ion-chromatographic data, a sample (0.50±0.02 g) releases a quantity of F in gas form equal to 0.27±0.02 mM (5.1 mg) in the absorption liquid used. Considering that the samples were composed of a mix of cathodes and anodes and the total weight of these components in a battery cell is 469.3 g (cathode active material: 218.2±0.8 g, graphite: 115.9±0.3 g, copper foils:

57.0±0.1 g, aluminum foils: 36.0±0.1 g, and separators 42.2±0.5 g; chapter 5.2.1), the quantity of F released during the thermal treatment of an entire LiB cell is equal to 4.8±0.1 g.
Therefore, the quantity of F produced during incineration is equal to 5.2 g (0.4 g+4.8 g). The majority of this is released in gas form, >90 w% (4.8 g), while the rest remains in the oil by-products.

Pyrolysis

When pyrolyzing all anodes and cathodes contained in a single LiB cell at 650°C for 180 minutes, 5.0±0.2 g of oil was collected, which equates to ~0.7% of the weight of the battery. From this initial quantity it was possible to obtain ~1.2g of Fraction 1 (corresponding to ~0.2 w% of the battery) and ~3.8g of Fraction 2 (corresponding to ~0.5 w% of the battery).
The quantity of oil collected after pyrolysis was almost three times the quantity collected after incineration. In particular, the quantity of the polar fraction (Fraction 2) was increased more of three times compared to the quantity of Fraction 2 collected after incineration.
A sample from each of the two collected fractions was sent to the MedAc LTD laboratory (UK) for the determination of the contents of C, H, P, and F (Table 11).

Table 11: Elemental analysis of carbon, hydrogen, phosphor, and fluorine in the oil collected after pyrolysis at 650°C for 180 minutes, performed by MedAc LTD.

	Element (w%)			
	C	H	F	P
Fraction 1 (non-polar)	82.2±1.0	14.0±0.2	1.0±0.1	0.02±0.01
Fraction 2 (polar)	45.2±0.2	3.6±0.2	37.1±0.1	0.32±0.01

The composition of oil collected after pyrolysis is similar to the composition of the oil collected after incineration. So, also in this case the most polar fraction was largely composed of the decomposition products of the PVDF. Fluorine was therefore not totally removed from the system as hydrofluoric acid by the flow of gas but partially remained in this organic by-product. Considering that F represents 37.1 ±0.1 w% of Fraction 2 (3.8g), then 1.4g of this fraction is composed of F. This quantity of F remains in the oil by-product produced by the incineration of an entire LiB cell.
From the ion-chromatographic data, a sample (0.50±0.02 g) releases a quantity of F in gas form equal to 0.23±0.01 mM (4.4 mg) in the absorption liquid used. Considering that the samples were composed of a mix of cathodes and anodes and the total weight of these components in a

battery cell is 469.3 g (cathode active material: 218.2±0.8 g, graphite: 115.9±0.3 g, copper foils: 57.0±0.1 g, aluminum foils: 36.0±0.1 g, and separators 42.2±0.5 g; chapter 5.2.1), the quantity of F released during the thermal treatment of an entire LiB cell is equal to 4.1±0.1 g.
Therefore, during incineration, the quantity of F produced is equal to 5.5 g (1.4 g+4.1 g). The majority is released in gas form, >75 w% (4.1 g), while the rest remains in the oil by-products.

Gas chromatographic-mass spectrometer analysis of both fractions was performed to identify their composition. None of the sample fractions had a spectrum containing the three lines for ion masses 256M+, (M-47)+, and (M-56)+ which would identify the fluoro-dioxin 2,3,7,8-TFDD [109].

To confirm that none of the metals from the cathode active material were lost in the gas flow or formed organo-complexes, the oil was treated in a solution consisting of a mixture of 98% concentrated H_2SO_4 and 30% concentrated H_2O_2, as described in the Materials and Methods chapter. The dissolving solution and the gas-washing solution were analyzed by ICP-OES. This measurement did not detect any Ni, Co, Mn, Ni, Cu, or Al in those solutions.

The incineration proved to have a larger environmental impact than the dynamic pyrolysis due to its greater production of HF, CO, and CO_2. By contrast, during vacuum pyrolysis, the gases remain trapped in the furnace and the atmosphere becomes rich in CO, CO_2, hydrofluoric acid, and organic compounds that are volatile at high temperature. The latter re-condense when the furnace returns to room temperature, thus preventing them from escaping as gas from the system. This reduces the danger of the gas produced during the thermal process and therefore the costs of reducing the toxic substances contained therein. Another aspect that needs to be considered is the energy consumption. Vacuum pyrolysis has the advantage of not needing continuous pumping of gas into the system.
The PVDF decomposes during the treatment, releasing HF in a gaseous state and an organic by-product rich in fluorine. Further analysis is needed to determine which organic molecules compose this by-product and if this can have a new application.

4.4.3 Formation of HF in the case of a high temperature accident involving the NMC-LiB using a cooling system based on the refrigeration liquids (RL) containing halogens. (Paper IV)

The concentration of F in the refrigeration liquids as determined through a Combustion Ion Chromatographic analysis is shown in Table 12.

Table 12: The concentration of fluoride in the refrigeration liquids.

	[F] (mol/L)
RL1	28.4±0.2
RL2	18.4±0.1
RL3	13.7±0.2
RL4	1.0±0.1

Dense white smoke was produced after 2 minutes from the beginning of the incineration for the sample without RL and after 5 minutes with RL. The amount of smoke slowly decreased but persisted until 30 minutes from the beginning of the heat treatment. At the end of the experiments, all the RLs were decomposed to gas products, without leaving any condensed product. The data in Figure 30 and Table 13 show the amounts of HF released during the experiments. The use of RL1 contributes to the HF formation by a ratio of 5:1 ($[F]_{RL}/[F]_{LiB}$) when the weight ratio is 1:7 (w_{RL}/w_{LiB}) and produces the highest quantity of HF.

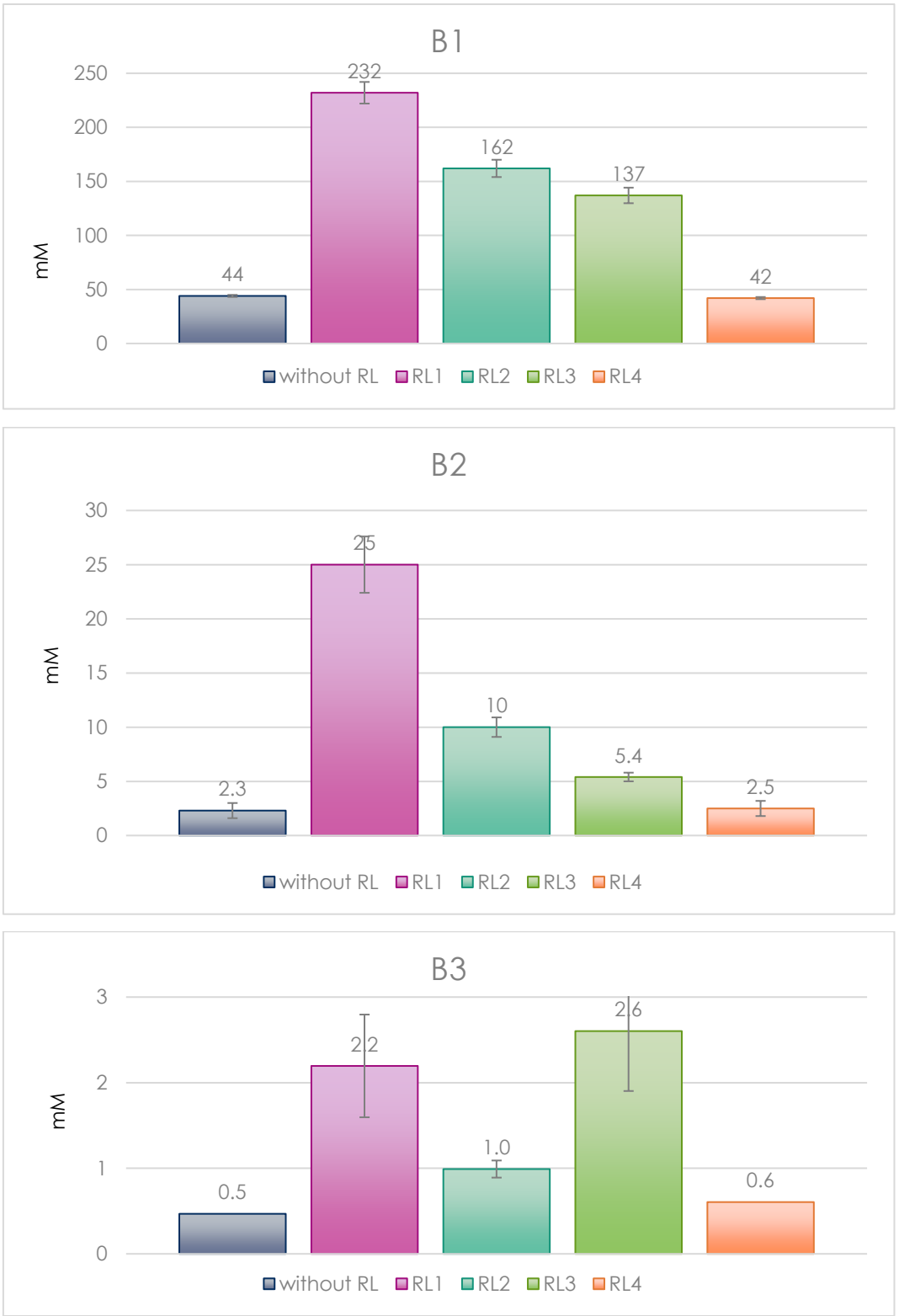

Figure 30: Ion chromatographic analysis data of the gas product (HF). B1 is the solution from the first washing bottle, B2 is the solution from the second washing bottle and B3 is the solution from the last washing bottle in the system.

Table 13: Ion chromatographic analysis of the HF in the off-gas

	[F] (mmol/L)			
	B1	B2	B3	Tot
without RL	44±1.0	2.3±0.7	0.5±0.0	46.8±1.7
RL1	232±10	25±2.6	2.2±0.6	259±13
RL2	162±8.0	10±0.9	1.0±0.1	173±9.0
RL3	137±7.2	5.4±0.4	2.6±0.7	145±8.3
RL4	42±1.0	2.5±0.7	0.6±0.0	45±1.7

For the RL1, RL2, and RL3 only ~1% of the initial concentration of F in the RL (Table 12) was detected by ion chromatographic analysis of the gas-washing water (Table 13). This indicates that only a small quantity of the fluoride is released as HF during the decomposition of the RLs. There is not a significant difference between the total concertation of F released thermal treating the LiB without refrigeration liquids and the concertation of F released using RL4. So RL4 did not contribute significantly to any HF formation, whereas RL1-3 increased the HF formation

The pH of the Milli Q water used to wash the off-gas varied depending on which RL was used (Table 14). This indicates the presence of hydrogen ions, most probably from HF. The pH increased from B1 to B3 for RL1, RL2, and RL3, corresponding to a decrease in F concentration in the washing solutions as shown in Table 13.

The pH measured for RL4 and for the LiB thermal treated without refrigeration liquids has similar values in B1. In B2 and B3, RL 4 has a higher pH than LiB without RL. Since RL4 contains a negligible amount of F this decrease is explained by the formation of another substance than HF.

Table 14: Measured pH of the washing solution in the 3 gas-washing bottles, where the accuracy of the analysis was ±0.2 (absolute values). The pH meter was calibrated with three standard solutions at pH 1, 4, and 7.

	pH		
	B1	B2	B3
without RL	2.1	3.0	3.0
RL1	1.3	2.4	2.7
RL2	1.9	2.4	2.7
RL3	1.9	2.5	2.6
RL4	2.1	3.4	3.8

The use of an RL with a fluorine-based chemical composition leads to a consistent increase in the quantity of HF released in the event of a high temperature accident. However, the F released as HF represents a small quantity of the [F] present in the RL before the treatment. The decomposition of the RL, therefore, produces a variety of other by-products that need to be identified.

5. Conclusions

The effects of incineration, dynamic pyrolysis, and vacuum pyrolysis on the composition of NMC-LiB were studied. It has been defined how the thermal treatment utilizes the carbon already present in the NMC battery. It was demonstrated how this carbon triggers a carbothermic reduction of the metal oxides of the cathode active material. In addition, due to their hazardous potential, the behavior of the organic components was also followed and determined.

In inert or vacuum conditions Co, Ni, and Mn in the cathode materials are carbothermically reduced to a lower oxidation state. Co, CoO, Ni, NiO, Mn, and Mn_3O_4 are the main products. Li stays in the oxidation state +1 and forms Li_2O and Li_2CO_3. The lithium-metal-oxides are completely decomposed. Instead, during incineration, partial oxidation of the products from the decomposition of the lithium-metal-oxide was observed. Co, CoO, Co_3O_4, Ni, NiO, Mn_3O_4, and MnO_2 were formed. Li stayed in the oxidation state +1 and formed Li_2O and Li_2CO_3. The O_2 in the gas flow caused partial oxidation of the Cu and Al foils, with the formation of CuO and Al_2O_3.

An increase in temperature and duration of treatment promoted the carbothermic reduction and the removal of graphite and organic components. The carbon content reached ~15 w% after dynamic pyrolysis, starting from an initial 41w%. Almost complete decomposition of the graphite and organic species, ~0.6 w% was reached after incineration.

No differences were observed between the effects that the carbothermic reduction had on scrap LiB materials and spent LiBs materials and only the vacuum pyrolysis had relevant effects on the morphology of cathode active materials.

Thermal treatment followed by milling permits the separation of the cathode active material from the Al metal foils. This is due to the decomposition of the PVDF binder at high temperature. The best result was >95% of active material removed. However, increasing the temperature and time of treatment also resulted in an increase in the contamination with Al powder in the separated cathode active material, which decreased the metal yield in the Al

recycling process and thus decreases the possibilities for direct utilization of cathode material for battery production.

The organic components decomposed, releasing a gas composed mainly of CO_2, CO, and H_2O. The PVDF decomposed to release HF and an organic by-product rich in fluorine. The results show the presence of fluoride-containing compounds in both the gas phase and oil organic by-products.

In the case of a high temperature accident, the use of a refrigeration liquid with a fluorine-based chemical composition leads to a consistent increase in the quantity of HF released in the event of a high temperature accident. However, the F released as HF represents only a small quantity of the [F] present in the RL1-3 before the treatment. The decomposition of the RL1-3, therefore, produces a variety of other by-products that need to be identified. With a refrigeration liquid, the smoke formation was delayed 2-2.5 times as compared without using RL (using passive air cooling).

The methods that we applied can be applied flexibly on batteries of different chemistry. Pyrolysis and incineration are already used as thermal pretreatment in some industrial recycling processes. The results achieved in the present work contribute to a better understanding of the effect of carbothermal treatments on the complex chemical system in real battery waste processing and can be applied to optimize the industrial processing procedures to reach higher efficiencies in the transformation of complex oxides and to decrease the treatment time, and also the energy demands for the processing.

6. Recommendations for future work

- Further analysis is needed to define the exact organic molecules and the chemical composition of the oil by-product. Tests are needed to identify the performance and possible application of the oil produced during the thermal treatment.

- It has been observed that during pyrolysis all the cathode active material reacting with the C can be reduced. On the contrary, more than 50% of the graphite, which is initially present in the samples, is not consumed during the heat treatment. There is therefore a possibility to combine this process with the recycling processes of other waste material that needs a carbothermic treatment.

7. Acknowledgments

This thesis has been carried out at Chalmers University of Technology, Department of Chemistry and Chemical Engineering, Nuclear Chemistry and Industrial Materials Recycling.

An acknowledgment goes to the Swedish Energy Agency – Battery Fund (Grant No: 40506-1 and 48204-1) for providing the funding of the research related to the battery waste treatment.

The authors would like to acknowledge the support of Volvo Cars Corporation for providing the samples and valuable discussion.

Research related to production scrap was supported by KIC InnoEnergy – (Grant 8_2018_lP167_ReVolt Re-valorisation of active metals for Li-ion battery production).

The authors would like to acknowledge the support of Northvolt AB, in providing the samples and valuable discussion.

An acknowledgment goes to the Swedish Energy Agency (Grant no. 2018-008060) for providing the funding of the research related to the cooling liquids treatment.
The authors would like to acknowledge the support of APR Technologies AB, in providing the samples and valuable discussion.

The authors also thank the Department of Modeling and Simulation at Outotec for help with extending the database data for the thermodynamic calculations.

A great deal of thanks is extended to:

Martina Petranikova for her patience, knowledge and invaluable help. In these years she has been always present for me as a guide with kindness and willingness.

Britt-Marie Steenari for her guidance, knowledge and the important suggestions that she has given me to make better my method of work and writing.

My examiner Christian Ekberg for his kind assistance and valuable advices .

Burcak Ebin for his help with experiments and his willingness to answers my incredible amount of questions. Your help has been essential in these years.

Mark R.StJ. Foreman for his essential help in the analysis of the organic by-products.

Stellan Holgersson for his invaluable help with the laboratory equipment.

Marcus Hedberg for his essential help with the carbon content analysis.

The rest of the people at NC/IMR. I feel lucky to work with and next to so incredible and talented people. A special thank to Marino Gregoric and Fredrik Espegren to have been my first friends in Sweden and always helped me with kindness and patience. To Luis Guillermo Gonzalez Fonseca and Emma López-Alonso County for their friendship and for the incredible adventures by car and in the board games. To Niklas Hansson, Anna-Elina Pasi and Thea Lyseid Authen to be not only colleagues but also great friends. To Cristian Tunsu, Toni Karlsson, Mikael Karlsson, Jinfeng Tang, Filip Holmberg, Artem Matyskin, Mikhail S Tyumentsev, Lovisa Bauhn, and Jenny Halleröd to have been fantastic colleagues.

My family and friends for their support and to always be present for me despite the distance. A special thank to my parents, my grandparents, Alice's parents, and my brother Marco for their love. To Giorgio and Marta for really good times and unforgettable memories.

Alberto and Luca to be more brothers than friends.

Angela,Olha,Paola, Alessandra, Yordan, Maurizio, and Emanuele to be irreplaceable friends.

My girlfriend Alice for her love and support. You are the most interesting, shining and beautiful person that I have ever met.

8. References

(1) Chagnes, A. *Lithium Battery Technologies*; Elsevier Inc., 2015. https://doi.org/10.1016/b978-0-12-801417-2.00005-0.

(2) Zheng, X.; Zhu, Z.; Lin, X.; Zhang, Y.; He, Y.; Cao, H.; Sun, Z. A Mini-Review on Metal Recycling from Spent Lithium Ion Batteries. *Engineering*. Elsevier Ltd June 1, 2018, pp 361–370. https://doi.org/10.1016/j.eng.2018.05.018.

(3) Guo, Y.; Li, F.; Zhu, H.; Li, G.; Huang, J.; He, W. Leaching Lithium from the Anode Electrode Materials of Spent Lithium-Ion Batteries by Hydrochloric Acid (HCl). *Waste Manag.* **2016**, *51*, 227–233. https://doi.org/10.1016/j.wasman.2015.11.036.

(4) Global EV Outlook 2020. *Glob. EV Outlook 2020* **2020**. https://doi.org/10.1787/d394399e-en.

(5) Zeng, X.; Li, J.; Singh, N. Recycling of Spent Lithium-Ion Battery: A Critical Review. *Crit. Rev. Environ. Sci. Technol.* **2014**, *44* (10), 1129–1165. https://doi.org/10.1080/10643389.2013.763578.

(6) International Energy Agency. *Global EV Outlook 2018: Towards Cross-Modal Electrification*; 2018. https://doi.org/10.1787/9789264302365-en.

(7) Till Bunsen; Cazzola, P.; D'Amore, L.; Gorner, M.; Scheffer, S.; Schuitmaker, R.; Signollet, H.; Tattini, J.; Paoli, J. T. L. Global EV Outlook 2019 to Electric Mobility. *OECD iea.org* **2019**, 232.

(8) Liobikienė, G.; Butkus, M. The European Union Possibilities to Achieve Targets of Europe 2020 and Paris Agreement Climate Policy. *Renew. Energy* **2017**, *106* (2017), 298–309. https://doi.org/10.1016/j.renene.2017.01.036.

(9) Wollenberg, E.; Richards, M.; Smith, P.; Havlík, P.; Obersteiner, M.; Tubiello, F. N.; Herold, M.; Gerber, P.; Carter, S.; Reisinger, A.; et al. Reducing Emissions from Agriculture to Meet the 2 °C Target. *Glob. Chang. Biol.* **2016**, *22* (12), 3859–3864. https://doi.org/10.1111/gcb.13340.

(10) Talens Peiró, L.; Villalba Méndez, G.; Ayres, R. U. Lithium: Sources, Production, Uses, and Recovery Outlook. *Jom* **2013**, *65* (8), 986–996. https://doi.org/10.1007/s11837-013-

0666-4.

(11) Sun, Y.; Goh, B. China wants new energy vehicle sales in 2025 to be 25% of all car sales https://www.reuters.com/article/us-china-autos-electric/china-wants-new-energy-vehicle-sales-in-2025-to-be-25-of-all-car-sales-idUSKBN1Y70BN.

(12) Warner, J. The Future of Lithium-Ion Batteries and Electrification. *Handb. Lithium-Ion Batter. Pack Des.* **2015**, 211–216. https://doi.org/10.1016/B978-0-12-801456-1.00016-6.

(13) Olivetti, E. A.; Ceder, G.; Gaustad, G. G.; Fu, X. Lithium-Ion Battery Supply Chain Considerations: Analysis of Potential Bottlenecks in Critical Metals. *Joule* **2017**, *1* (2), 229–243. https://doi.org/10.1016/j.joule.2017.08.019.

(14) Xu, B.; Qian, D.; Wang, Z.; Meng, Y. S. Recent Progress in Cathode Materials Research for Advanced Lithium Ion Batteries. *Mater. Sci. Eng. R Reports* **2012**, *73* (5–6), 51–65. https://doi.org/10.1016/j.mser.2012.05.003.

(15) Wikner, E. THESIS FOR THE DEGREE OF LICENTIATE OF ENGINEERING Lithium Ion Battery Aging: Battery Lifetime Testing and Physics-Based Modeling for Electric Vehicle Applications. **2017**, 94.

(16) Belchí Lorente, D.; Mandil, G.; Svecova, L.; Thivel, P.-X.; Zwolinski, P. *Life Cycle and Sustainability*; Elsevier Inc., 2015. https://doi.org/10.1016/b978-0-12-801417-2.00008-6.

(17) Schmuch, R.; Wagner, R.; Hörpel, G.; Placke, T.; Winter, M. Performance and Cost of Materials for Lithium-Based Rechargeable Automotive Batteries. *Nat. Energy* **2018**, *3* (4), 267–278. https://doi.org/10.1038/s41560-018-0107-2.

(18) Petranikova, M.; Ebin, B.; Mikhailova, S.; Steenari, B. M.; Ekberg, C. Investigation of the Effects of Thermal Treatment on the Leachability of Zn and Mn from Discarded Alkaline and Zn–C Batteries. *J. Clean. Prod.* **2018**, *170*, 1195–1205. https://doi.org/10.1016/j.jclepro.2017.09.238.

(19) Winslow, K. M.; Laux, S. J.; Townsend, T. G. A Review on the Growing Concern and Potential Management Strategies of Waste Lithium-Ion Batteries. *Resources, Conservation and Recycling*. Elsevier B.V. February 1, 2018, pp 263–277.

https://doi.org/10.1016/j.resconrec.2017.11.001.

(20) Georgi-Maschler, T.; Friedrich, B.; Weyhe, R.; Heegn, H.; Rutz, M. Development of a Recycling Process for Li-Ion Batteries. *J. Power Sources* **2012**, *207*, 173–182. https://doi.org/10.1016/j.jpowsour.2012.01.152.

(21) Gaines, L. The Future of Automotive Lithium-Ion Battery Recycling: Charting a Sustainable Course. *Sustain. Mater. Technol.* **2014**, *1–2*, 2–7. https://doi.org/10.1016/j.susmat.2014.10.001.

(22) Zhang, W.; Xu, C.; He, W.; Li, G.; Huang, J. A Review on Management of Spent Lithium Ion Batteries and Strategy for Resource Recycling of All Components from Them. *Waste Manag. Res.* **2018**, *36* (2), 99–112. https://doi.org/10.1177/0734242X17744655.

(23) Guan, J.; Li, Y.; Guo, Y.; Su, R.; Gao, G.; Song, H.; Yuan, H.; Liang, B.; Guo, Z. Mechanochemical Process Enhanced Cobalt and Lithium Recycling from Wasted Lithium-Ion Batteries. *ACS Sustain. Chem. Eng.* **2017**, *5* (1), 1026–1032. https://doi.org/10.1021/acssuschemeng.6b02337.

(24) Knyazev, A. V.; Mączka, M.; Smirnova, N. N.; Knyazeva, S. S.; Chernorukov, N. G.; Ptak, M.; Shushunov, A. N. Study of the Phase Transition and Thermodynamic Functions of LiMn2O4. *Thermochim. Acta* **2014**, *593*, 58–64. https://doi.org/10.1016/j.tca.2014.08.020.

(25) Li, M.; Lu, J.; Chen, Z.; Amine, K. 30 Years of Lithium-Ion Batteries. *Advanced Materials*. Wiley-VCH Verlag August 16, 2018. https://doi.org/10.1002/adma.201800561.

(26) Mizushima, K.; Jones, P. C.; Wiseman, P. J.; Goodenough, J. B. LixCoO2 (0<x≤1): A New Cathode Material for Batteries of High Energy Density. *Solid State Ionics* **1981**, *3–4* (C), 171–174. https://doi.org/10.1016/0167-2738(81)90077-1.

(27) Lv, W.; Wang, Z.; Cao, H.; Sun, Y.; Zhang, Y.; Sun, Z. A Critical Review and Analysis on the Recycling of Spent Lithium-Ion Batteries. *ACS Sustain. Chem. Eng.* **2018**, *6* (2), 1504–1521. https://doi.org/10.1021/acssuschemeng.7b03811.

(28) Xu, J.; Thomas, H. R.; Francis, R. W.; Lum, K. R.; Wang, J.; Liang, B. A Review of Processes and Technologies for the Recycling of Lithium-Ion Secondary Batteries.

Journal of Power Sources. March 1, 2008, pp 512–527. https://doi.org/10.1016/j.jpowsour.2007.11.074.

(29) Li, Z.; Huang, J.; Yann Liaw, B.; Metzler, V.; Zhang, J. A Review of Lithium Deposition in Lithium-Ion and Lithium Metal Secondary Batteries. *J. Power Sources* **2014**, *254*, 168–182. https://doi.org/10.1016/j.jpowsour.2013.12.099.

(30) Kwade, A.; Haselrieder, W.; Leithoff, R.; Modlinger, A.; Dietrich, F.; Droeder, K. Current Status and Challenges for Automotive Battery Production Technologies. *Nat. Energy* **2018**, *3* (4), 290–300. https://doi.org/10.1038/s41560-018-0130-3.

(31) A Method for Recycling Spent Lithium Metal Polymer Rechargeable Batteries and Related Materials. 2001.

(32) Liu, C.; Lin, J.; Cao, H.; Zhang, Y.; Sun, Z. Recycling of Spent Lithium-Ion Batteries in View of Lithium Recovery: A Critical Review. *Journal of Cleaner Production*. 2019. https://doi.org/10.1016/j.jclepro.2019.04.304.

(33) Träger, T.; Friedrich, B.; Weyhe, R. Recovery Concept of Value Metals from Automotive Lithium-Ion Batteries. *Chemie-Ingenieur-Technik* **2015**, *87* (11), 1550–1557. https://doi.org/10.1002/cite.201500066.

(34) Chen, M.; Ma, X.; Chen, B.; Arsenault, R.; Karlson, P.; Simon, N.; Wang, Y. Recycling End-of-Life Electric Vehicle Lithium-Ion Batteries. *Joule* **2019**, *3* (11), 2622–2646. https://doi.org/10.1016/j.joule.2019.09.014.

(35) Ekberg, C.; Petranikova, M. Lithium Batteries Recycling. In *Lithium Process Chemistry*; Elsevier, 2015; pp 233–267. https://doi.org/10.1016/B978-0-12-801417-2.00007-4.

(36) Bernardes, A. M.; Espinosa, D. C. R.; Tenório, J. A. S. Recycling of Batteries: A Review of Current Processes and Technologies. *J. Power Sources* **2004**, *130* (1–2), 291–298. https://doi.org/10.1016/j.jpowsour.2003.12.026.

(37) Hanisch, C.; Diekmann, J.; Stieger, A.; Haselrieder, W.; Kwade, A. Recycling of Lithium-Ion Batteries. *Handb. Clean Energy Syst.* **2015**, No. 2011, 1–24. https://doi.org/10.1002/9781118991978.hces221.

(38) Velázquez-Martínez, O.; Valio, J.; Santasalo-Aarnio, A.; Reuter, M.; Serna-Guerrero, R. A Critical Review of Lithium-Ion Battery Recycling Processes from a Circular Economy

Perspective. *Batteries* **2019**, *5* (4), 5–7. https://doi.org/10.3390/batteries5040068.

(39) Blomgren, G. E. The Development and Future of Lithium Ion Batteries. *J. Electrochem. Soc.* **2017**, *164* (1), A5019–A5025. https://doi.org/10.1149/2.0251701jes.

(40) Ekberg, C.; Petranikova, M. *Lithium Batteries Recycling*; Elsevier Inc., 2015. https://doi.org/10.1016/B978-0-12-801417-2.00007-4.

(41) Christmann, P.; Gloaguen, E.; Labbé, J.-F.; Melleton, J.; Piantone, P. *Global Lithium Resources and Sustainability Issues*; 2015. https://doi.org/10.1016/B978-0-12-801417-2.00001-3.

(42) Elwert, T.; Goldmann, D.; Römer, F.; Buchert, M.; Merz, C.; Schueler, D.; Sutter, J. Current Developments and Challenges in the Recycling of Key Components of (Hybrid) Electric Vehicles. *Recycling* **2016**, *1* (1), 25–60. https://doi.org/10.3390/recycling1010025.

(43) Warner, J. Second Life and Recycling of Lithium-Ion Batteries. *Handb. Lithium-Ion Batter. Pack Des.* **2015**, 169–176. https://doi.org/10.1016/b978-0-12-801456-1.00014-2.

(44) Meshram, P.; Pandey, B. D.; Mankhand, T. R. Extraction of Lithium from Primary and Secondary Sources by Pre-Treatment, Leaching and Separation: A Comprehensive Review. *Hydrometallurgy*. Elsevier 2014, pp 192–208. https://doi.org/10.1016/j.hydromet.2014.10.012.

(45) Petrániková, M.; Miškufová, A.; Havlík, T.; Forsén, O.; Pehkonen, A. *Cobalt Recovery from Spent Portable Lithium Accumulators after Thermal Treatment*; 2011; Vol. 17.

(46) Li, Z.; Huang, J.; Yann Liaw, B.; Metzler, V.; Zhang, J. A Review of Lithium Deposition in Lithium-Ion and Lithium Metal Secondary Batteries. *J. Power Sources* **2014**, *254*, 168–182. https://doi.org/10.1016/j.jpowsour.2013.12.099.

(47) Chagnes, A.; Pospiech, B. A Brief Review on Hydrometallurgical Technologies for Recycling Spent Lithium-Ion Batteries. *Journal of Chemical Technology and Biotechnology*. July 2013, pp 1191–1199. https://doi.org/10.1002/jctb.4053.

(48) Chagnes, A. *Fundamentals in Electrochemistry and Hydrometallurgy*; 2015. https://doi.org/10.1016/b978-0-12-801417-2.00002-5.

(49) Mantuano, D. P.; Dorella, G.; Elias, R. C. A.; Mansur, M. B. Analysis of a Hydrometallurgical Route to Recover Base Metals from Spent Rechargeable Batteries by Liquid-Liquid Extraction with Cyanex 272. *J. Power Sources* **2006**, *159* (2), 1510–1518. https://doi.org/10.1016/j.jpowsour.2005.12.056.

(50) Yao, Y.; Zhu, M.; Zhao, Z.; Tong, B.; Fan, Y.; Hua, Z. Hydrometallurgical Processes for Recycling Spent Lithium-Ion Batteries: A Critical Review. *ACS Sustainable Chemistry and Engineering*. American Chemical Society November 5, 2018, pp 13611–13627. https://doi.org/10.1021/acssuschemeng.8b03545.

(51) Lain, M. J. Recycling of Lithium Ion Cells and Batteries. *J. Power Sources* **2001**, *97–98* (June 2000), 736–738. https://doi.org/10.1016/S0378-7753(01)00600-0.

(52) Harper, G.; Sommerville, R.; Kendrick, E.; Driscoll, L.; Slater, P.; Stolkin, R.; Walton, A.; Christensen, P.; Heidrich, O.; Lambert, S.; et al. Recycling Lithium-Ion Batteries from Electric Vehicles. *Nature* **2019**, *575* (7781), 75–86. https://doi.org/10.1038/s41586-019-1682-5.

(53) Zhang, X.; Li, L.; Fan, E.; Xue, Q.; Bian, Y.; Wu, F.; Chen, R. Toward Sustainable and Systematic Recycling of Spent Rechargeable Batteries. *Chemical Society Reviews*. Royal Society of Chemistry October 7, 2018, pp 7239–7302. https://doi.org/10.1039/c8cs00297e.

(54) Granata, G.; Moscardini, E.; Pagnanelli, F.; Trabucco, F.; Toro, L. Product Recovery from Li-Ion Battery Wastes Coming from an Industrial Pre-Treatment Plant: Lab Scale Tests and Process Simulations. *J. Power Sources* **2012**, *206*, 393–401. https://doi.org/10.1016/j.jpowsour.2012.01.115.

(55) Liu, P.; Xiao, L.; Chen, Y.; Tang, Y.; Wu, J.; Chen, H. Recovering Valuable Metals from LiNixCoyMn1-x-YO2 Cathode Materials of Spent Lithium Ion Batteries via a Combination of Reduction Roasting and Stepwise Leaching. *J. Alloys Compd.* **2019**, *783*, 743–752. https://doi.org/10.1016/j.jallcom.2018.12.226.

(56) Zheng, X.; Gao, W.; Zhang, X.; He, M.; Lin, X.; Cao, H.; Zhang, Y.; Sun, Z. Spent Lithium-Ion Battery Recycling – Reductive Ammonia Leaching of Metals from Cathode Scrap by Sodium Sulphite. *Waste Manag.* **2017**, *60*, 680–688. https://doi.org/10.1016/j.wasman.2016.12.007.

(57) Huang, Y.; Han, G.; Liu, J.; Chai, W.; Wang, W.; Yang, S.; Su, S. A Stepwise Recovery of Metals from Hybrid Cathodes of Spent Li-Ion Batteries with Leaching-Flotation-Precipitation Process. *J. Power Sources* **2016**, *325*, 555–564. https://doi.org/10.1016/j.jpowsour.2016.06.072.

(58) Zhu, S. G.; He, W. Z.; Li, G. M.; Zhou, X.; Zhang, X. J.; Huang, J. W. Recovery of Co and Li from Spent Lithium-Ion Batteries by Combination Method of Acid Leaching and Chemical Precipitation. *Trans. Nonferrous Met. Soc. China (English Ed.* **2012**, *22* (9), 2274–2281. https://doi.org/10.1016/S1003-6326(11)61460-X.

(59) Lv, W.; Wang, Z.; Cao, H.; Sun, Y.; Zhang, Y.; Sun, Z. A Critical Review and Analysis on the Recycling of Spent Lithium-Ion Batteries. *ACS Sustain. Chem. Eng.* **2018**, *6* (2), 1504–1521. https://doi.org/10.1021/acssuschemeng.7b03811.

(60) Moradi, B.; Botte, G. G. Recycling of Graphite Anodes for the next Generation of Lithium Ion Batteries. *J. Appl. Electrochem.* **2016**, *46* (2), 123–148. https://doi.org/10.1007/s10800-015-0914-0.

(61) He, L. P.; Sun, S. Y.; Mu, Y. Y.; Song, X. F.; Yu, J. G. Recovery of Lithium, Nickel, Cobalt, and Manganese from Spent Lithium-Ion Batteries Using l -Tartaric Acid as a Leachant. *ACS Sustain. Chem. Eng.* **2017**, *5* (1), 714–721. https://doi.org/10.1021/acssuschemeng.6b02056.

(62) Zhong, X.; Liu, W.; Han, J.; Jiao, F.; Qin, W.; Liu, T. Pretreatment for the Recovery of Spent Lithium Ion Batteries: Theoretical and Practical Aspects. *J. Clean. Prod.* **2020**, *263*, 121439. https://doi.org/10.1016/j.jclepro.2020.121439.

(63) Lombardo, G.; Ebin, B.; Mark, M. R.; Steenari, B. M.; Petranikova, M. Incineration of EV Lithium-Ion Batteries as a Pretreatment for Recycling – Determination of the Potential Formation of Hazardous by-Products and Effects on Metal Compounds. *J. Hazard. Mater.* **2020**, *393* (November 2019), 122372. https://doi.org/10.1016/j.jhazmat.2020.122372.

(64) Li, J.; Wang, G.; Xu, Z. Environmentally-Friendly Oxygen-Free Roasting/Wet Magnetic Separation Technology for in Situ Recycling Cobalt, Lithium Carbonate and Graphite from Spent LiCoO 2 /Graphite Lithium Batteries. *J. Hazard. Mater.* **2016**, *302*, 97–104. https://doi.org/10.1016/j.jhazmat.2015.09.050.

(65) Bergmann, C. P.; Veit, H. M.; Moura, A.; Editors, B. *Topics in Mining, Metallurgy and Materials Engineering Series Editor: Electronic Waste Recycling Techniques*.

(66) Xu, J.; Thomas, H. R.; Francis, R. W.; Lum, K. R.; Wang, J.; Liang, B. A Review of Processes and Technologies for the Recycling of Lithium-Ion Secondary Batteries. *Journal of Power Sources*. 2008. https://doi.org/10.1016/j.jpowsour.2007.11.074.

(67) Definition, P. *Electronic Waste 电子垃圾.*

(68) Zhang, J.; Li, X.; Song, D.; Miao, Y.; Song, J.; Zhang, L. Effective Regeneration of Anode Material Recycled from Scrapped Li-Ion Batteries. *J. Power Sources* **2018**, *390* (January), 38–44. https://doi.org/10.1016/j.jpowsour.2018.04.039.

(69) Hayner, C. M.; Zhao, X.; Kung, H. H. Materials for Rechargeable Lithium-Ion Batteries. *Annu. Rev. Chem. Biomol. Eng.* **2012**, *3*, 445–471. https://doi.org/10.1146/annurev-chembioeng-062011-081024.

(70) Gu, F.; Guo, J.; Yao, X.; Summers, P. A.; Widijatmoko, S. D.; Hall, P. An Investigation of the Current Status of Recycling Spent Lithium-Ion Batteries from Consumer Electronics in China. *J. Clean. Prod.* **2017**, *161*, 765–780. https://doi.org/10.1016/j.jclepro.2017.05.181.

(71) Li, L.; Ge, J.; Wu, F.; Chen, R.; Chen, S.; Wu, B. Recovery of Cobalt and Lithium from Spent Lithium Ion Batteries Using Organic Citric Acid as Leachant. *J. Hazard. Mater.* **2010**, *176* (1–3), 288–293. https://doi.org/10.1016/j.jhazmat.2009.11.026.

(72) Inderherbergh, J. Polyvinylidene Fluoride (PVDF) Appearance, General Properties and Processing. *Ferroelectrics* **1991**, *115* (4), 295–302. https://doi.org/10.1080/00150193.1991.11876614.

(73) Vezzini, A. Manufacturers, Materials and Recycling Technologies. In *Lithium-Ion Batteries: Advances and Applications*; Elsevier B.V., 2014; pp 529–551. https://doi.org/10.1016/B978-0-444-59513-3.00023-6.

(74) Hanisch, C.; Loellhoeffel, T.; Diekmann, J.; Markley, K. J.; Haselrieder, W.; Kwade, A. Recycling of Lithium-Ion Batteries: A Novel Method to Separate Coating and Foil of Electrodes. *J. Clean. Prod.* **2015**, *108*, 301–311. https://doi.org/10.1016/j.jclepro.2015.08.026.

(75) Diekmann, J.; Hanisch, C.; Froböse, L.; Schälicke, G.; Loellhoeffel, T.; Fölster, A.-S.; Kwade, A. Ecological Recycling of Lithium-Ion Batteries from Electric Vehicles with Focus on Mechanical Processes. *J. Electrochem. Soc.* **2017**, *164* (1), A6184–A6191. https://doi.org/10.1149/2.0271701jes.

(76) Diaz, F.; Wang, Y.; Weyhe, R.; Friedrich, B. Gas Generation Measurement and Evaluation during Mechanical Processing and Thermal Treatment of Spent Li-Ion Batteries. *Waste Manag.* **2019**, *84*, 102–111. https://doi.org/10.1016/j.wasman.2018.11.029.

(77) Jung, W. Thermal Management. *Data Convers. Handb.* **2005**, 823–832. https://doi.org/10.1016/B978-075067841-4/50045-2.

(78) Rao, Z.; Wang, S. A Review of Power Battery Thermal Energy Management. *Renewable and Sustainable Energy Reviews*. December 2011, pp 4554–4571. https://doi.org/10.1016/j.rser.2011.07.096.

(79) Bandhauer, T. M.; Garimella, S.; Fuller, T. F. Temperature-Dependent Electrochemical Heat Generation in a Commercial Lithium-Ion Battery. *J. Power Sources* **2014**, *247*, 618–628. https://doi.org/10.1016/j.jpowsour.2013.08.015.

(80) Kim, J.; Oh, J.; Lee, H. Review on Battery Thermal Management System for Electric Vehicles. *Appl. Therm. Eng.* **2019**, *149* (November 2018), 192–212. https://doi.org/10.1016/j.applthermaleng.2018.12.020.

(81) Abiotic, S.; Air, S. A.; Active, S.; Basic, S.; Energy, A.; Cyanex, S.; Battery, S.; Compound, S.; Acidic, S.; Carbon, S.; et al. Lithium Process Chemistry. *Lithium Process Chem.* **2015**, 293–300. https://doi.org/10.1016/B978-0-12-801417-2.18001-6.

(82) Nazari, A.; Farhad, S. Heat Generation in Lithium-Ion Batteries with Different Nominal Capacities and Chemistries. *Appl. Therm. Eng.* **2017**, *125*, 1501–1517. https://doi.org/10.1016/j.applthermaleng.2017.07.126.

(83) Saw, L. H.; Ye, Y.; Tay, A. A. O. Electrochemical-Thermal Analysis of 18650 Lithium Iron Phosphate Cell. *Energy Convers. Manag.* **2013**, *75*, 162–174. https://doi.org/10.1016/j.enconman.2013.05.040.

(84) Song, D.; Wang, X.; Zhou, E.; Hou, P.; Guo, F.; Zhang, L. Recovery and Heat Treatment

of the Li(Ni1/3Co 1/3Mn1/3)O2 Cathode Scrap Material for Lithium Ion Battery. *J. Power Sources* **2013**, *232*, 348–352. https://doi.org/10.1016/j.jpowsour.2012.10.072.

(85) Yang, L.; Xi, G.; Xi, Y. Recovery of Co, Mn, Ni, and Li from Spent Lithium Ion Batteries for the Preparation of LiNixCoyMnzO2 Cathode Materials. *Ceram. Int.* **2015**, *41* (9), 11498–11503. https://doi.org/10.1016/j.ceramint.2015.05.115.

(86) Paulino, J. F.; Busnardo, N. G.; Afonso, J. C. Recovery of Valuable Elements from Spent Li-Batteries. *J. Hazard. Mater.* **2008**, *150* (3), 843–849. https://doi.org/10.1016/j.jhazmat.2007.10.048.

(87) Hu, J.; Zhang, J.; Li, H.; Chen, Y.; Wang, C. A Promising Approach for the Recovery of High Value-Added Metals from Spent Lithium-Ion Batteries. *J. Power Sources* **2017**, *351*, 192–199. https://doi.org/10.1016/j.jpowsour.2017.03.093.

(88) Liu, C.; Lin, J.; Cao, H.; Zhang, Y.; Sun, Z. Recycling of Spent Lithium-Ion Batteries in View of Lithium Recovery: A Critical Review. *J. Clean. Prod.* **2019**, *228* (1), 801–813. https://doi.org/10.1016/j.jclepro.2019.04.304.

(89) Zhang, J.; Hu, J.; Zhang, W.; Chen, Y.; Wang, C. Efficient and Economical Recovery of Lithium, Cobalt, Nickel, Manganese from Cathode Scrap of Spent Lithium-Ion Batteries. *J. Clean. Prod.* **2018**, *204*, 437–446. https://doi.org/10.1016/j.jclepro.2018.09.033.

(90) Oar-Arteta, L.; Wezendonk, T.; Sun, X.; Kapteijn, F.; Gascon, J. Metal Organic Frameworks as Precursors for the Manufacture of Advanced Catalytic Materials. *Mater. Chem. Front.* **2017**, *1* (9), 1709–1745. https://doi.org/10.1039/c7qm00007c.

(91) Longo, E.; de Almeida La Porta, F. *Recent Advances in Complex Functional Materials: From Design to Application*; 2017. https://doi.org/10.1007/978-3-319-53898-3.

(92) Shen, Y. Carbothermal Synthesis of Metal-Functionalized Nanostructures for Energy and Environmental Applications. *J. Mater. Chem. A* **2015**, *3* (25), 13114–13188. https://doi.org/10.1039/c5ta01228g.

(93) Lai, C.; Chen, J.; Knight, J. C.; Manthiram, A.; Navrotsky, A. Thermodynamic Stability of Transition-Metal-Substituted LiMn2−xMxO4 (M=Cr, Fe, Co, and Ni) Spinels. *ChemPhysChem* **2016**, *4*, 1973–1978. https://doi.org/10.1002/cphc.201600120.

(94) Levene, P. A. CONFIGURATIONAL RELATIONSHIP OF HYDROCARBONS III.

THE OPTICAL ROTATIONS OF THE HYDROCARBONS OF THE SERIES METHYLISOBUTYLMETHANE. **1931**, *761*.

(95) Kim, M. geu; White, J. D. Olefins from Thermal Decomposition of N-Sulfoximino-2-Oxazolidones. A Novel Synthesis of Bicyclo[3.3.1]Non-l-Ene. *J. Am. Chem. Soc.* **1977**, *99* (4), 1172–1180. https://doi.org/10.1021/ja00446a032.

(96) Battino, R.; Seybold, P. G.; Campanell, F. C. Correlations Involving the Solubility of Gases in Water at 298.15 K and 101325 Pa. *J. Chem. Eng. Data* **2011**, *56* (4), 727–732. https://doi.org/10.1021/je101070h.

(97) Andersson, P.; Blomqvist, P.; Lorén, A. *Investigation of Fire Emissions from Li-Ion Batteries Investigation of Fire Emissions from Li-Ion Batteries*; SP Technical Research Institute of Sweden, 2013.

(98) Larsson, F.; Andersson, P.; Blomqvist, P.; Mellander, B. E. Toxic Fluoride Gas Emissions from Lithium-Ion Battery Fires. *Sci. Rep.* **2017**, *7* (1). https://doi.org/10.1038/s41598-017-09784-z.

(99) Terborg, L.; Weber, S.; Blaske, F.; Passerini, S.; Winter, M.; Karst, U.; Nowak, S. Investigation of Thermal Aging and Hydrolysis Mechanisms in Commercial Lithium Ion Battery Electrolyte. *J. Power Sources* **2013**, *242*, 832–837. https://doi.org/10.1016/j.jpowsour.2013.05.125.

(100) Grützke, M.; Krüger, S.; Kraft, V.; Vortmann, B.; Rothermel, S.; Winter, M.; Nowak, S. Investigation of the Storage Behavior of Shredded Lithium-Ion Batteries from Electric Vehicles for Recycling Purposes. *ChemSusChem* **2015**, *8* (20), 3433–3438. https://doi.org/10.1002/cssc.201500920.

(101) Nguyen, T. Degradation of Polyfvinyl Fluoride) and Poiyfvinylidene Fluoride). *J. Macromol. Sci. Part C* **1985**, *25* (2), 227–275. https://doi.org/10.1080/15583728509412823.

(102) Hirschler, M. M. Effect of Oxygen on the Thermal Decomposition of Poly(Vinylidene Fluoride). *Eur. Polym. J.* **1982**, *18* (5), 463–467. https://doi.org/10.1016/0014-3057(82)90184-7.

(103) Mears, W. H.; Stahl, R. F.; Orfeo, S. R.; Shair, R. C.; Kells, L. F.; Thompson, W.;

McCann, H. Thermodynamic Properties of Halogenated Ethanes and Ethylenes. *Ind. Eng. Chem.* **1955**, *47* (7), 1449–1454. https://doi.org/10.1021/ie50547a052.

(104) Feng, X.; Ouyang, M.; Liu, X.; Lu, L.; Xia, Y.; He, X. Thermal Runaway Mechanism of Lithium Ion Battery for Electric Vehicles: A Review. *Energy Storage Mater.* **2018**, *10* (December 2016), 246–267. https://doi.org/10.1016/j.ensm.2017.05.013.

(105) Shipilov, A. I.; Kostareva, E. V.; Kochanov, A. S. Selective Dechlorination of Polychlorofluoroaromatic Compounds: Preparation of 1,3,5-Trifluorobenzene. *J. Fluor. Chem.* **1999**, *96* (1), 23–24. https://doi.org/10.1016/S0022-1139(98)00329-7.

(106) IRVING, J. B.; JAMIESON, D. T. THERMAL CONDUCTIVITY OF 13 FLUOROCARBON LIQUIDSVan. *Journul Fluor. Chemishv* **1975**, No. 5, 449–456. https://doi.org/DOI: 10.1007/BF02389711.

(107) Aroney, M. J.; Cleaver, G.; Pierens, R. K.; Le Fèvre, R. J. W. Molecular Polarisability. The Anisotropy of the Car-F Group. *J. Chem. Soc. Perkin Trans. 2* **1974**, *1* (1), 3–5. https://doi.org/10.1039/P29740000003.

(108) Shin, T.; Hajima, O.; Chuichi, W. *Pyrograms and Thermograms of 163 High Polymers, and MS Data of the Major Pyrolyzates*; 2011. https://doi.org/10.1016/b978-0-444-53892-5.10002-1.

(109) Weber, R.; Schrenk, D.; Hagenmaier, A.; Hagenmaier, H. POLYFLUORINATED DIBENZODIOXINS AND DIBENZOFURANS - SYNTHESIS, ANALYSIS, FORMATION AND TOXICOLOGY. **1995**, *30* (4), 629–639.

(110) Weber, R.; Schmitz, H. J.; Schrenk, D.; Hagenmaier, H. Metabolic Degradation, Inducing Potency, and Metabolites of Fluorinated and Chlorinated-Fluorinated Dibenzodioxins and Dibenzofurans. *Chemosphere* **1997**, *34* (1), 29–40. https://doi.org/10.1016/S0045-6535(96)00365-7.

(111) Zhang, C.; Sun, X. Gas-Phase Tropospheric Chemistry of 2,3,7,8-Tetrafuorinated Dibenzo-p-Dioxin. *Sci. Total Environ.* **2014**, *468–469*, 104–110. https://doi.org/10.1016/j.scitotenv.2013.08.018.

(112) Zhang, S. S.; Xu, K.; Jow, T. R. A Thermal Stabilizer for LiPF6-Based Electrolytes of Li-Ion Cells. *Electrochem. Solid-State Lett.* **2002**, *5* (9), 1–4.

https://doi.org/10.1149/1.1499669.

(113) Yang, H.; Zhuang, G. V.; Ross, P. N. Thermal Stability of LiPF6 Salt and Li-Ion Battery Electrolytes Containing LiPF6. *J. Power Sources* **2006**, *161* (1), 573–579. https://doi.org/10.1016/j.jpowsour.2006.03.058.

(114) [JCP 13] JCPDS – International Center for Diffraction Data, PDF – 4+, (2013), 12 Campus Blvd., Newton Square, PA 19073 – 3273 U.S.A. https://doi.org/10.11113/jt.v56.60.

(115) Kuila, A.; Maity, N.; Chatterjee, D. P.; Nandi, A. K. Temperature Triggered Antifouling Properties of Poly(Vinylidene Fluoride) Graft Copolymers with Tunable Hydrophilicity. *J. Mater. Chem. A* **2015**, *3* (25), 13546–13555. https://doi.org/10.1039/c5ta01306b.

(116) Xiao, J.; Li, J.; Xu, Z. Novel Approach for in Situ Recovery of Lithium Carbonate from Spent Lithium Ion Batteries Using Vacuum Metallurgy. *Environ. Sci. Technol.* **2017**, *51* (20), 11960–11966. https://doi.org/10.1021/acs.est.7b02561.

(117) Choi, S. S.; Kim, Y. K. Microstructural Analysis of Poly(Vinylidene Fluoride) Using Benzene Derivative Pyrolysis Products. *J. Anal. Appl. Pyrolysis* **2012**, *96*, 16–23. https://doi.org/10.1016/j.jaap.2012.02.014.